AN ABSTRACT OF THE THESIS OF

William R. Tahnk for the degree of Doctor of Philosophy in Atmospheric Sciences presented on February 2, 2001.

Title: INDOEX Aerosol Optical Depths and Radiative Forcing Derived From AVHRR

Redacted for privacy

Abstract approved: _____

James A. Coakley, Jr.

The Indian Ocean Experiment (INDOEX) had as a primary objective determining the radiative forcing due to anthropogenic aerosols over climatologically significant space and time scales: the Indian Ocean during the winter monsoon, January – March. During the winter monsoon, polluted, low-level air from the Asian subcontinent blows over the Arabian Sea and Indian Ocean. As part of INDOEX, aerosol optical depths were derived from Advanced Very High Resolution Radiometer (AVHRR) data for the cloud-free ocean regions. The AVHRR radiances were first calibrated using the interior zone of the Antarctic and Greenland ice sheets, which proved to be radiometrically stable calibration targets. Optical depths were derived by matching the observed radiances to radiances calculated for a wide range of optical depths and viewing geometry. Optical depths derived with the AVHRR were compared with those derived with NASA's Aerosol Robotic Network (AERONET) CIMEL instrument at the Center for Clouds, Chemistry, and Climate's Kaashidhoo Observatory, as well as with other surface and shipboard observations taken in the INDOEX region. The

retrieved and surface-based optical depths agreed best for a new 2-channel, 2-aerosol model scheme in which the AVHRR observations at 0·64 and 0·84 microns were used to determine relative amounts of marine and polluted continental aerosol and then the resulting aerosol mixture was used to derive the optical depths. Broadband radiative transfer calculations for the mixture of marine and polluted continental aerosols were combined with the 0·64 and 0·84-micron AVHRR radiances to determine the radiative forcing due to aerosols in the INDOEX region. Monthly composites of aerosol optical depth and top of the atmosphere, surface, and atmospheric radiative forcing were derived from calibrated AVHRR radiances for January-March 1996-2000. An inter-annual variability in the magnitude and spatial extent of high value regions is noted for derived optical depths and radiative forcing, with highest values reached in 1999, particularly in the Bay of Bengal which during the IFP was covered by plumes from Indochina. Frequency distributions of the optical depth for $1° \times 1°$ latitude-longitude regions are well represented by gamma distribution functions. The day-to-day and year-to-year variability of the optical depth for such regions is correlated with the long term average optical depth. Interannual variability of the monthly mean optical depths for such regions is found to be as large as the day to day.

INDOEX Aerosol Optical Depths and Radiative Forcing Derived From AVHRR

by

William R. Tahnk

A Thesis Submitted

to

Oregon State University

In Partial Fulfillment of

the requirements for the

degree of

Doctor of Philosophy

Presented February 2, 2001

Commencement June 2001

Doctor of Philosophy thesis of William R. Tahnk presented on February 2, 2001

APPROVED:

Redacted for privacy

Major Professor, representing Atmospheric Sciences

Redacted for privacy

Dean of College of Oceanic and Atmospheric Sciences

Redacted for privacy

Dean of Graduate School

I understand that my thesis will become part of the permanent collection of Oregon State University libraries. My signature below authorizes release of my thesis to any reader upon request.

Redacted for privacy

William R. Tahnk, Author

ACKNOWLEDGEMENTS

I'd like to express my gratitude to Professor James A. Coakley, Jr., for his countless hours of counsel, discussion, and encouragement. His enthusiasm and thirst for knowledge are infectious and always an inspiration. The INDOEX project afforded me the unique opportunity to participate in a top-notch field experiment and work closely with scientists from all over the world. I would also like to thank Professor Coakley and John Wong for creating and maintaining a first-class research environment.

I wish to thank Drs. Jeffrey Barnes, Steven Esbensen, Larry Mahrt, and Barbara Gartner for examining the dissertation and serving on my doctoral committee.

Finally, I am very grateful for the steady funding which supported my research. This work was supported by a National Science Foundation Science and Technology Center grant to the Scripps Institute of Oceanography Center for Clouds, Chemistry and Climate (C^4).

TABLE OF CONTENTS

TABLE OF CONTENTS (Continued)

Page

TABLE OF CONTENTS (Continued)

Page

LIST OF FIGURES

LIST OF FIGURES (Continued)

LIST OF FIGURES (Continued)

LIST OF FIGURES (Continued)

LIST OF FIGURES (Continued)

LIST OF FIGURES (Continued)

LIST OF TABLES

INDOEX Aerosol Optical Depths and Radiative Forcing Derived From AVHRR

Chapter 1
Introduction

1.1 Background

The burning of fossil fuels, changes in land cover and use, and other human activities are having a profound effect on the climate and energy balance of Earth. Atmospheric concentrations of greenhouse gases are increasing, which alters the planet's radiative balance and tends to warm the atmosphere. On the other hand, human activities are also responsible for an increase in aerosol concentrations in some regions, which is thought to have an opposite effect on the radiative balance and an overall cooling effect on the atmosphere. These changes in the levels of greenhouse gases and aerosols are expected to result in regional and global changes in temperature, precipitation, and circulation, and other more subtle global climate changes. The magnitude of these changes and the degree to which they offset each other is unclear. Uncertainty in the magnitude of climate forcing by aerosols results from a lack of knowledge of global aerosol characteristics and temporal changes. Careful and accurate estimates of aerosol properties on regional and global scales are therefore a necessary complement to any study of climate forcing.

Aerosols are small particles and droplets of natural and human origin that are suspended in the atmosphere for a length of time. They include dust and other particles that can be composed of a variety of different chemicals and constituents. Aerosols of human origin are primarily the result of fossil fuel and biomass burning, while natural aerosols are chiefly the result of volcanic activity, biological processes, fires, and dust storms.

Aerosols in the atmosphere influence the radiation balance and climate of Earth both directly and indirectly. The direct effect of aerosols on climate is through scattering and absorption of sunlight (Charlson et. al., 1992). The degree to which aerosols attenuate sunlight is usually expressed as an optical depth or thickness, a unitless number that is proportional to the likelihood that light will be scattered or absorbed. Aerosols also increase cloud albedo through microphysical processes (Twomey 1977, Twomey et. al., 1984), and possibly suppress precipitation and increase cloud lifetime (Albrecht, 1989), resulting in climate forcing as an indirect effect. The amount of aerosol introduced into the atmosphere each year through industrial processes can be estimated with some degree of accuracy (Spiro et. al., 1992), though the short and long term quantitative effects of these aerosols on the global climate and energy budget is largely unknown (Intergovernmental Panel on Climate Control (IPCC), 1994), mostly due to our lack of knowledge regarding the optical and physical properties of aerosols.

In general, any factor altering the amount of solar radiation received at the surface can affect climate. The effect induced by these factors, which causes a change in the amount of energy available to the Earth-atmosphere system, is termed radiative forcing. The radiative forcing due to aerosols depends on their spatial distribution and optical and physical properties. Optical properties define the degree to which aerosols can absorb and scatter radiation, while physical properties relate to the size, shape, and chemical composition of the particles. Comparatively speaking, these properties are better understood for stratospheric aerosols than for tropospheric aerosols (IPCC 1996, Sato et. al. 1993, Kaufman et. al. 1997). Most anthropogenic aerosols are found in the lower troposphere, at altitudes below 2 km and with residence times of a few days. Consequently, the tropospheric aerosols are distributed inhomogeneously over a region with high concentrations near the source. Any offset to warming by greenhouse gases that aerosols provide will therefore be spatially and temporally inhomogeneous and thus difficult to quantify on a global scale.

Estimates of the radiative forcing due to changes in greenhouse gas concentrations since pre-industrial times are provided by the IPCC (1994) and are thought to be relatively certain. This certainty is due to the spatial and temporal uniformity of the greenhouse gas distribution, and to their known optical properties. The IPCC estimates radiative forcing due to greenhouse gases (CO_2, CH_4, N_2O, and the halocarbons) to be +2·45 Wm^{-2} ±0·4 Wm^{-2}, based on 1994 levels (IPCC, 1994). In contrast, the estimates of direct forcing by sulfates and organics from biomass burning, and indirect effects of tropospheric aerosols in general have such a high degree of uncertainty that their usefulness in predicting climate change on decadel and longer time scales is severely limited. The IPCC estimates the total direct forcing due to anthropogenic aerosols (sulfates, fossil fuel soot, and organics from biomass burning) to be –0·5 Wm^{-2} ±0·3 Wm^{-2}, based on 1996 levels (IPCC, 1996). Due to the high level of uncertainty, estimates of radiative forcing resulting from changes in cloud properties influenced by aerosols (the indirect effect) range from 0 to -1·5 Wm^{-2}.

1.2 Motivation

To better understand the impact of aerosols on climate and the energy budget, and reduce the uncertainty in the estimates of climate forcing, the optical and physical properties of aerosols and their spatial distribution must be known (Kaufman et. al., 1997). Frequent global remote sensing measurements of the variation of aerosol spatial distribution and some key optical properties, combined with periodic *in situ* measurements for verification, are essential to a more accurate understanding of the climate forcing by aerosols.

To improve our understanding of aerosol climate forcing, the Indian Ocean Experiment (INDOEX) was designed as a focused field experiment to study and

attempt to quantify the role of aerosols, clouds, and tropospheric chemistry and transport, in climate forcing and change (Ramanathan et. al., 1996). The primary objectives were threefold: (1) to assess the significance of sulfates and other continental aerosols on global radiative forcing; (2) to assess the magnitude of the solar absorption at the surface and in the troposphere including the role of Inter-Tropical Convergence Zone (ITCZ) cloud systems; and (3) to assess the role of the ITCZ in the transport of trace species and pollutants and their resultant radiative forcing.

The major field campaigns of INDOEX took place during the late winter and early spring of 1998 and 1999. During the months of the northeast monsoon, the Arabian Sea and equatorial Indian Ocean are a unique natural laboratory. From January through March the predominant low-level wind is a northeasterly flow carrying mineral dust and anthropogenic aerosols from the Indian subcontinents and surrounding nations to the Arabian Sea and Bay of Bengal. These aerosols stagnate and concentrate off the West Coast of India and in the Bay of Bengal, which remain largely cloud-free, thereby creating a gigantic laboratory to observe the effects of aerosols on solar radiation. Surface, aircraft, and ship measurements of aerosol and solar radiation parameters were made during the First Field Phase (FFP), conducted in February and March, 1998, and during the Intensive Field Phase (IFP), conducted during February and March, 1999. These *in situ* measurements can be compared with aerosol optical parameters derived from calibrated satellite observations to derive monthly and seasonal composites of aerosol optical parameters over the INDOEX region.

This dissertation seeks to use satellite observations to describe the spatial and temporal distribution and variability of aerosol optical parameters and estimate the direct effect of aerosols on radiative forcing and climate in the INDOEX region. Observations from the Advanced Very High Resolution Radiometer (AVHRR), a multi-spectral scanning radiometer onboard the NOAA-14 spacecraft, were used to derive aerosol optical parameters. Calibrated radiances from the AVHRR visible

and infrared channels were used for cloud screening and to derive aerosol optical depth and radiative forcing for cloud-free pixels in the satellite's field of view.

The treatment of clouds in climate models is thought to be a great source of uncertainty in accurately predicting long term climate change. Clouds affect climate in two ways, depending on the cloud altitude. Low clouds mainly reflect incoming solar radiation, thus removing energy from the Earth-atmosphere system. High clouds (cirrus) trap and reduce outgoing radiation more than they reflect incoming solar radiation, thereby adding energy to the system. This dual nature of cloud's influence on climate complicates the determination of aerosol direct radiative forcing in the INDOEX region, since the frequency of occurrence of partly cloud covered and overcast pixels was significant. Several alternative treatments of aerosol forcing under "average cloud conditions" are examined.

During the INDOEX campaign, the NOAA-14 spacecraft was ideally positioned for retrieval of daytime aerosol optical conditions. Optical depth measurements made at the Kaashidhoo Climate Observatory, on the island of Hulule, and aboard ship compare favorably with aerosol optical depths derived from co-located satellite observations. Calibrated NOAA-14 radiances, were used to derive composites of mean monthly aerosol optical depth and top of the atmosphere, surface, and atmospheric aerosol direct radiative forcing for the period January-March 1996-2000. For all years, the seasonally-averaged aerosol direct radiative forcing of the atmosphere for the INDOEX region (30S to 30N, 50E to 110E) is -2.4 Wm^{-2} ±0·5 Wm^{-2} for average cloud conditions, which is somewhat higher than the IPCC global annual estimate of -0·5 Wm^{-2} ±0·5 Wm^{-2} for direct forcing by anthropogenic aerosols. The difference in magnitude would likely be mitigated once the AVHRR-derived forcing estimates were extended to long-term global annual averages.

An inter-annual variability in the magnitude and spatial extent of high value regions is noted for derived optical depths and radiative forcing, with highest values reached in 1999, particularly in the Bay of Bengal which during the IFP was covered by plumes from Indochina. Frequency distributions of the optical depth

for $1° \times 1°$ latitude-longitude regions are well represented by gamma distribution functions. The day-to-day and year-to-year variability of the optical depth for such regions is correlated with the long term average optical depth. Interannual variability of the monthly mean optical depths for such regions is found to be as large as the day to day.

1.3 Outline of the Dissertation

To obtain reasonable estimates of aerosol optical depth and radiative forcing, we must first ensure that the satellite observations are accurately calibrated. An analysis of the calibration coefficients used to describe sensor degradation in channels 1 and 2 of AVHRR on NOAA-14 is presented in Chapter 2. Section 2.1 is the introduction. Section 2.2 discusses the use of the interior zones of the permanent ice sheets of Antarctica and Greenland as radiometrically stable targets for calibrating NOAA-14 visible and near-infrared channels. Section 2.3 presents the results of the calibration study. New calibration equations are derived using observations through January 1998 and compared with published coefficients. Section 2.4 extends the calibration study to present using Antarctic and Greenland data for the period 1999-2000.

Accurate retrievals of aerosol optical parameters depend critically on the selection of an appropriate size distribution and index of refraction. A review of the physical and optical characteristics of aerosols and their size distributions is presented in Chapter 3. Section 3.1 is the introduction. In section 3.2, a review of Mie theory is presented. Section 3.3 is a review of standard size distributions commonly used to describe aerosols. An inter-comparison of standard size distributions is presented in Section 3.4. This includes a comparison of the phase function for a typical distribution of aerosols, and specific distributions of haze

particles and cloud droplets. Section 3.5 presents the results of studies examining the sensitivity of the scattering phase function to a variety of aerosol mixtures and models.

A new scheme for retrieving aerosol properties for ocean regions from reflected sunlight at both the visible and near infrared wavelengths measured by the NOAA-14 AVHRR is presented in Chapter 4. A review of existing techniques for deriving aerosol optical parameters from satellite radiances and the aerosol models used, is presented in Section 4.1. In section 4.2, methods used to identify cloud-free fields of view are described. In addition, the aerosol models used to calculate cloud-free reflectances and the procedures used to extract aerosol optical properties using existing schemes and a new 2-channel, 2-model scheme are presented. Procedures for using the derived optical depth and mixing fraction from the 2-channel, 2-model scheme to estimate net radiative flux and aerosol direct radiative forcing are described in Section 4.3. The results of a comparison of retrieved optical depths from a number of extraction schemes, with surface measurements from a number of sources, are presented in section 4.4. Section 4.5 presents an evaluation of aerosol direct radiative forcing for cloud-free and average cloud conditions at the top of the atmosphere, the surface and in the atmosphere using the 2-channel, 2-model scheme and several single-channel, single model schemes.

A 5-year climatology of aerosol optical depth and radiative forcing for the INDOEX region is presented in Chapter 5. Section 5.1 is the introduction. The analysis technique is presented in section 5.2. Sources of error in deriving spatial and temporal means for gridded data are examined. The treatment of clouds in computing aerosol direct radiative forcing under average cloud conditions is discussed. Analysis results for aerosol optical depth and derived mixing fraction are presented in section 5.3. A detailed analysis of day-to-day and year-to-year variability in optical depth is given in section 5.4. Seasonal climatology for aerosol direct radiative forcing for top of the atmosphere, surface, and the

atmosphere, for cloud-free and average conditions, is presented and discussed in section 5.5.

A summary and concluding remarks are presented in Chapter 6.

Chapter 2
Improved Calibration Coefficients for NOAA-14 AVHRR Visible and Near-IR Channels

2.1 Introduction

NOAA Advanced Very High Resolution Radiometer (AVHRR) observations have received considerable use in deriving cloud cover, cloud top altitudes, visible optical depths, effective droplet radii (Han et al. 1994, 1998), aerosol burdens over oceans (Husar et al. 1997), vegetation indices (Gutman et al. 1995), in addition to their intended use, sea surface temperatures (McClain et al. 1985, May et al. 1998). All of these derived products require calibrated radiances. While the AVHRR carries a blackbody for the calibration of the thermal channels: channel 3 at 3.7 μm, 4 at 11 μm, and 5 at 12 μm, there is no calibration source for the visible channel: channel 1 at 0.64 μm and the near-IR channel: channel 2 at 0.85 μm, and the sensitivities of these channels are known to degrade with time (Brest and Rossow 1992, Kaufman and Holben 1993, Rao and Chen 1995). Consequently, studies have been conducted in recent years to derive improved post-launch calibration coefficients which characterize AVHRR sensor degradation. In preparation for the extraction of aerosol properties from AVHRR radiances for the Indian Ocean Experiment (INDOEX), NOAA-14 observations of the Greenland and Antarctic ice sheets are used to assess the calibration coefficients recommended for the AVHRR.

Kaufman and Holben (1993) and Rao and Chen (1996) used large, homogeneous, fixed desert targets as calibration sources to characterize AVHRR sensor degradation. Loeb (1997), on the other hand, used the permanent ice sheets of Greenland and Antarctica as calibration targets. As with deserts, the interior zones of permanent ice sheets are spatially and temporally stable (Kukla and

Robinson 1980, Weller 1980). At high latitudes there are numerous overpasses within a given month that provide acceptable viewing geometries for the determination of calibration coefficients. A disadvantage, of course, is that high latitude snow and ice scenes can be viewed only during the summer season.

In this study, daily NOAA-14 passes are used to examine calibration targets over the Antarctic and Greenland ice sheets. Calibration coefficients are derived for the Antarctic ice sheet and the stability of the coefficients is examined using the Greenland ice sheet. Raw pixel counts measured in homogeneous regions of the permanent ice sheets are used to derive reflectances for the visible and near-IR channels of the AVHRR based on the standard reflectances derived by Loeb (1997) using NOAA-9 AVHRR data. NOAA-9 AVHRR data serves as the standard for calibration (Rao and Chen, 1995). The NOAA-14 reflectances are compared with reflectances obtained using the calibration algorithms recommended by Rao and Chen (1996 and private communication) and included in the NOAA-14 Level 1b data stream by NOAA. In the case of the Greenland ice sheet, new reflectance standards are derived for channel 2 using the NOAA-14 observations at viewing geometries not investigated by Loeb. The analysis and results presented in sections 2.2 and 2.3 are based on NOAA-14 data through 1998. Further modifications to derived calibration coefficients based on a reanalysis of NOAA-14 data after June 1998 are presented in section 2.4.

2.2 Analysis

NOAA-14 AVHRR Global Area Coverage (GAC) measurements (Kidwell, 1994) are collected on a daily basis for the periods January 1996, 1997, and 1998 for Antarctica and for May and June 1995, 1996, 1997, and 1998 for Greenland. For Antarctica, the observations are collected for 60S to 90S and 70E to 160E. For

Greenland, the observations are collected for 73N to 78N and 32W to 48W. Each data point is represented by a 10-bit raw pixel count for a particular AVHRR channel. The reflectance is given by

$$R_i = \frac{(\alpha_i C_{10}^i + \beta_i)\delta_{ES}}{\mu_0} \tag{2.1}$$

where (for channel i):

R_i = reflectance (or equivalently, the isotropic albedo, in %);

α_i = slope (%albedo/count);

β_i = intercept (%albedo);

C_{10}^i = 10-bit raw pixel count;

δ_{ES} = correction for mean Earth-Sun distance;

μ_0 = cosine of the solar zenith angle.

To insure that the satellite measurements included in the radiometric study are spatially and temporally homogeneous and stable, certain criteria are applied in the analysis. First, the GAC AVHRR 4-km data are divided into 17 scan line by 17 scan spot arrays covering approximately (68 km)^2 subregions at nadir. To minimize effects due to the anisotropy of the surface reflection, only subregions near nadir (average view zenith angle less than 18 degrees) are considered. To minimize uncertainties due to variations in surface type (land versus water, coastal ice versus snow and ice cover over land), only pixels that are well inland are included. The solar zenith angle for NOAA-14 satellite passes over the Antarctic region in Southern Hemisphere summer is restricted to the range 55 to 75 degrees. Table 2.1 summarizes the NOAA-14 data considered in the analysis, after these constraints are applied. Observations of the Antarctic ice sheet are used to derive calibration coefficients, and observations of the Greenland ice sheet are used to

verify the mid-year values of the coefficients. Since the satellite launch date was December 30, 1994, January 1995 observations were examined for inclusion, but observations for the thermal channels at 3.7 and 11 μm, which are used to test the spatial uniformity of the targets, as described below, were missing from the data stream for January 1995.

Table 2.1. The count of NOAA-14 AVHRR images and sub-regions considered in this study.

Month/Year	Region	No. of passes used	No. of sub-regions used
January 1996	Antarctica	31	2393
January 1997	Antarctica	31	2388
January 1998	Antarctica	31	2364
May 1995	Greenland	31	778
May 1996	Greenland	31	789
May 1997	Greenland	31	893
May 1998	Greenland	31	754
June 1995	Greenland	60	1720
June 1996	Greenland	60	1476
June 1997	Greenland	60	1500
June 1998	Greenland	60	1605

Calibration curves constructed from NOAA-9 AVHRR channel 1 and 2 reflectances are used as a reference for uncalibrated AVHRR observations. For NOAA-9, Loeb (1997) determined that the reflectances in channel 1 and 2 are given by

$$R_1 = 74.25 + 0.8953\theta_o - 0.01233\theta_o^2 \quad (2.2a)$$

$$R_2 = 60.29 + 0.8305\theta_o - 0.00915\theta_o^2 \quad (2.2b)$$

for Antarctica, and by

$$R_1 = 81.37 + 0.5202\theta_o - 0.009152\theta_o^2 \quad (2.3a)$$

$$R_2 = 103.9 - 0.6072\theta_o + 0.001373\theta_o^2 \quad (2.3b)$$

for Greenland, where:

R_1, R_2 = channel reflectance (in %);

θ_o = solar zenith angle (in degrees).

(2.2a) and (2.2b) are restricted to solar zenith angles between 63° and 80°, and (2.3a) and (2.3b) are for solar zenith angles between 46° and 73°. As will be shown later, the viewing geometry dependent reflectances differ from those given by (2.3b) for channel 2 at solar zenith angles not investigated by Loeb.

Because of their remote locations, the ice sheets are assumed to be immune to radiance variations due to airborne pollutants. They are, however, subject to radiance variations due to clouds. In order to minimize effects due to clouds, an index of homogeneity is calculated for each (68 km)^2 subregion following Loeb (1997):

$$N = \frac{1}{4}\left(\frac{\sigma_1}{\overline{R_1}} + \frac{\sigma_2}{\overline{R_2}} + \frac{\sigma_3}{\overline{T_3}} + \frac{\sigma_4}{\overline{T_4}}\right) \times 100\% \quad (2.4)$$

where (for channel number given by the subscript):

N = index of homogeneity (in %);

$\overline{R_1}, \overline{R_2}$ = mean channel reflectances;

σ_1, σ_2 = standard deviation of channel reflectances;

$\overline{T_3}, \overline{T_4}$ = mean channel brightness temperatures;

σ_3, σ_4 = standard deviation of channel brightness temperatures.

A large N implies large spatial variations in pixel reflectances and/or brightness temperatures within the subregion, probably due to the presence of clouds. Conversely, a small N implies small spatial variations in pixel reflectances and brightness temperatures. Such regions are assumed to be cloud-free.

2.3 Results

Figures 2.1 and 2.2 show reflectances and N, the index of homogeneity, for NOAA-14 AVHRR channels 1 and 2, and for the data periods given in Table 2.1 for Antarctica. For consistency between years, only subregions with solar zenith angles between 63 and 68 degrees are shown. The reflectances for the Antarctic region for all years are calibrated using the following formulae, which were adopted by Rao and Chen in 1995 as a revision to the pre-launch coefficients:

$$R_1 = 0.1115C_{10}^1 - 4.5715 \quad (2.5a)$$

$$R_2 = 0.1337C_{10}^2 - 5.4827 \quad (2.5b)$$

where:

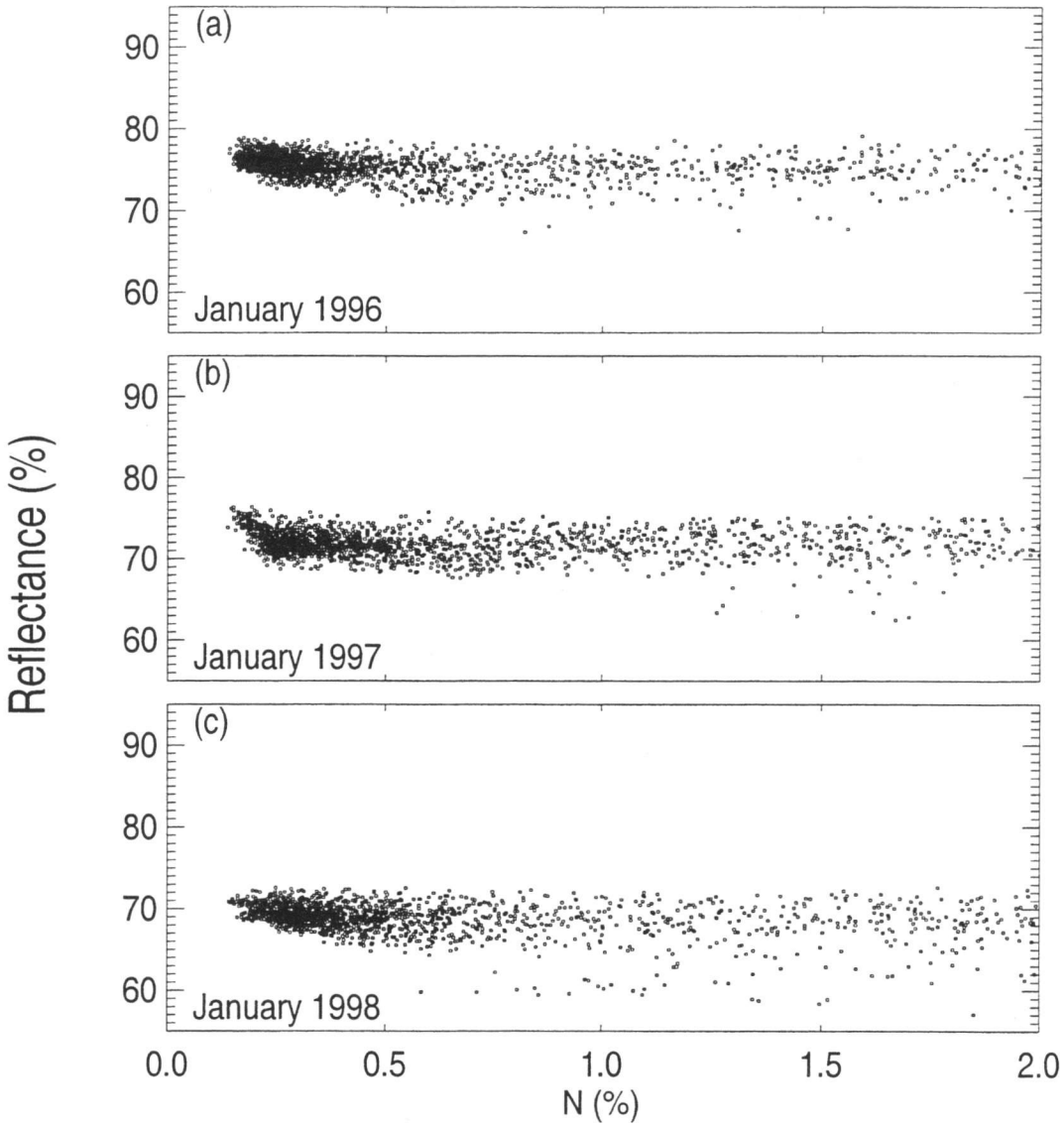

Figure 2.1. NOAA-14 AVHRR Channel 1 reflectances and N, the index of homogeneity, for 17 × 17 pixel subregions having view zenith angles less than 18° and solar zenith angles between 63° and 68° in (a) January 1996, (b) January 1997, and (c) January 1998 for Antarctica. The reflectances are obtained using (2.5a).

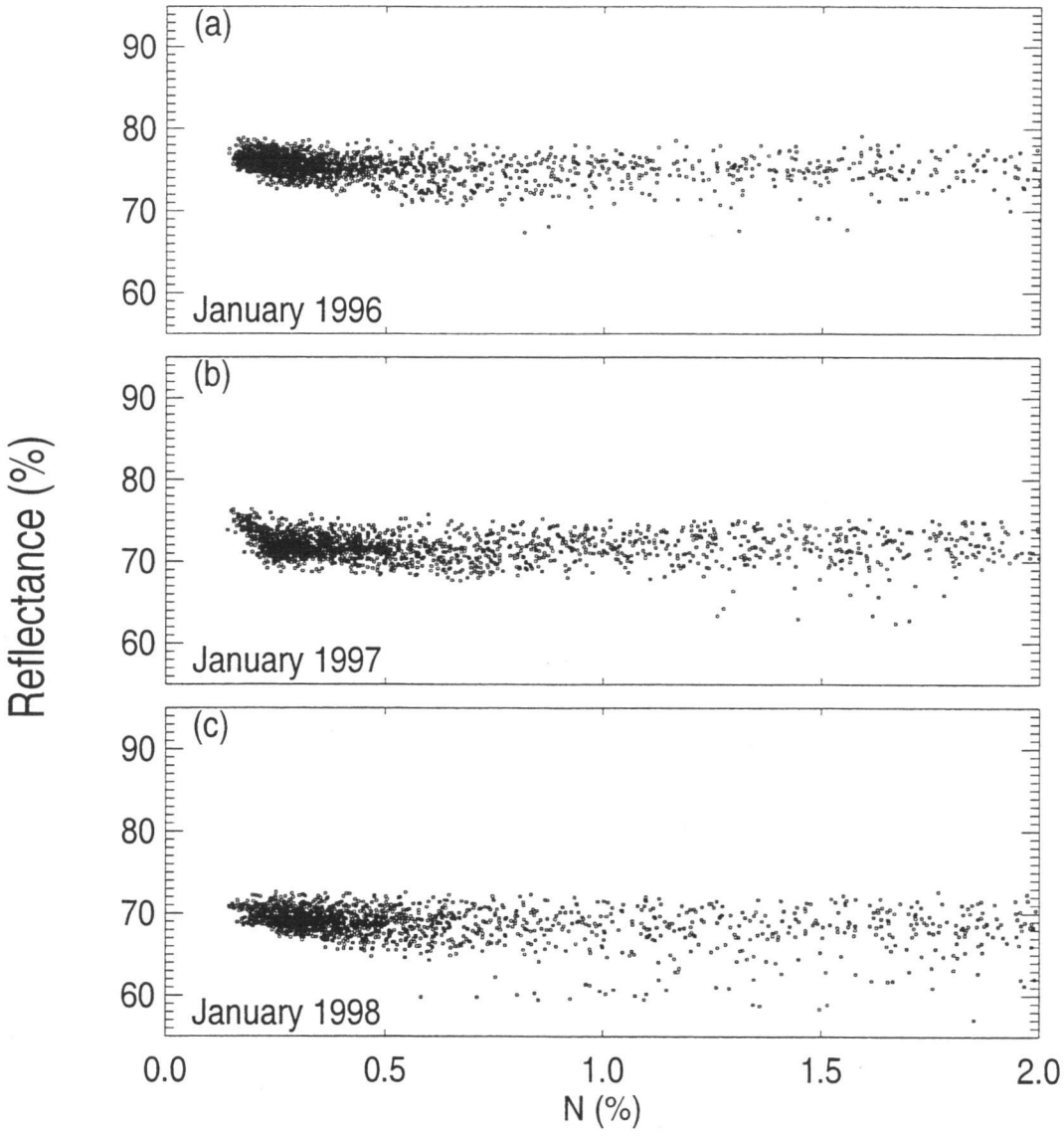

Figure 2.2. NOAA-14 AVHRR Channel 2 reflectances and N, the index of homogeneity, for 17 × 17 pixel subregions having view zenith angles less than 18° and solar zenith angles between 63° and 68° in (a) January 1996, (b) January 1997, and (c) January 1998 for Antarctica. The reflectances are obtained using (2.5b).

R_1, R_2 = channel reflectance (in %);

C_{10}^1, C_{10}^2 = channel 10-bit raw pixel count.

For all years and both channels, when N is small (less than about 0·6%), the reflectances are stable and clustered. As N becomes large, reflectances are widely scattered, implying a lack of homogeneity, suggesting cloud contamination. Loeb (1997) presents several plausible explanations for why the pattern of widely scattered points at high values of N appear to be associated with the presence of clouds in the subregion. For nadir views and high solar zenith angles, the forward scattering of sunlight by clouds prevents the light from reaching the surface, which reduces the scene reflectance.

Figures 2.3 and 2.4 show reflectances for channels 1 and 2 as a function of solar zenith angle for only those subregions that displayed a high degree of homogeneity ($N < 0{\cdot}6\%$ for channel 1 and $N < 0{\cdot}4\%$ for channel 2). Superimposed on the observations are the NOAA-9 reference calibration curves (2.2a and 2.2b). Sensor degradation is clearly evident in channel 1, with only a small change over time in channel 2.

Rao and Chen (1996) derived calibration equations using the desert reference and 1995 data. Based on their determination, reflectance in channels 1 and 2, as a function of day since launch and pixel count, is expressed as the product of the 'slope' term and the pixel count as follows:

$$R_1 = (0.0000232d + 0.109) \times (C_{10}^1 - C_0) \qquad (2.6a)$$

$$R_2 = (0.0000373d + 0.129) \times (C_{10}^2 - C_0) \qquad (2.6b)$$

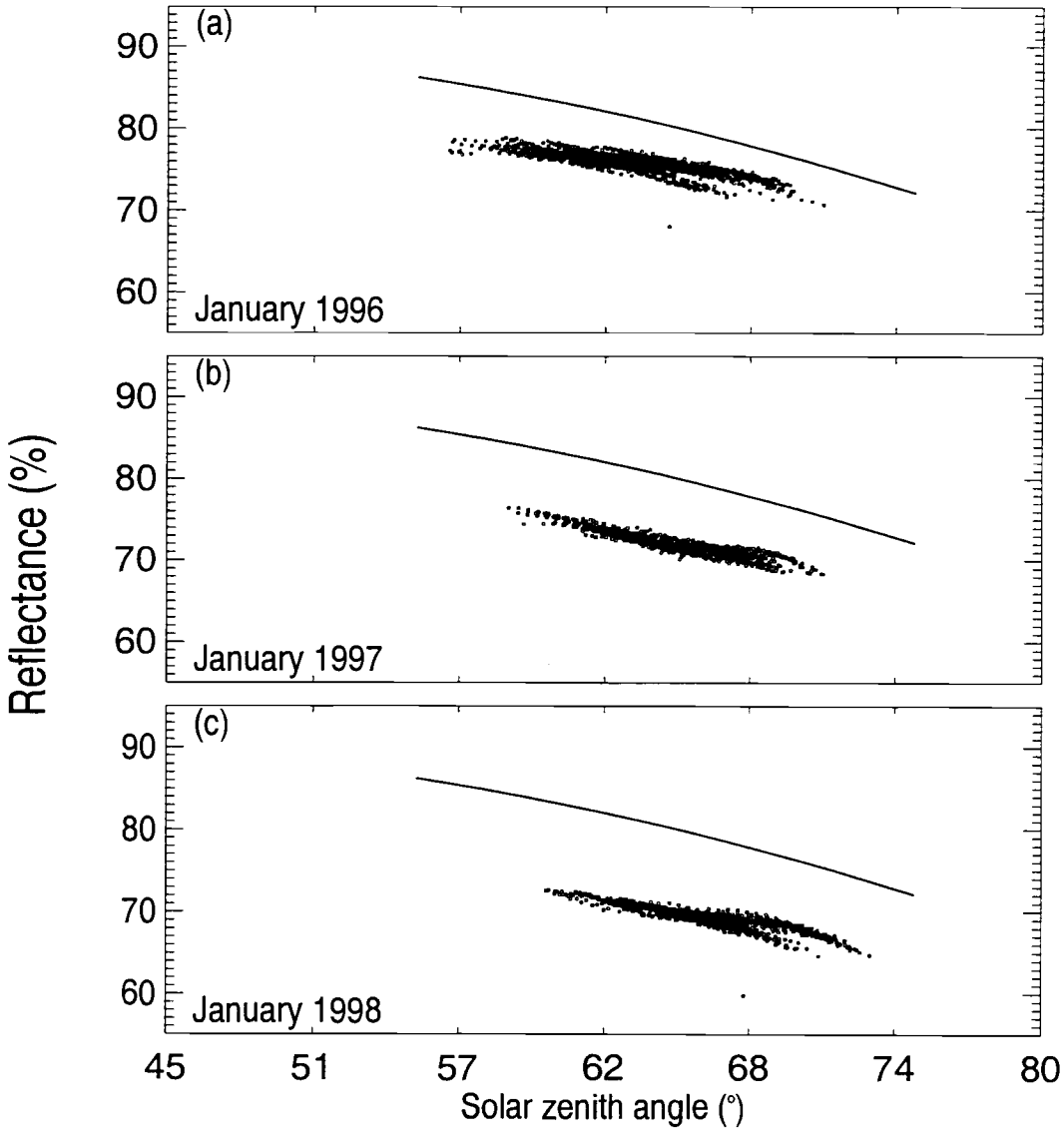

Figure 2.3. NOAA-14 AVHRR Channel 1 reflectances and solar zenith angles for 17×17 pixel subregions with $N < 0{\cdot}6\%$ in (a) January 1996, (b) January 1997, and (c) January 1998 for Antarctica. The solid line represents the NOAA-9 calibration reference for Antarctica, from Loeb (1997). The NOAA-14 reflectances are obtained using (2.5a).

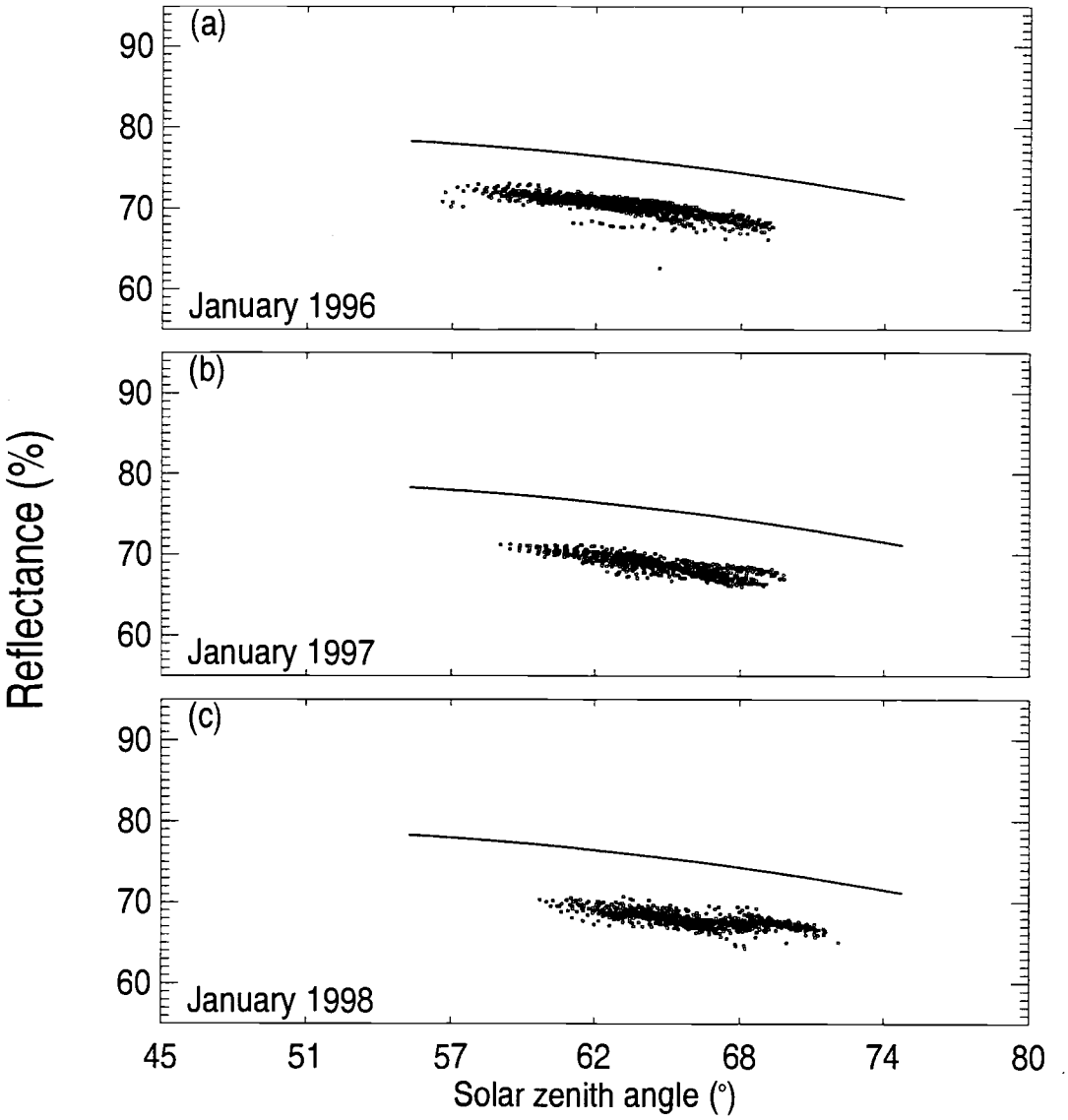

Figure 2.4. NOAA-14 AVHRR Channel 2 reflectances and solar zenith angles for 17×17 pixel subregions with $N < 0{\cdot}4\%$ in (a) January 1996, (b) January 1997, and (c) January 1998 for Antarctica. The solid line represents the NOAA-9 calibration reference for Antarctica, from Loeb (1997). The NOAA-14 reflectances are obtained using (2.5b).

where:

R_1, R_2 = channel reflectance (in %);

d = day since launch (December 30, 1994: d = 0);

C_{10}^1, C_{10}^2 = channel AVHRR 10-bit raw pixel count;

C_0 = deep space offset = 41 for channels 1 and 2.

The standard errors of estimates of reflectance for (2.6a) and (2.6b) given by Rao and Chen (1996) are 1.5 and 2.1 in units of % reflectance. Rao and Chen suggest that (2.6a) and (2.6b) be used to calibrate raw pixel counts for channels 1 and 2 for all times. Figures 2.5 and 2.6 are identical to Figs. 2.3 and 2.4, except that the reflectances are obtained using (2.6a) and (2.6b). Calibration coefficients based on (2.6a) and (2.6b) were imbedded in the NOAA Level 1b data stream for the period November 1996 – November 1998.

Rao and Chen (private communication) derived new calibration equations using the desert reference and 1996-1998 data. Based on the three-year record of observations over the desert site, the revised post-launch calibration equations are given as follows:

$$R_1 = (0.0000135d + 0.111) \times (C_{10}^1 - C_0) \qquad (2.7a)$$

$$R_2 = (0.0000133d + 0.134) \times (C_{10}^2 - C_0) \qquad (2.7b)$$

Figures 2.7 and 2.8 are identical to Figs. 2.5 and 2.6, except that the reflectances are obtained using (2.7a) and (2.7b). Commencing December 1998, calibration coefficients based on (2.7a) and (2.7b) are imbedded in the NOAA Level 1b data stream.

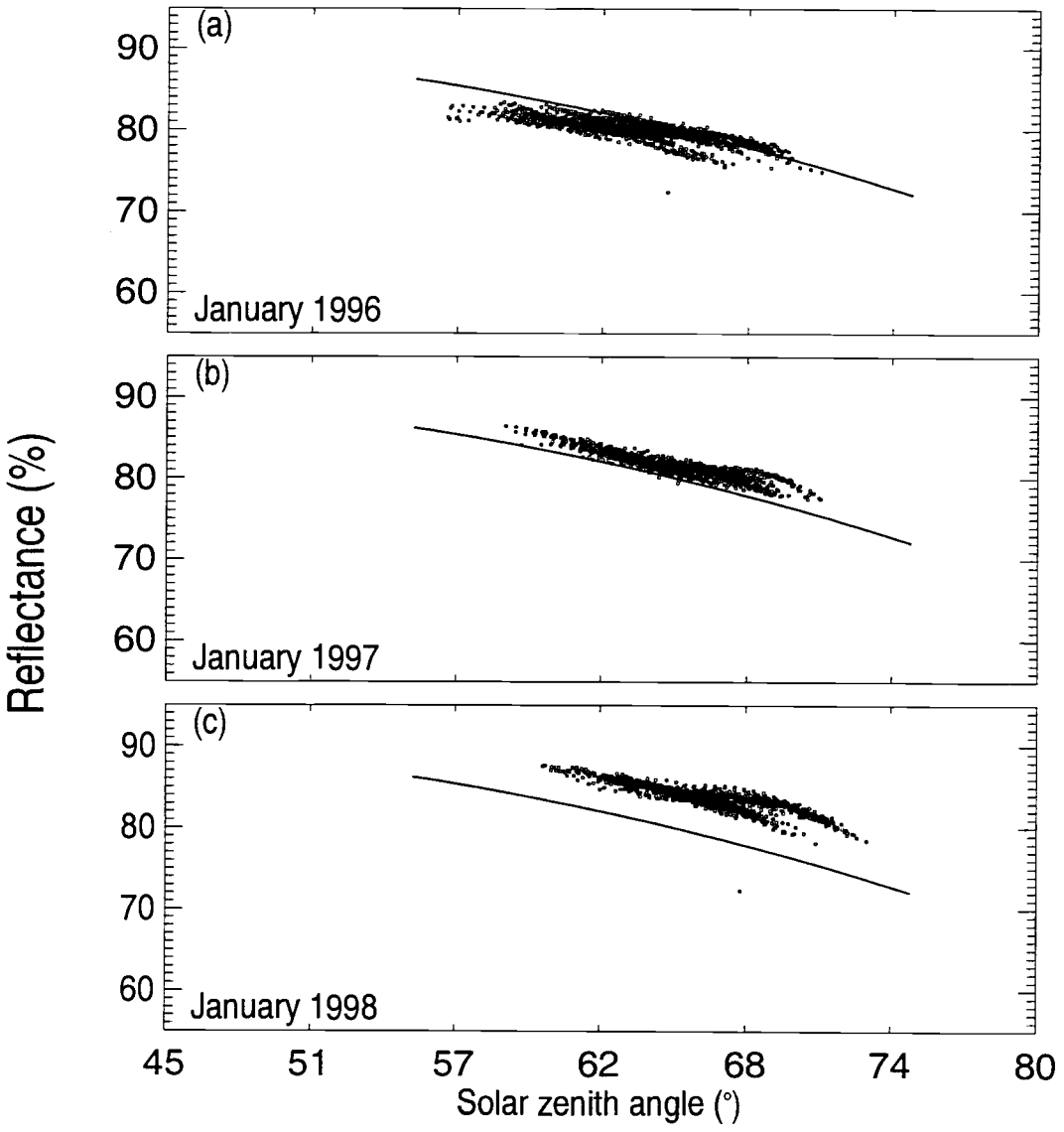

Figure 2.5. NOAA-14 AVHRR Channel 1 reflectances and solar zenith angles for 17×17 pixel subregions with $N < 0{\cdot}6\%$ in (a) January 1996, (b) January 1997, and (c) January 1998 for Antarctica. The solid line represents the NOAA-9 calibration reference for Antarctica, from Loeb (1997). The reflectances are obtained using (2.6a).

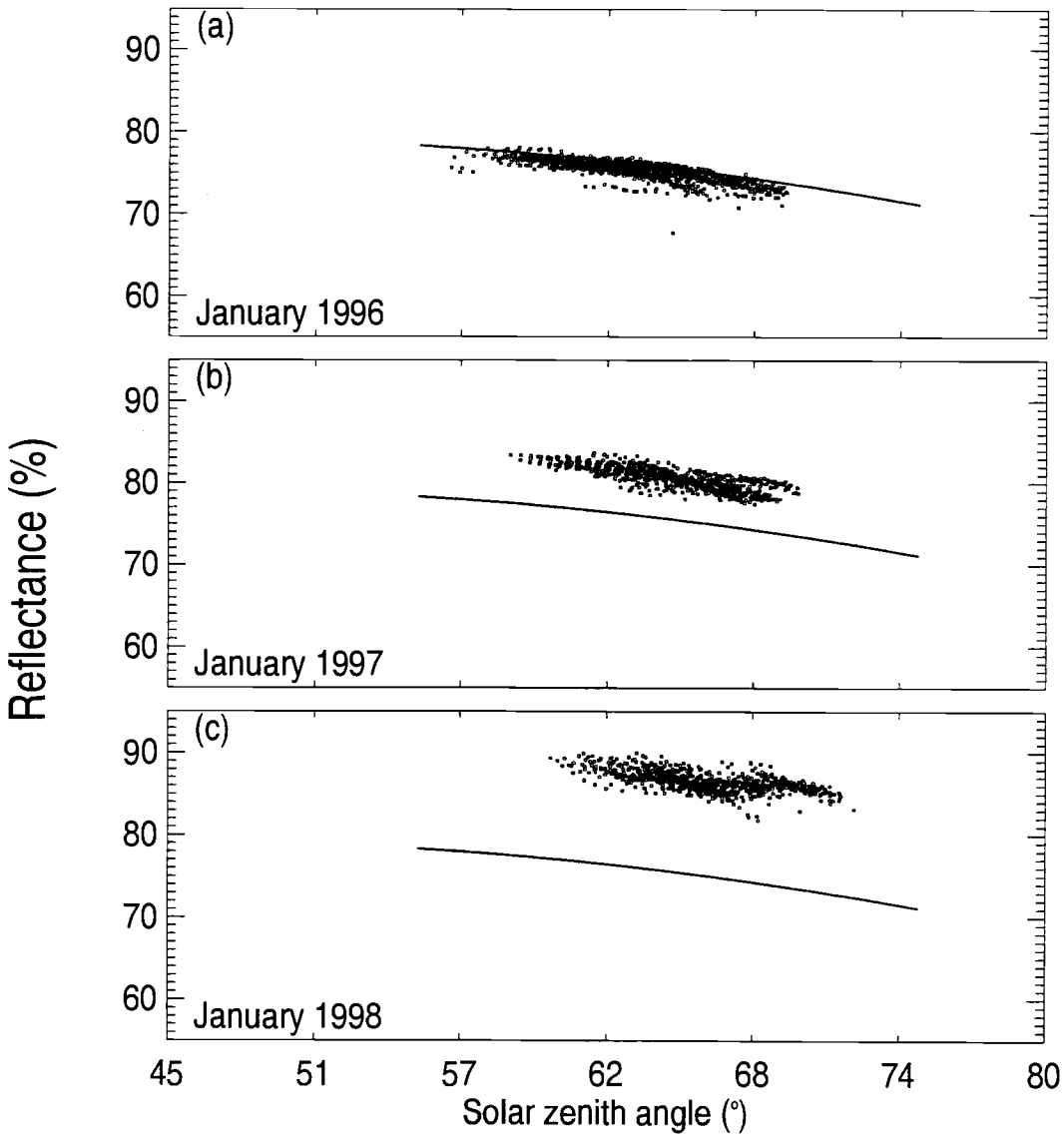

Figure 2.6. NOAA-14 AVHRR Channel 2 reflectances and solar zenith angles for 17 × 17 pixel subregions with $N < 0{\cdot}4\%$ in (a) January 1996, (b) January 1997, and (c) January 1998 for Antarctica. The solid line represents the NOAA-9 calibration reference for Antarctica, from Loeb (1997). The reflectances are obtained using (2.6b).

It is obvious from the trend in the observations in Figs. 2.5 and 2.6 that (2.6a) and (2.6b) were progressively over-compensating for the degradation of the NOAA-14 AVHRR channel 1 and 2 reflectances. Furthermore, the regression lines for the NOAA-9 standard were outside the bounds of the standard errors of estimates of reflectance given by Rao and Chen (1996). Reflectances calibrated with (2.7a) and (2.7b) more closely match the NOAA-9 standard (Figs. 2.7 and 2.8), though year-to-year variations, especially in channel 2, are evident.

New calibration coefficients were developed for NOAA-14 using the NOAA-9 reflectances for Antarctica given by (2.2a) and (2.2b). Based on observed NOAA-14 AVHRR reflectances for 1996-1998, the coefficients are given by

$$R_1 = (0.00001195d + 0.1146) \times (C_{10}^1 - 41) \qquad (2.8a)$$

$$R_2 = (0.000005135d + 0.1432) \times (C_{10}^2 - 41) \qquad (2.8b)$$

The 95% confidence intervals for channel 1 and channel 2 reflectances are 1.5 and 1.7 in units of % reflectance. Figures 2.9 and 2.10 are identical to Figs. 2.7 and 2.8, with the exception that (2.8a) and (2.8b) are used to derive the channel reflectances, in place of the Rao and Chen formulae (2.7a) and (2.7b). The reflectances for small N ($N < 0{\cdot}6\%$ for channel 1 and $N < 0{\cdot}4\%$ for channel 2) are consistent with those derived from the NOAA-9 AVHRR.

In Figs. 2.9 and 2.10, the variability of reflectances observed for a given solar zenith angle is due in part to residual cloud contamination, differences in surface reflectances, and differences in the column concentrations of ozone and water vapor observed for different targets on different days. Cloud contamination and differences in surface reflectances affect both channels. Changes in ozone concentrations, on the other hand, affect primarily the reflectances observed in

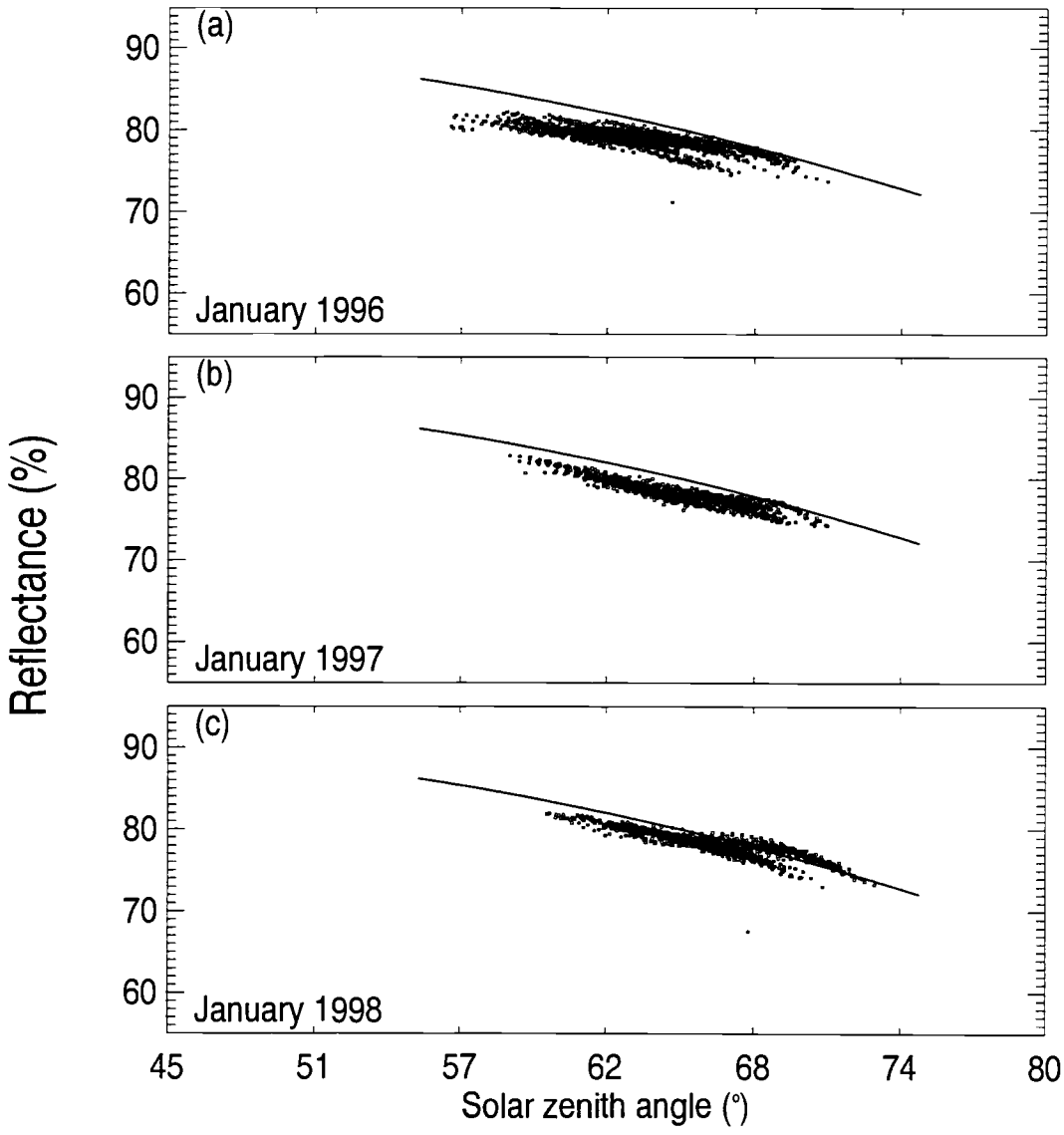

Figure 2.7. NOAA-14 AVHRR Channel 1 reflectances and solar zenith angles for 17 × 17 pixel subregions with $N < 0{\cdot}6\%$ in (a) January 1996, (b) January 1997, and (c) January 1998 for Antarctica. The solid line represents the NOAA-9 calibration reference for Antarctica, from Loeb (1997). The reflectances are obtained using (2.7a).

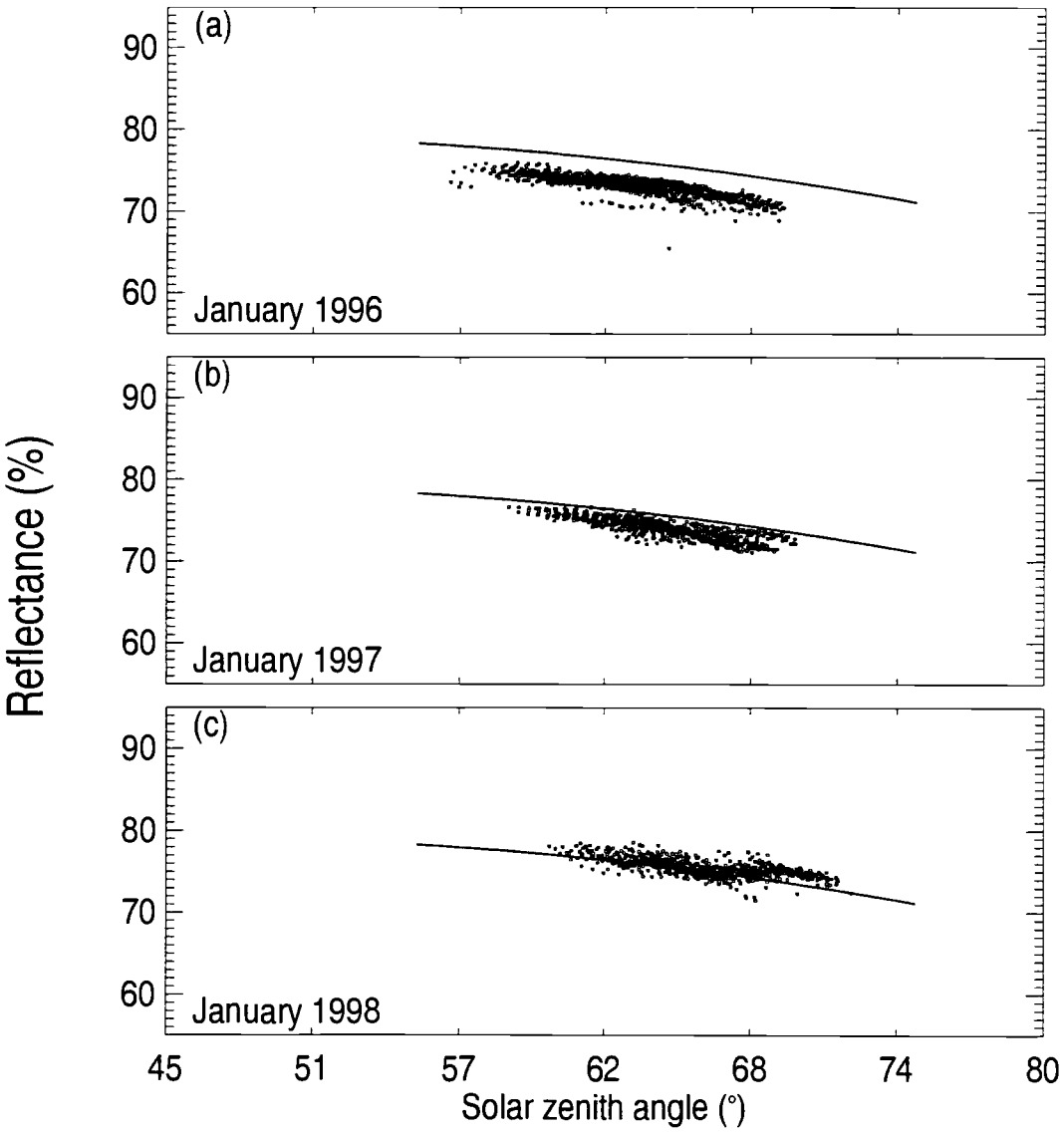

Figure 2.8. NOAA-14 AVHRR Channel 2 reflectances and solar zenith angles for 17 × 17 pixel subregions with $N < 0{\cdot}4\%$ in (a) January 1996, (b) January 1997, and (c) January 1998 for Antarctica. The solid line represents the NOAA-9 calibration reference for Antarctica, from Loeb (1997). The reflectances are obtained using (2.7b).

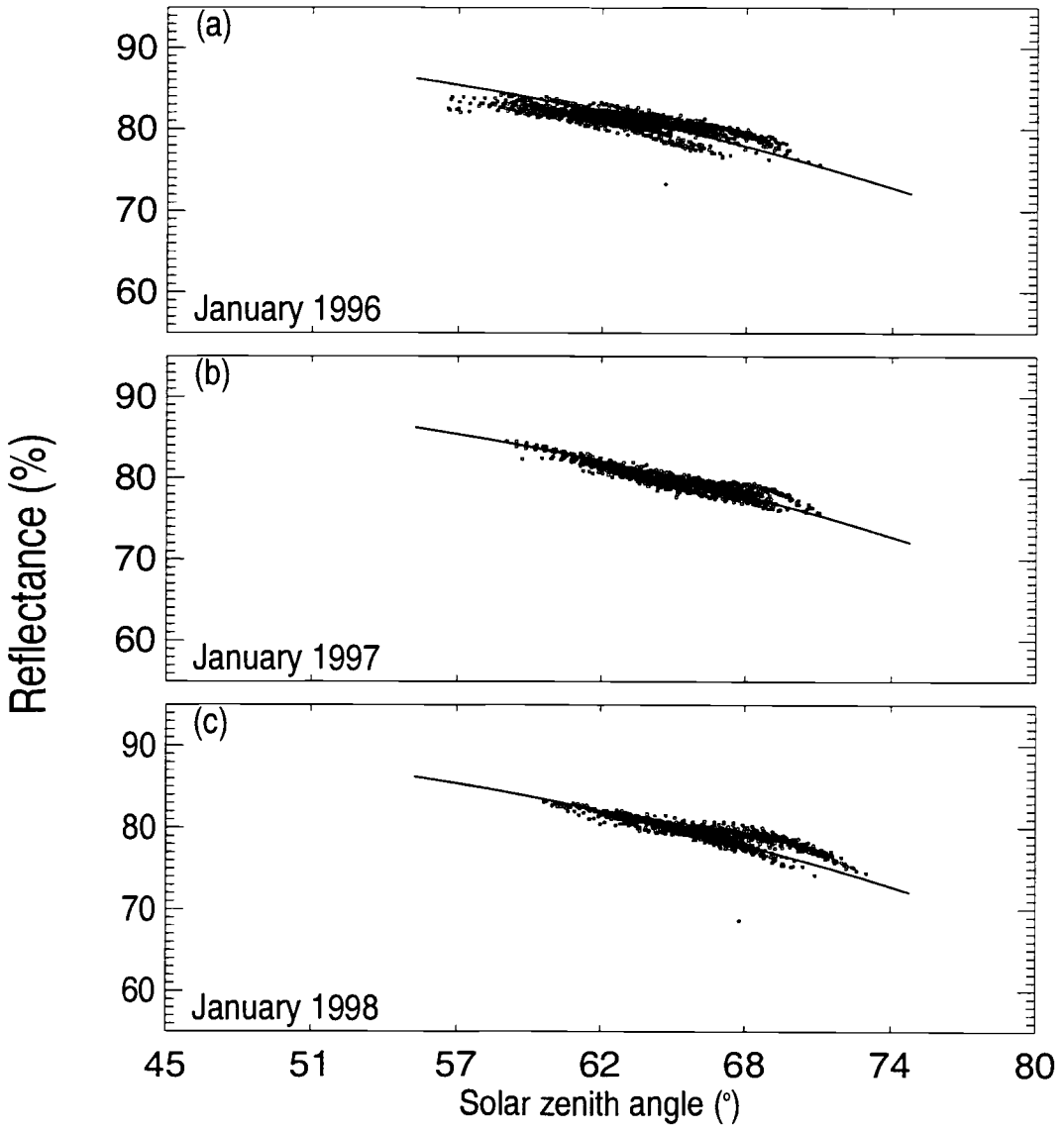

Figure 2.9. NOAA-14 AVHRR Channel 1 reflectances and solar zenith angles for 17 × 17 pixel subregions with $N < 0{\cdot}6\%$ in (a) January 1996, (b) January 1997, and (c) January 1998 for Antarctica. The solid line represents the NOAA-9 calibration reference for Antarctica, from Loeb (1997). The reflectances are obtained using (2.8a).

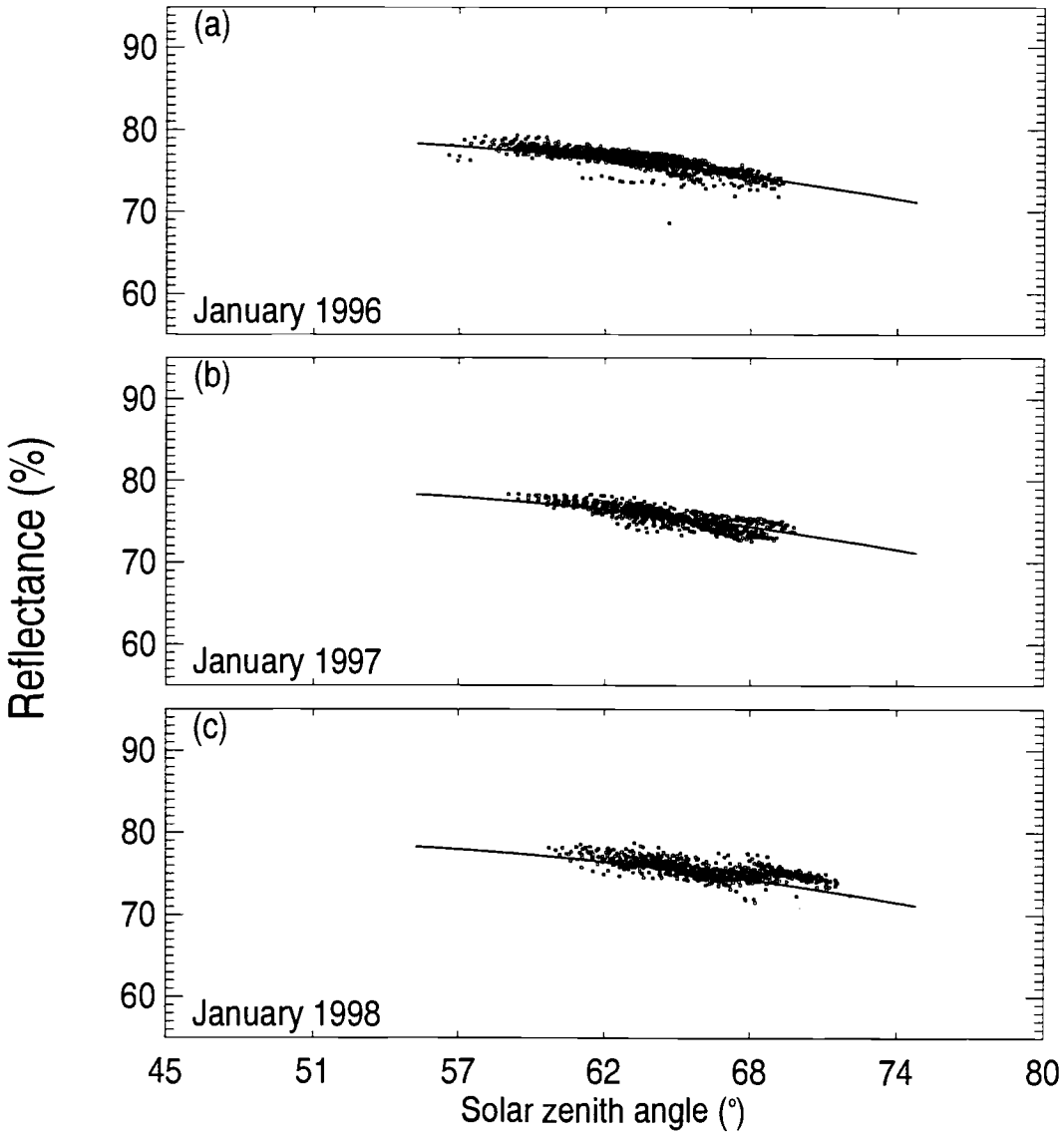

Figure 2.10. NOAA-14 AVHRR Channel 2 reflectances and solar zenith angles for 17 × 17 pixel subregions with $N < 0{\cdot}4\%$ in (a) January 1996, (b) January 1997, and (c) January 1998 for Antarctica. The solid line represents the NOAA-9 calibration reference for Antarctica, from Loeb (1997). The reflectances are obtained using (2.8b).

channel 1, and changes in water vapor concentrations affect primarily the reflectances in channel 2.

Radiative transfer calculations were performed in order to investigate the effects of varying ozone and water vapor concentrations. The calculations were performed using DISORT (Stamnes et al 1988), and include the effects of Rayleigh scattering and absorption by oxygen, ozone, and water vapor. The correlated *k*-distributions described by Kratz (1995) were used to account for molecular absorption. The surface was taken to be Lambertian and the surface albedo was chosen so that the calculated reflectances closely matched those observed. Summertime profiles of temperature, humidity, and ozone for subarctic latitudes (McClatchey et al 1972) were used in the calculations. The results indicate that for nadir views and for a solar zenith angle of 70°, a relatively large change in ozone, 0.1 cm-STP, equivalent to 30% of the summertime average column amount, is required to cause a change in channel 1 reflectances equal to 1.5 in units of % reflectance, the 95% confidence interval for the reflectances given by (2.8a). Likewise, a change equal to about 50% of the water vapor average column amount, which is taken to be 0.8 g cm^{-2} above 2 km, is required to produce a change in channel 2 reflectances equal to 1.7 in % reflectance, the 95% confidence interval for the reflectances given by (2.8b). While variations in the concentrations of ozone and water vapor contribute to the variability of the observed reflectances, most of the variability appears to be due to differences in surface reflectances and residual cloud contamination.

Observations over central Greenland are used to determine the accuracy of (2.8a) and (2.8b). Calibration targets over central Greenland offer the same advantages ascribed to targets in the Antarctic region. Reflectances from GAC formatted NOAA-14 data for the period May and June 1995, 1996, 1997, and 1998 are obtained using (2.8a) and (2.8b), and compared against the reference calibration curves (2.3a) and (2.3b) derived by Loeb (1997) for Greenland. The results for AVHRR channels 1 and 2 are shown in Figures 2.11 and 2.12. Clearly, (2.8a)

provides stable results in channel 1 over Greenland for the period of observation (Fig. 2.11).

Loeb (1997) used AVHRR observations from NOAA-9 ascending and descending orbits over Greenland for June 1985 and 1986 to derive the calibration formulae (2.3a) and (2.3b) represented by the solid lines in Figs. 2.11 and 2.12. Solar zenith angles for the June ascending orbits are typically between 45° and 55° and for descending orbits between 65° and 75°. For May, ascending orbits over Greenland have solar zenith angles between 55° and 65°. The dashed lines in Fig. 2.12 are least squares second order polynomial fits to the May-June set of observations over Greenland for the period 1995 to 1998. While (2.3a) clearly describes reflectance as a function of solar zenith angle for channel 1, independent of the inclusion of May observations, (2.3b) does not satisfactorily describe the solar zenith angle dependence in channel 2 when May data are included.

A new second-order regression equation derived from NOAA-14 AVHRR May and June observations for channel 2 over Greenland is given by

$$R_2' = -53.8125 + 4.64062\theta_0 - 0.041061\theta_0^2, \qquad (2.9)$$

and is represented by the dashed curves in Fig. 2.12, valid for solar zenith angles $48° \leq \theta_0 \leq 78°$.

Observations of Greenland for July and August were analyzed in order to investigate the repeatability of the solar zenith angle-reflectance relationship given by (2.9). Observations for July ascending orbits produced reflectance-solar zenith angle relationships that were identical to the observations for June, while observations for August repeated the relationships obtained for May. This finding reinforces the conclusion that data from May through August may be included in the derivation of calibration coefficients using Greenland.

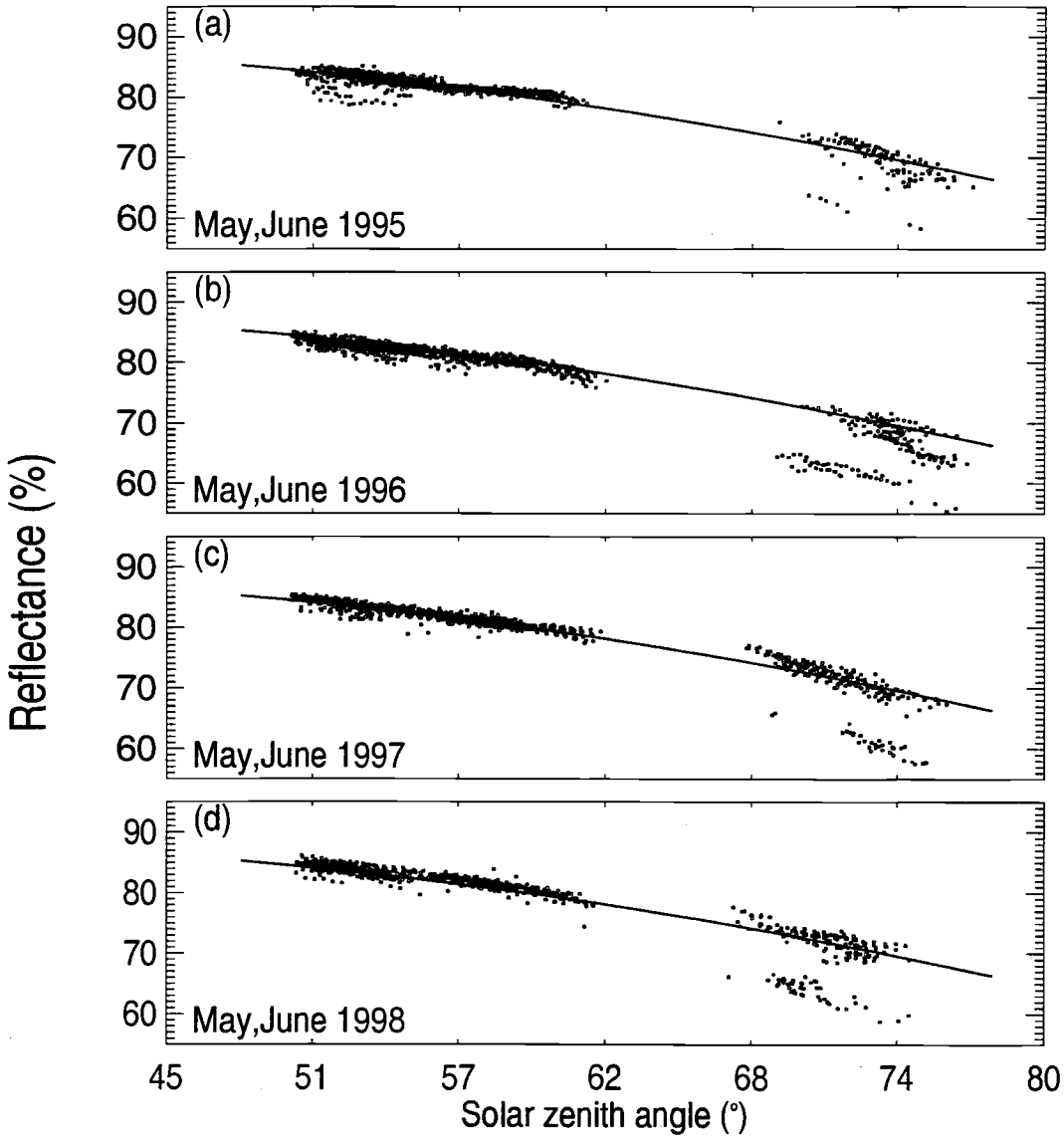

Figure 2.11. NOAA-14 AVHRR Channel 1 reflectances and solar zenith angles for 17 × 17 pixel subregions with $N < 0{\cdot}4\%$ in (a) May, June 1995, (b) May, June 1996, (c) May, June 1997, and (d) May, June 1998 for central Greenland. The solid line represents the NOAA-9 calibration reference for Greenland, from Loeb (1997). The reflectances are obtained using (2.8a).

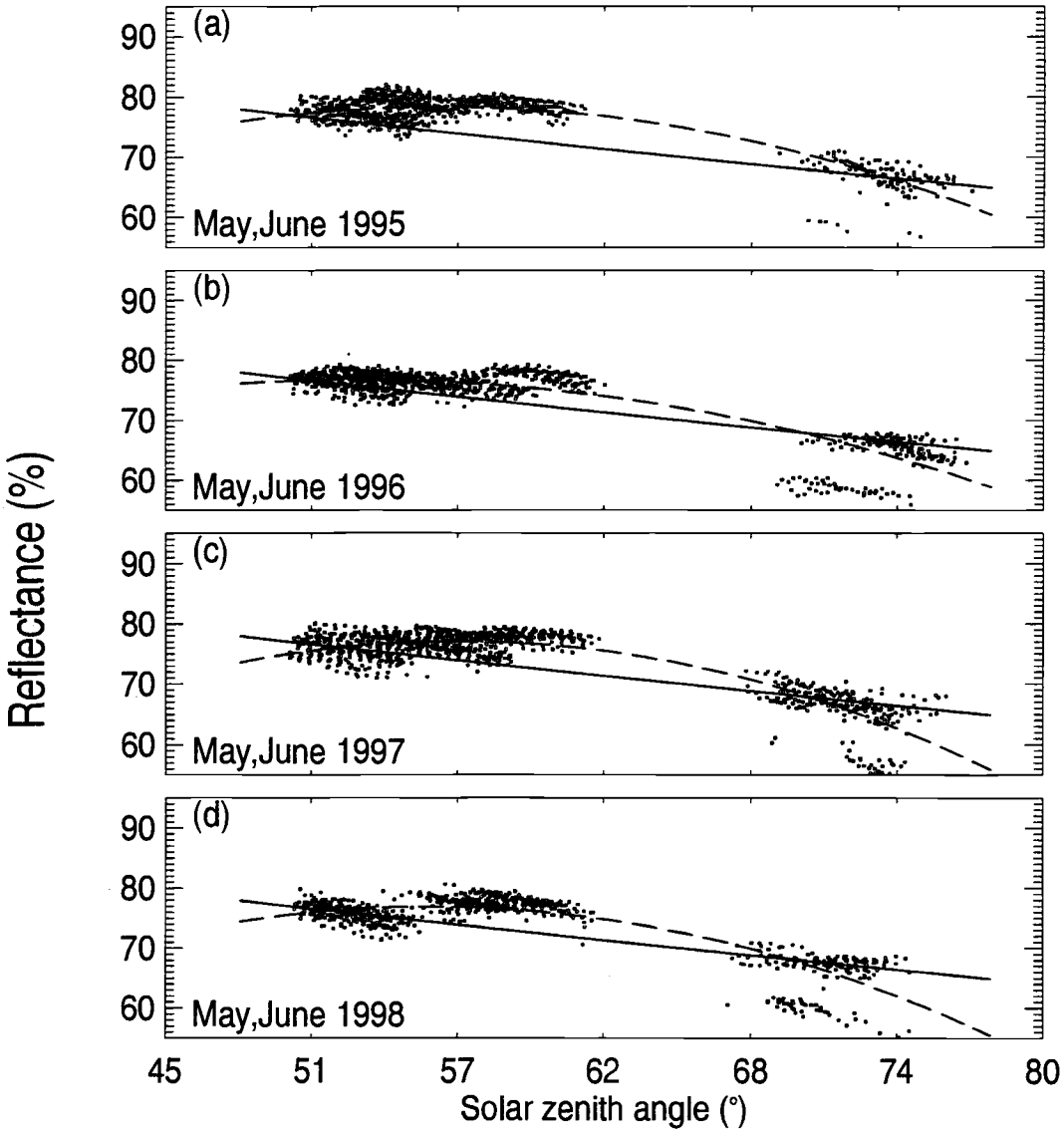

Figure 2.12. NOAA-14 AVHRR Channel 2 reflectances and solar zenith angles for 17 × 17 pixel subregions with $N < 0{\cdot}4\%$ in (a) May, June 1995, (b) May, June 1996, (c) May, June 1997, and (d) May, June 1998 for central Greenland. The dashed line represents a linear least-squares fit to the observations and the solid line represents the NOAA-9 calibration reference for Greenland, from Loeb (1997). The reflectances are obtained using (2.8b).

June descending orbits (observations with solar zenith angles between 65° and 75°) show two distinct clusters of points in Figs. 2.11 and 2.12. For all Greenland passes included in the study, observations were indiscriminately taken from within the region 73N to 78N and 32W to 48W. In the case of June descending passes, it was noted that at high solar zenith angles there were regional differences in the observations with radiance values that were 10% less at lower latitudes (73N to 75N) than at higher latitudes (75N to 78N). The observations with lower reflectances could have been eliminated from the figures by enforcing a stricter cutoff for the index of homogeneity ($N < 0.2\%$) or by limiting the geographic region used as a target. There is, however, little difference in the calibration coefficients obtained using the less restrictive index of homogeneity ($N < 0.4\%$) and larger target area.

Figure 2.13 shows the change in the count-to-reflectance 'slope' with time for channel 1 and 2 reflectances, superimposed on the 'slope' term from (2.8a) and (2.8b) (solid line). The NOAA-9 reference curves given by (2.2a) and (2.2b), are used to derive the 'slopes' for Antarctica channels 1 and 2, and (2.3a) is used to derive the 'slopes' for Greenland channel 1, while (2.9) is used in place of (2.3b) in computing the Greenland channel 2 'slopes'. Also shown are the 'slopes' imbedded in the NOAA-14 Level 1b data stream since December 1998 as given by (2.7a) and (2.7b) (dashed line). Assuming that the targets are stable over time, the calibration coefficients derived in this study would provide stable reflectances for both channels.

2.4 Re-Analysis of NOAA-14 Data to Present

When observations from Antarctica for the period January 1999-2000 were included in the analysis, it was apparent that there was a change in sensor

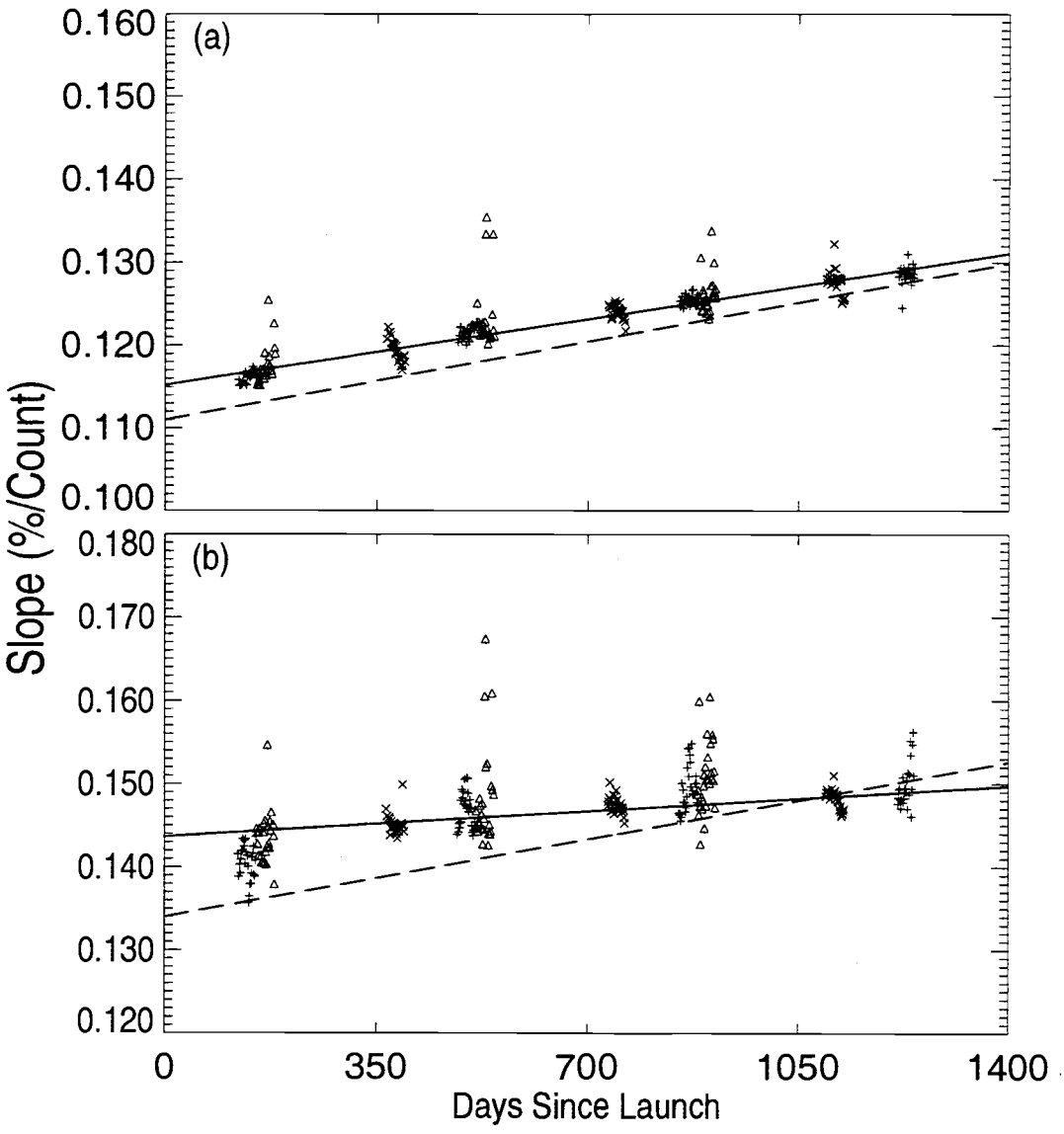

Figure 2.13. Change in slope with time for (a) channel 1 and (b) channel 2 of NOAA-14 AVHRR. Plotted symbols represent daily mean 'slopes' for NOAA-14 passes from May (+) and June (Δ) over Greenland for the period 1995 to 1998, and January (×) over Antarctica for the period 1996 to 1998. The solid line represents the 'slope' term from (2.8a) and (2.8b), and the dashed line represents the 'slope' imbedded in the NOAA-14 Level 1b data stream since December 1998 as given by (2.7a) and (2.7b).

degradation after January 1998. Table 2.2 summarizes the NOAA-14 data from 1999 and 2000 considered in the reanalysis.

Table 2.2. The count of NOAA-14 AVHRR images and sub-regions from 1999 and 2000 considered in the reanalysis.

Month/Year	Region	No. of passes used	No. of sub-regions used
January 1999	Antarctica	31	1018
January 2000	Antarctica	31	1663
May 1999	Greenland	31	845
June 1999	Greenland	30	807
May 2000	Greenland	31	748
June 2000	Greenland	15	367

Figure 2.14 shows reflectances for January 1996-2000 for channels 1 and 2 as a function of solar zenith angle for subregions where the spatial uniformity index, N < 0·6%. The reflectances are obtained using the post-launch coefficients given by (2.5a) and (2.5b). Superimposed on the observations are the NOAA-9 reference calibration curves (2.2a) and (2.2b). Degradation is observed, primarily in channel 1, for the 1996-1998 reflectances. The trend in coefficients appears to reverse in 1999 and 2000.

New calibration coefficients are developed from the 5-years of data for Antarctica using (2.2a) and (2.2b) as a reference. The new coefficients are given by

$$R_1 = (-9.2268\times10^{-9}d^2 + 2.4509\times10^{-5}d + 0.1115)\times(C_{10}^1 - 41) \qquad (2.10a)$$

$$R_2 = (-1.3997\times10^{-9}d^2 + 5.2415\times10^{-6}d + 0.1434)\times(C_{10}^2 - 41) \qquad (2.10b)$$

Figure 2.15 shows the change in the count-to-reflectance 'slope' with time for channel 1 and 2 reflectances, when data from all 5 years are included in the analysis. The solid line represents the 'slope' from (2.10a) and (2.10b), the dotted line represents the 'slope' from (2.8a) and (2.8b), and the dashed line represents the 'slope' imbedded in the NOAA-14 Level 1b data stream since December 1998 as given by (2.7a) and (2.7b).

Observations over the interior zone of the Greenland ice sheet were used to determine the accuracy of (2.10a) and (2.10b). Daily mean 'slopes' for NOAA-14 passes from May and June over Greenland for the period 1995-2000 are plotted in Fig. 2.15. Though the scatter in 'slopes' for Greenland suggests some target instability, the calibration coefficients derived in this study appear to provide stable reflectances for both channels. It was concluded that (2.10a) and (2.10b) should be used to calibrate reflectances for NOAA-14 AVHRR channels 1 and 2.

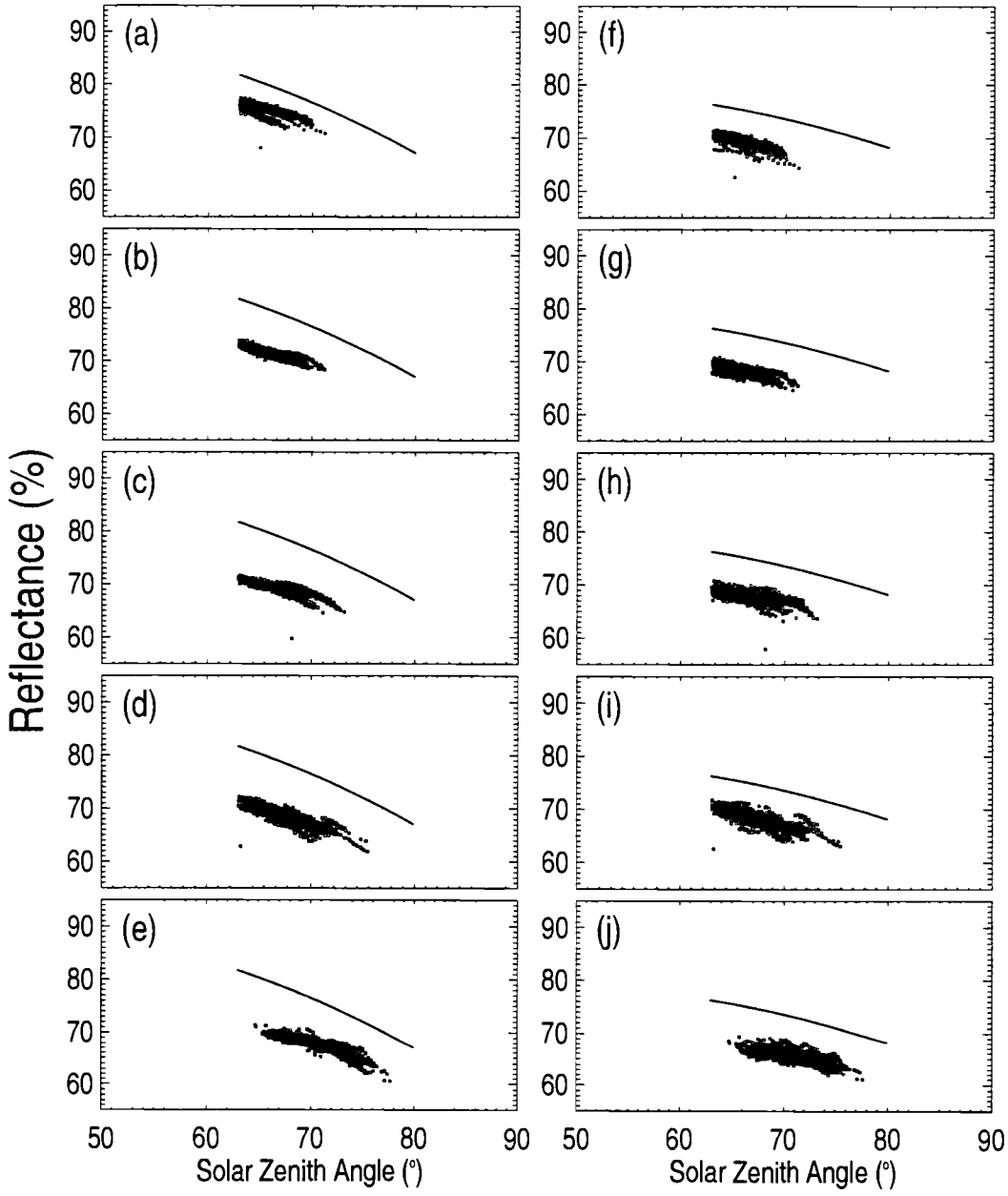

Figure 2.14. NOAA-14 AVHRR Channel 1 and 2 reflectances and solar zenith angles for 17 × 17 pixel subregions with spatial uniformity index, $N < 0{\cdot}6\%$ in January 1996 – 2000 for Antarctica. Parts (a) – (e) represent observations for Channel 1, and parts (f) – (j) for Channel 2. The solid line represents the NOAA-9 calibration reference for Antarctica, from Loeb (1997). The NOAA-14 reflectances are obtained using (2.5a) and (2.5b).

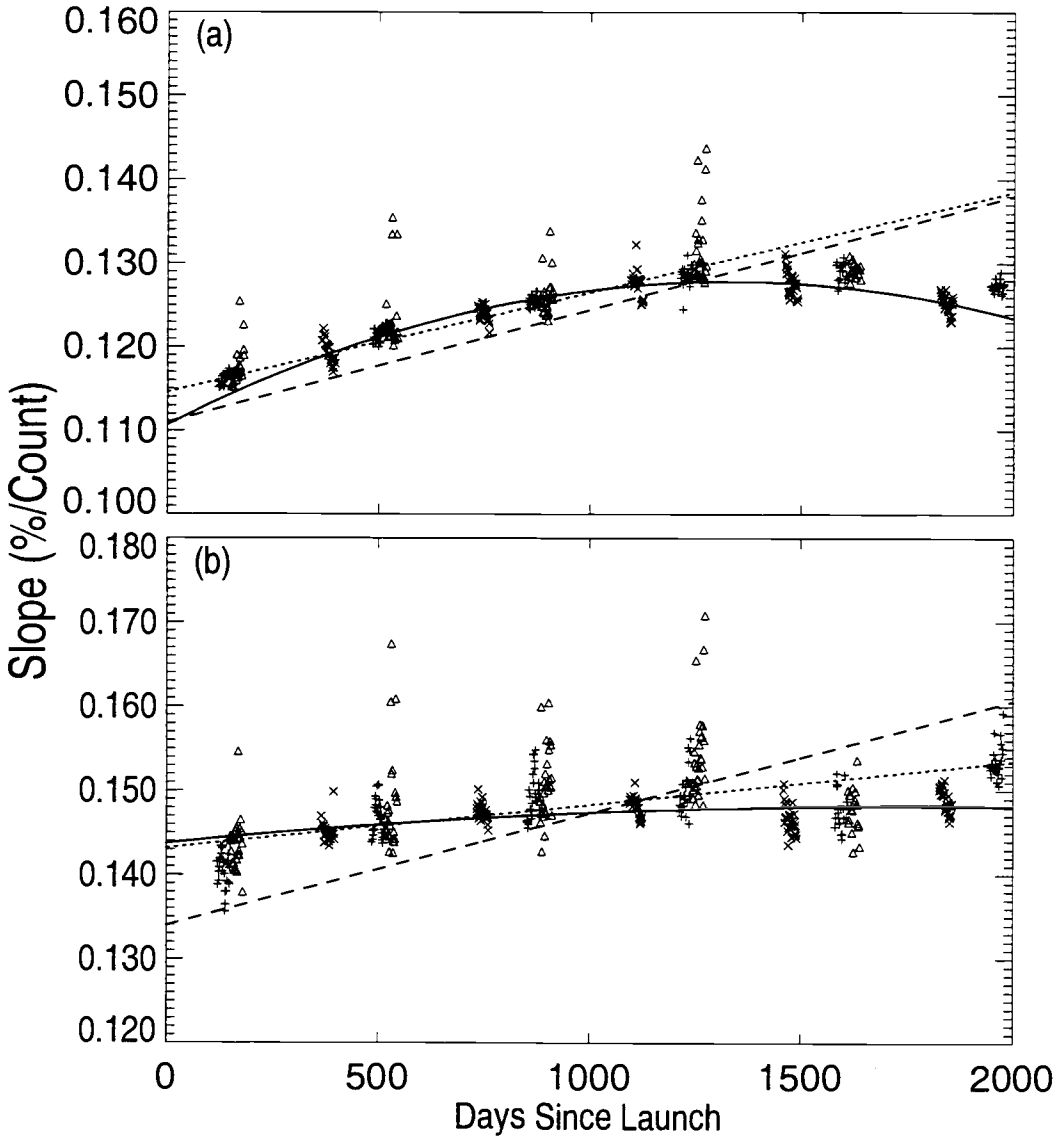

Figure 2.15. Change in slope with time for (a) channel 1 and (b) channel 2 of NOAA-14 AVHRR. Plotted symbols represent daily mean 'slopes' for NOAA-14 passes from May (+) and June (Δ) over Greenland for the period 1995 to 2000, and January (×) over Antarctica for the period 1996 to 2000. The solid line represents the 'slope' from (2.10a) and (2.10b), the dotted line represents the 'slope' from (2.8a) and (2.8b), and the dashed line represents the 'slope' imbedded in the NOAA-14 Level 1b data stream since December 1998 as given by (2.7a) and (2.7b).

Chapter 3
A Review of Aerosols and Their Size Distributions

3.1 Introduction

Laboratory and *in situ* measurements have shown that aerosol optical parameters are difficult to unambiguously specify owing to their wide range of physical characteristics. Aerosol particles in the atmosphere vary greatly in their source, composition, size, concentration, and optical properties. Of all properties of aerosols, though, none dominates their optical behavior more nor is as difficult to study experimentally as size.

Particles of all types scatter light. The particles with diameters greater than 1 micron scatter visible light proportional to the square of the diameter, while particles with diameters much less than 0.1 micron scatter visible light proportional to the fourth power of the diameter. The size spectrum and composition are of particular interest due to their impact on the optical properties of the aerosol particles. Aerosols of all types cover a size spectrum that extends over almost four orders of magnitude. Different parts of the particle size spectrum are responsible for different phenomena in the atmosphere. Of significance to this study are particles responsible for scattering and absorbing visible and infrared light.

Numerous measurements of aerosol optical and physical properties have been made from surface, shipborne, and airborne platforms. These measurements have led to the development of aerosol models in which the aerosol composition, concentration, optical properties, and size distribution are specified as a function of relative humidity. Given the optical properties and a size distribution, the light scattering and absorption properties of an aerosol can be determined using Mie theory.

3.2 Mie Theory

In applying Mie theory, a number of assumptions about the scattering medium and the scattering particles are often invoked. First, the particles are assumed to be spherical. In addition, it is assumed that all particles of a given type have the same complex index of refraction for a given wavelength of incident light, and the complex index of refraction is uniform within each particle.

Derivations of the Mie solution have been described in detail by a number of authors, notably by Stratton (1941) and by van de Hulst (1957). When incident plane-wave radiation interacts with a single homogeneous sphere, part of the incident energy will be scattered. The scattered radiation field is described by a scattering matrix. Mie theory provides a solution for the scattering matrix in the form of two infinite converging series given by

$$S_1(m,x,\theta)=\sum_{n=1}^{\infty}\frac{2n+1}{n(n+1)}(a_n\pi_n+b_n\tau_n) \tag{3.1}$$

$$S_2(m,x,\theta)=\sum_{n=1}^{\infty}\frac{2n+1}{n(n+1)}(b_n\pi_n+a_n\tau_n), \tag{3.2}$$

where S_1 and S_2 are dimensionless complex amplitudes which are functions of the complex index of refraction m, the Mie size parameter x, with $x=\frac{2\pi r}{\lambda}$, and the scattering angle θ. The Mie coefficients a_n and b_n, are functions of m and x only, and the angular functions π_n and τ_n are functions of $\mu=\cos\theta$ only. The Mie

coefficients are used to calculate the scattering and extinction efficiency factors Q_{sca} and Q_{ext}, the asymmetry parameter g, which denotes the relative strength of forward scattering, and the scattering and extinction cross sections σ_{sca} and σ_{ext}, which are computed from the product of the geometric cross section of the scattering sphere and Q_{sca} and Q_{ext}, respectively. The asymmetry parameter g is the average cosine of the scattering angle and is given by

$$g = \langle \cos\Theta \rangle = \int_{4\pi} \cos\Theta P(\Theta) \frac{d\Omega}{4\pi} \tag{3.3}$$

where Θ is the scattering angle, $P(\Theta)$ is the phase function, and Ω is a solid angle representing the cone of scattered radiation.

Since each particle intercepting incident radiation scatters an amount of light proportional to the scattering cross section σ_{sca} ($\sigma_{sca} = Q_{sca}\pi r^2$), it is useful to describe the scattered light in terms of the particle effective radius and effective variance for the size distribution. The effective radius, r_{eff}, and the effective variance, v_{eff}, are given by

$$r_{eff} = \frac{\int_{r_1}^{r_2} r\pi r^2 n(r)dr}{\int_{r_1}^{r_2} \pi r^2 n(r)dr} = \frac{1}{G}\int_{r_1}^{r_2} r\pi r^2 n(r)dr \tag{3.4}$$

$$v_{eff} = \frac{1}{Gr_{eff}^2}\int_{r_1}^{r_2} (r - r_{eff})^2 \pi r^2 n(r)dr, \tag{3.5}$$

where G is the geometric cross-sectional area of particles per unit volume and $n(r)$ is the particle number density. Other useful scattering quantities that can be calculated for a size distribution are $<Q_{sca}>$, the effective scattering efficiency factor, given by

$$<Q_{sca}>=\frac{\int_{r_1}^{r_2} Q_{sca}(r)\pi r^2 n(r)dr}{\int_{r_1}^{r_2} \pi r^2 n(r)dr}, \tag{3.6}$$

$<Q_{ext}>$, the effective extinction efficiency factor, given by

$$<Q_{ext}>=\frac{\int_{r_1}^{r_2} Q_{ext}(r)\pi r^2 n(r)dr}{\int_{r_1}^{r_2} \pi r^2 n(r)dr}, \tag{3.7}$$

ω_{eff}, the effective single scattering albedo, given by

$$\omega_{eff}=\frac{\int_{r_1}^{r_2} Q_{sca}(r)\pi r^2 n(r)dr}{\int_{r_1}^{r_2} Q_{ext}(r)\pi r^2 n(r)dr}, \tag{3.8}$$

and g_{eff}, the effective asymmetry parameter, given by

$$g_{eff}=\frac{\int_{r_1}^{r_2} Q_{sca}(r)g(r)\pi r^2 n(r)dr}{\int_{r_1}^{r_2} Q_{sca}(r)\pi r^2 n(r)dr}. \tag{3.9}$$

The mathematical derivation of optical properties such as single scattering albedo and scattering phase function requires knowledge of the size distribution and the complex index of refraction. Thus, it is important that the correct size distribution and aerosol model be used to characterize an atmospheric layer.

3.3 Standard Size Distributions

Based on extensive *in situ* measurements of the physical properties of aerosols, three distribution functions are commonly used to characterize the size distribution of atmospheric aerosols. These are discussed below.

3.3.1 The Modified Gamma Distribution

Deirmendjian (1964) used a family of distribution functions to compute optical properties for a number of different haze, cloud, and rain models. To account for the multi-modal nature of atmospheric aerosols with n species, the modified gamma distribution, in its most general form, is given by

$$n(r) = \frac{dN(r)}{dr} = \sum_{i=1}^{n} N_i a_i r^{\alpha_i} \exp(-b_i r^{\gamma_i}) \qquad 0 \le r < \infty \quad (3.10)$$

and reduces to the standard gamma distribution,

$$n(r) = \frac{dN(r)}{dr} = \sum_{i=1}^{n} N_i a_i r^{\alpha_i} \exp(-b_i r) \qquad 0 \le r < \infty \quad (3.11)$$

when $\gamma = 1$.

The gamma distribution with variations has been used for studying cloud and haze particles, notably by Khrgian and Mazin (1952) and Deirmendjian (1964), but in general is not often used because a, b, α, and γ are not easily related to physical quantities such as particle mass or cross section.

3.3.2 The Log Normal Distribution

An analysis of *in situ* measurements of particle size under a variety of conditions has shown that natural aerosols consist of fairly independent groups of particles. The log normal distribution function was introduced by Davies (1974) specifically to account for the presence of large particles in an aerosol suspension of mainly small particles. To account for the multi-modal nature of atmospheric aerosols with n species, the log normal distribution, in its most general form, is given by

$$n(r) = \frac{dN(r)}{dr} = \sum_{i=1}^{n} \frac{N_i}{(2\pi)^{1/2}\sigma_i} \frac{1}{r} \exp\left[-\frac{\left(\ln \frac{r}{r_i} \right)^2}{2\sigma_i^{\,2}} \right], \qquad (3.12)$$

where r_i is the median radius of the particle for species i and σ_i is the standard deviation of the log normal distribution, with the variance given by

$$\sigma_i^2 = \int_0^\infty \left(\ln \frac{r}{r_i} \right)^2 f\left(\ln \frac{r}{r_i} \right) \frac{dr}{r}. \tag{3.13}$$

If the lognormal distribution is specified in terms of r_{eff}, the effective radius, and v_{eff}, the effective variance, r_{eff} and v_{eff} are related to r_i and σ (Nakajima and King, 1990) by

$$r_{eff} = r_i \exp\left[\frac{5\sigma^2}{2} \right] \tag{3.14}$$

and

$$v_{eff} = e^{\sigma^2} - 1. \tag{3.15}$$

3.3.3 The Junge Power Law

Junge (1963) introduced the power law function as a convenient way to illustrate the aerosol size distribution. Though it does not accurately account for large particles, it is nevertheless useful as a means of obtaining information about particle size. The power law function is in the form

$$\frac{dN}{d \log r} = C r^{-p}, \tag{3.16}$$

where C is a constant and p is a size parameter typically varying between 3 and 5. The optical depth is related to Ångström's turbidity coefficient β by

$$\tau(\lambda) = \beta\lambda^{-\alpha}, \tag{3.17}$$

and to α directly by

$$\tau_\lambda = \tau_o\left(\frac{\lambda}{\lambda_o}\right)^{-\alpha}, \tag{3.18}$$

where the subscript 0 refers to a reference wavelength, and α, the wavelength exponent, is related to the size parameter p in (3.16) through a simple first-order polynomial expression, that can be derived using Mie calculations (Nakajima and Higurashi, 1997). The value of α ranges from approximately 0 for large scatterers to 4 for Rayleigh scattering, with values of approximately 1.3 for average atmospheric aerosol. The advantage of the power law is that the size distribution can be specified simply in terms of a single parameter, p.

3.4 Comparison of Standard Size Distributions

Hansen and Travis (1974) used the three basic distribution functions to demonstrate the sensitivity of the phase function to the shape of the size distribution. Holding the particle effective radius and variance constant permits comparison of a set of size distributions. Single scattering intensities are computed using the complex index of refraction for pure water (m=1·33-0i) at a wavelength

of 0·55 μm. The parameters in each distribution are chosen such that r_{eff} = 1.0 μm and v_{eff} = 0·25. The form of the distributions used in the comparison are given below.

3.4.1 Single Mode Gamma Distribution for Comparison

A modified gamma size distribution first used by Hansen (1971) to make theoretical computations of aerosol optical properties is of the form

$$n(r) = Cr^{\frac{1-3b}{b}} \exp[-r/ab]], \tag{3.19}$$

where

$$C = \frac{N(ab)^{\frac{2b-1}{b}}}{\Gamma\left[\frac{1-2b}{b}\right]}, \tag{3.20}$$

and $\Gamma\left[\frac{1-2b}{b}\right]$, the gamma function, is given by

$$\Gamma\left[\frac{1-2b}{b}\right] = \sum_{n=1}^{\infty} (n-0.5)^{\frac{1-2b}{b}-1} \exp[-(n-0.5)]. \tag{3.21}$$

N represents the total number of particles per unit volume (normalized to 1·0 cm^{-3} for this study).

The Hansen form of the modified gamma distribution has the simple property that $a = r_{eff}$ and $b = v_{eff}$. As a consequence of setting $a = r_{eff}$ = 1 μm and $b = v_{eff}$ = 0·25, the arithmetic mean radius becomes

$$\bar{r} = a(1-2b) = 0.5\,\mu\text{m} \tag{3.22}$$

and the variance becomes

$$\sigma^2 = a^2 b(1-2b) = 0.125\,(\mu\text{m})^2. \tag{3.23}$$

The parameters in the other distributions examined in this study are chosen such that these values for $\bar{r}$ and σ^2 are conserved.

3.4.2 Bimodal Gamma Distribution for Comparison

The bimodal gamma distribution function is simply the sum of two Hansen modified gamma distributions (3.19), with each term containing half the particles. The sum of two log normal functions is frequently used to model a bimodal size distribution as well as a mixed layer consisting of two distinct aerosol components. The bimodal gamma distribution takes the form

$$n(r) = \frac{1}{2}\frac{Nr^{\frac{1-3b}{b}} e^{-\frac{r}{a_1 b}}}{(a_1 b)^{\frac{1-2b}{b}}\Gamma\left[\frac{1-2b}{b}\right]} + \frac{1}{2}\frac{Nr^{\frac{1-3b}{b}} e^{-\frac{r}{a_2 b}}}{(a_2 b)^{\frac{1-2b}{b}}\Gamma\left[\frac{1-2b}{b}\right]}, \tag{3.24}$$

where each of the two terms has the same meaning as in (3.19), with b and N constant for both terms. Values for $\bar{r}$ = 0·5 μm and σ^2 = 0·125 $(\mu\text{m})^2$ requires

that $b = 0{\cdot}0357$ and $a_1 = 0{\cdot}1795$ μm, and by arbitrarily choosing $a_2 = 5a_1$, then $a_2 = 0{\cdot}8975$ μm. For the same values of $\bar{r}$ and σ^2, $r_i = 0{\cdot}4082$ μm, as given by (3.15) and $\sigma_i = 0{\cdot}6368$ μm, based on (3.16).

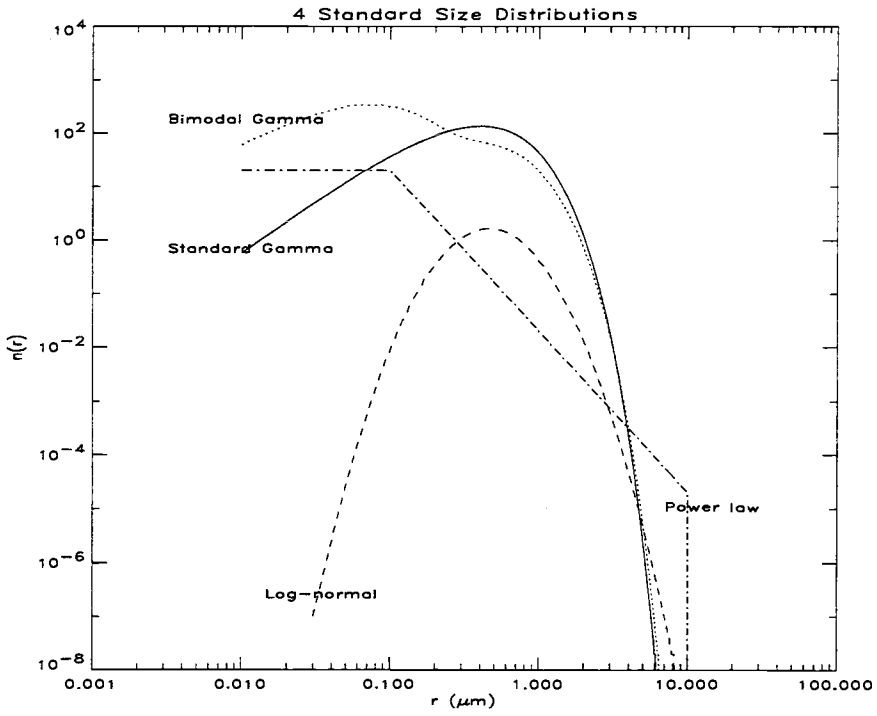

Figure 3.1. Modified gamma, bimodal gamma, log normal, and power law size distribution functions with parameters chosen such that $r_{\text{eff}} = 1$ μm and $v_{\text{eff}} = 0{\cdot}25$.

3.4.3 Power Law Distribution for Comparison

The Hansen and Travis form of this function is chosen such that the power law is proportional to r^{-3}. The Hansen and Travis power law distribution is given by

$$n(r) = \frac{2r_1^{\,2}r_2^{\,2}}{r_2^{\,2} - r_1^{\,2}} r_1^{-3} \quad \text{for} \quad r_1 \le r \le r_2, \tag{3.25a}$$

$$n(r) = 0 \quad \text{otherwise.} \tag{3.25b}$$

Choosing values $\bar{r}$ = 0·5 μm and σ^2 = 0·125 (μm)^2 requires that r_1 = 0·2690 μm, and r_2 = 3·535 μm.

3.4.4 Single Mode Log Normal Distribution for Comparison

The log normal function used by Hansen and Travis is as follows:

$$n(r) = \frac{dN(r)}{dr} = \frac{1}{(2\pi)^{1/2}\sigma_g} \frac{1}{r} \exp\left[-\frac{\left(\ln \frac{r}{r_g} \right)^2}{2\sigma_g^{\,2}} \right], \tag{3.26}$$

where r_g is the mode radius of the particle and σ_g is the standard deviation of r.

Figure 3.1 shows number density as a function of particle size over the range 0·005 to 100 μm. The parameters in each distribution are chosen such that the effective radius and effective variance are conserved. Figure 3.2 shows the single

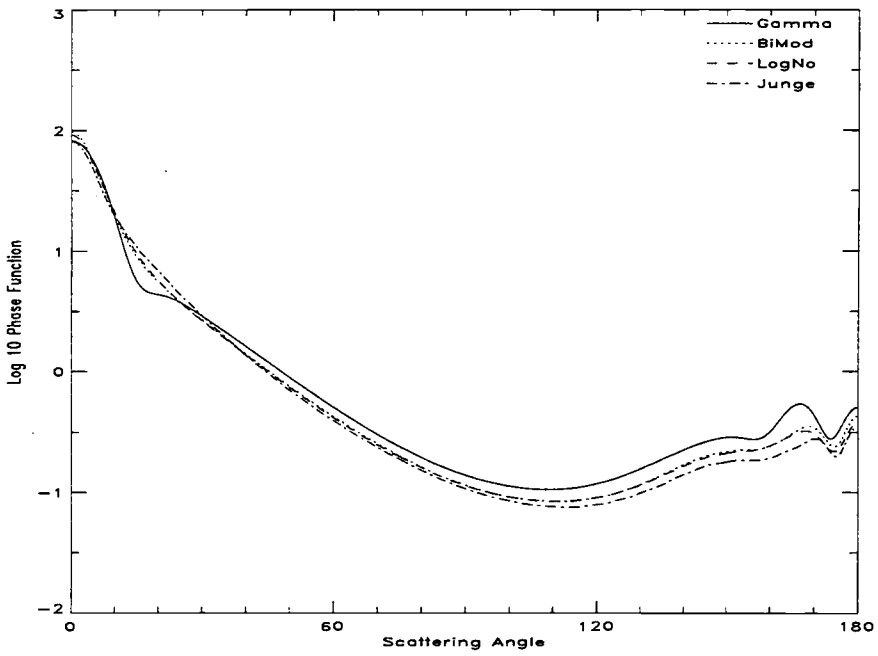

Figure 3.2. Phase function for the four size distributions shown in Fig. 3.1. The calculations are for pure water (real refractive index=1·33, no absorption), and wavelength $\lambda = 0{\cdot}55$ μm.

scattering intensity for the four size distributions in Fig. 3.1. The computations are done for done for pure liquid water (complex index of refraction m = 1·33-0*i*) and wavelength $\lambda = 0{\cdot}55$ μm.

The four adjustable constants used in the general form of the modified gamma distribution (3.10) give it great flexibility and make it ideal for use in characterizing various haze and cloud drop models. Deirmendjian (1964) used the modified gamma distribution in the form

$$n(r) = ar^{\alpha} \exp\left(-br^{\gamma}\right), \tag{3.27}$$

where N, the total particle number density, is found by integrating over the entire range of particle radius using

$$N = a\int_0^\infty r^\alpha \exp\left(-br^\gamma\right)dr, \tag{3.28}$$

which, after integration, becomes

$$N = a\gamma^{-1}b^{-\frac{\alpha+1}{\gamma}}\Gamma\left[\frac{\alpha+1}{\gamma}\right], \tag{3.29}$$

where $\Gamma\left[\frac{\alpha+1}{\gamma}\right]$, the gamma function, is given by

$$\Gamma\left[\frac{\alpha+1}{\gamma}\right] = \int_0^\infty t^{\frac{\alpha+1}{\gamma}-1}e^{-t}dt. \tag{3.30}$$

Thus a is given by N. Figure 3.3 shows Haze and Cloud number distributions as a function of size using the values for a, b, α, and γ given in Table 3.1 (from Deirmendjian, 1969). Figure 3.4 shows the corresponding phase function for the Haze L and Cloud C1 distributions shown in Fig. 3.3.

The parameters for each of the haze types are chosen as follows: type L represents continental aerosol; type M represents an oceanic or coastal distribution; and type H represents the size distribution of fine particles, such as stratospheric aerosol, or a layer of suspended dust. For water droplets, the cloud type C1 represents the cloud drop size distribution found in cumulus clouds of moderate thickness and represents the predominant case. In spite of the flexibility demonstrated here in the use of the 4 constants a, b, α, and γ for fitting the log normal distribution to various models of haze and water drops, the four adjustable constants make the function difficult to handle and they are not readily linked to physical quantities such as mass concentration or average cross sections.

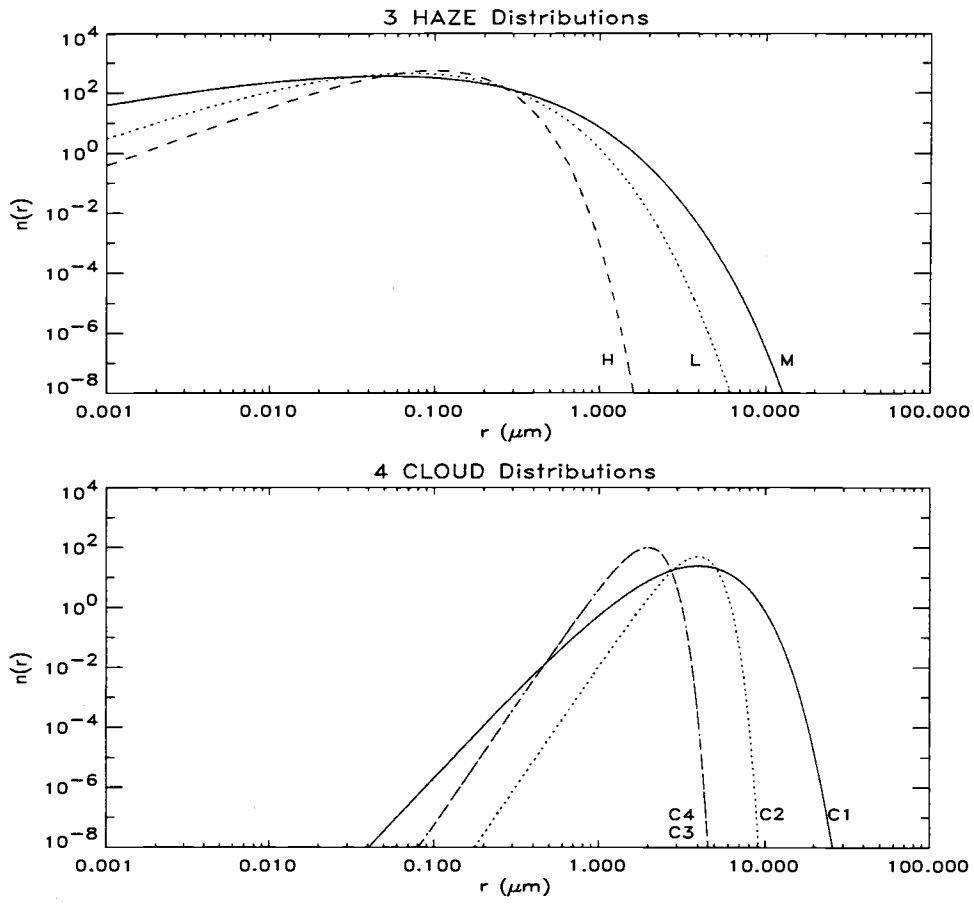

Figure 3.3. Haze-type and Cloud-type distributions from Deirmendjian (1964) for the parameters given in Table 3.1.

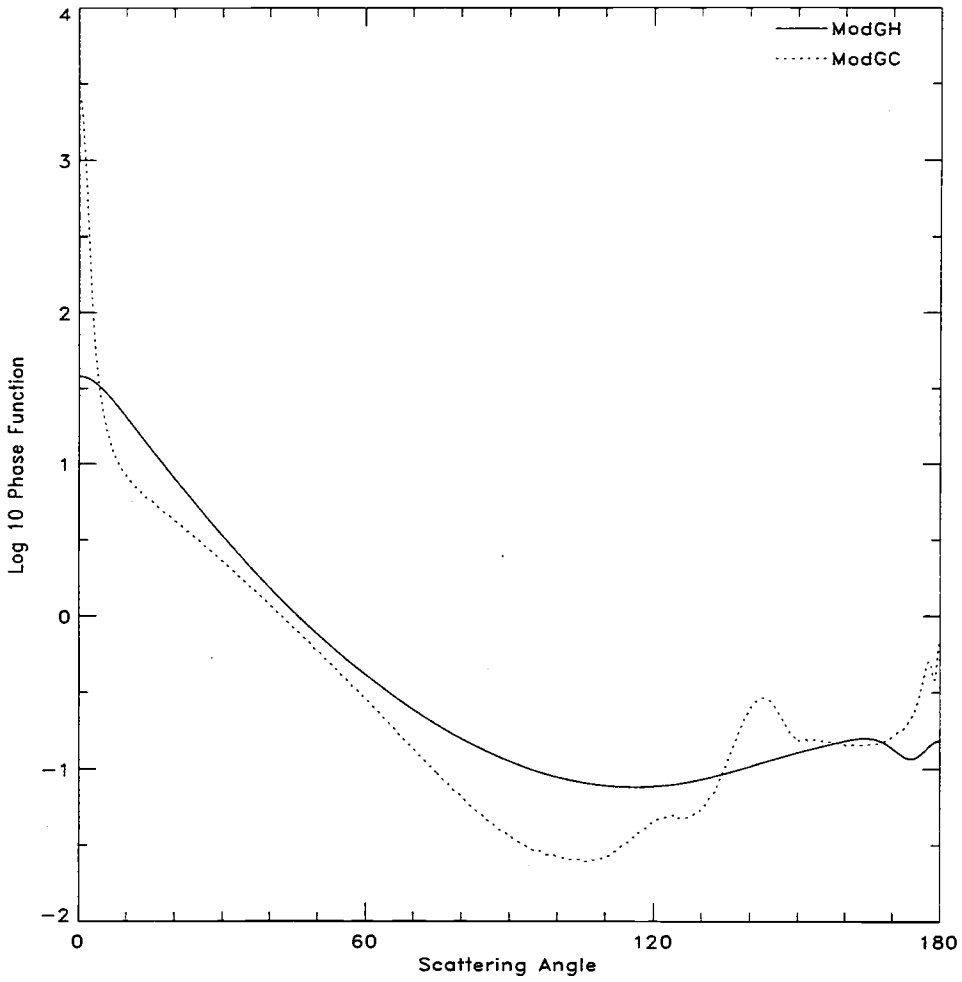

Figure 3.4. Phase function for the Haze L (ModGH) and Cloud C1 (ModGC) distributions shown in Fig. 3.3. The calculations are for pure water (real refractive index=1·33, no absorption), and wavelength $\lambda = 0{\cdot}55$ μm.

Table 3.1. Numerical parameters used in the modified gamma distribution (3.28) to construct various cloud and haze models (from Deirmendjian, 1969). Haze types represented are L (continental aerosol), M (marine or coastal aerosol), and H (stratospheric aerosol or dust). The cloud types are C1 (cumulus clouds of moderate thickness), C2 (same droplets size as C1 but narrower distribution), C3 (high cloud), and C4 (high cloud, smaller size than C3).

	a	b	α	γ
Haze M	5.3333×10^{4}	8.9443	1	0.5
Haze L	4.9757×10^{6}	15.1186	2	0.5
Haze H	4.0000×10^{5}	20.0000	2	1
Cloud C1	2.3730	1.5	6	1
Cloud C2	1.0851×10^{-2}	.04167	8	3
Cloud C3	5.5556	.33333	8	3
Cloud C4	5.5556	.33333	8	3

Size distributions are obtained by a variety of techniques, both experimental and mathematical. The size distribution can be derived from the spectral dependence of optical depths using inversion techniques (King et al., 1984; Stone et al., 1993). Where instruments such as cascade impactors and optical counters are used to make *in situ* measurements, the size distribution can be obtained directly (Patterson and Gillette, 1977; Sverdrup et al., 1975). Of the many distribution functions available, the log normal function is typically used because its parameters are readily linked to the moments of the distribution. For example, the number and volume moments are related by

$$\ln r_v = \ln r_n + 3(\ln \sigma_n)^2, \tag{3.31}$$

and the number and surface moments by

$$\ln r_s = \ln r_n + 2(\ln \sigma_n)^2, \tag{3.32}$$

where r_n and σ_n are the number mean radius and standard deviation from (3.12), r_s is the surface mean radius, and r_v is the volume mean radius. The number distribution is used in calculating the scattering properties of an aerosol layer using Mie theory, even though the total optical extinction, which impacts visibility, is closely related to the surface mode. Soil-derived particles eroded by the wind, and stratospheric aerosols of volcanic origin are often characterized by a size distribution with more than one mode. But this mode structure is more clearly seen in either the volume or the surface distribution than in the number distribution (Whitby et. al. 1972).

3.5 Sensitivity Studies

As discussed in the Introduction, a primary objective of this study was the determination of aerosol direct radiative forcing for cloud-free pixels in the INDOEX region. To do so, estimates of aerosol burdens were generated from NOAA-14 AVHRR satellite observations. As described in Chapter 4, the results of radiative transfer calculations for the average continental and tropical maritime aerosol models were used with AVHRR observations in a 2-channel, 2-model retrieval scheme to derive aerosol optical depth and an aerosol type mixture fraction. Other investigators have used a similar approach to derive aerosol optical properties from satellite observations, though there are differences in the aerosol size distribution, the index of refraction, and the aerosol model used in the

determination (Durkee et al. 1991, Higurashi and Nakajima 1999, Mischenko et al. 1999). Since accurate retrieval of aerosol optical properties depends critically on the selection of an appropriate size distribution and complex index of refraction, several studies were conducted to examine the sensitivity of the calculations to variations in the size distribution and index of refraction.

Though aerosols have a range in size of more than four orders of magnitude, the volume distribution of tropospheric aerosol has two and often three distinct peaks at particle sizes that correspond to Aitken nuclei (0·01 to 0·1 μm), fine (0·1 to 1 μm), and coarse mode particles (1 to 100 μm) (Whitby et. al. 1972, Charlson 1988).

While some investigators have used the log normal function with as many as seven terms to represent the different species in an aerosol distribution (Harris and McCormick, 1972; Davies, 1974), Whitby and Cantrell (1975) have shown that it is generally adequate to represent the two or three peaks found in a typical volume distribution of tropospheric aerosol, with a sum of two or three log normal distributions. The log normal distribution is frequently used to describe the size distribution of continental and maritime aerosols, where it is desirable to treat the composition of the individual modes separately.

Using Mie theory, the extinction efficiency and extinction cross section can be calculated for each of the components of an aerosol model by treating the components as an external mixture (no interaction between components). Optical depths for the individual components are calculated as follows:

$$\tau_{TOT} = \sum_{i=1}^{n} \tau_i , \tag{3.33}$$

and since

$$\tau = N\sigma L , \tag{3.34}$$

then

$$N\sigma_{TOT} L = \sum_{i=1}^{n} n_i \sigma_i L , \tag{3.35}$$

or

$$N\sigma_{TOT} = \sum_{i=1}^{n} n_i \sigma_i , \tag{3.36}$$

where N is the total number of particles per unit volume, and n is the number of particles for each component of the mixture.

For a 3-component aerosol model, for example, the individual optical depths are calculated as follows:

$$N\sigma_{TOT} = n_1\sigma_1 + n_2\sigma_2 + n_3\sigma_3 , \tag{3.37}$$

or

$$1 = \frac{n_1\sigma_1}{N\sigma_{TOT}} + \frac{n_2\sigma_2}{N\sigma_{TOT}} + \frac{n_3\sigma_3}{N\sigma_{TOT}} , \tag{3.38}$$

and

$$1 = \frac{\tau_1}{\tau_{TOT}} + \frac{\tau_2}{\tau_{TOT}} + \frac{\tau_3}{\tau_{TOT}} , \tag{3.39}$$

so

$$\tau_1 = \tau_{TOT}\frac{n_1\sigma_1}{N\sigma_{TOT}}, \tau_2 = \tau_{TOT}\frac{n_2\sigma_2}{N\sigma_{TOT}}, \tau_3 = \tau_{TOT}\frac{n_3\sigma_3}{N\sigma_{TOT}} . \tag{3.40}$$

Since the values of n and σ are known, the τ values for the individual components can be calculated simply by assigning a value to the mixture optical depth (τ_{TOT}).

Once derived, the optical parameters of the individual components can be mixed to derive the scattering parameters for the multi-component aerosol model. Several aerosol models chosen as representative of average urban and maritime polluted conditions were used in the INDOEX calculations. They are average

continental and tropical maritime, from Hess et al. (1998), and polluted maritime (INDOEX-specific), from Satheesh et al. (1999), and their respective components and physical parameters are given in Table 3.2.

Figure 3.5 shows the phase function for the average continental and tropical maritime mixtures and their individual components at wavelength = 0·65 μm. The mixture and the components show a large forward scatter component (low scattering angles) typical of particles with radii comparable to the wavelength of light, and only the larger non-absorbing particles exhibit a pronounced backscatter component (seen at high scattering angles). To illustrate the relationship between satellite-received radiance and the scatter of light by an aerosol mixture and its individual components, reflectance based on a single scatter approximation is computed using

$$R = \frac{P(\Theta)\omega\tau}{4\mu\mu_0}, \tag{3.41}$$

where:

$P(\Theta)$=phase function as a function of scattering angle

ω=single scattering albedo

τ=optical depth

μ=cosine of the satellite zenith angle

μ_0=cosine of the solar zenith angle.

Figure 3.6 shows AVHRR Channel 1 reflectance as a function of scattering angle for the average continental and tropical maritime mixtures and their components. Scattering by a cloud-free atmosphere approximates single scattering over the range of optical depths from 0 to 1 at the reference wavelength (λ=0.55 μm). The optical depths for the individual components are calculated using (3.40)

Table 3.2. Aerosol model parameters taken from Hess et al. (1998) and Satheesh et al. (1999). Parameters are shown for Average Continental, Tropical Ocean, and Polluted Maritime, with Water Soluble 80% RH (WASO80), Insoluble (INSO), Soot, Sea Salt Accumulation Mode 80% RH (SSAM80), Sea Salt Coarse Mode 80% RH (SSCM80), and Mineral Transport (MITR) constituents.

MODEL	N	R_{min}	R_{max}	R_{mod}	σ	λ=0.65 μm		λ=0.80 μm	
		μm				m_r	m_i	m_r	m_i
Average Continental									
▫ **WASO80**	0·458	0·007	29·8	0·031	2·24	1·397	0·002	1·393	0·003
▫ **INSO**	2.61×10^{-5}	0.005	20	0·471	2·51	1·53	0·008	1·52	0·008
▫ **SOOT**	0.542	0.005	20	0·012	2	1·75	0·435	1·75	0·430
Tropical Ocean									
▫ **WASO80**	0·983	0·007	29·8	0·031	2·24	1·397	0·002	1·393	0·003
▫ **SSAM80**	0.017	0.009	39·9	0·416	2·03	1·351	0	1·348	0

Table 3.2 (continued)

MODEL	N	R_{min}	R_{max}	R_{mod}	σ	λ=0.65 μm		λ=0.80 μm	
		μm				m_r	m_i	m_r	m_i
Polluted Maritime									
▫ **WASO80**	0.202	0.007	29·8	0·031	2·24	1·397	0·002	1·393	0·003
▫ **SSAM80**	1.20×10^{-4}	0.009	39·9	0·416	2·03	1·351	0	1·348	0
▫ **SSCM80**	1.11×10^{-6}	0.009	100	3·49	2·03	1·351	0	1·348	0
▫ **MITR**	1.83×10^{-5}	0.02	5	0·5	2·2	1·53	0·004	1·53	0·004
▫ **SOOT**	0.798	0.005	20	0·012	2	1·75	0·435	1·75	0·430

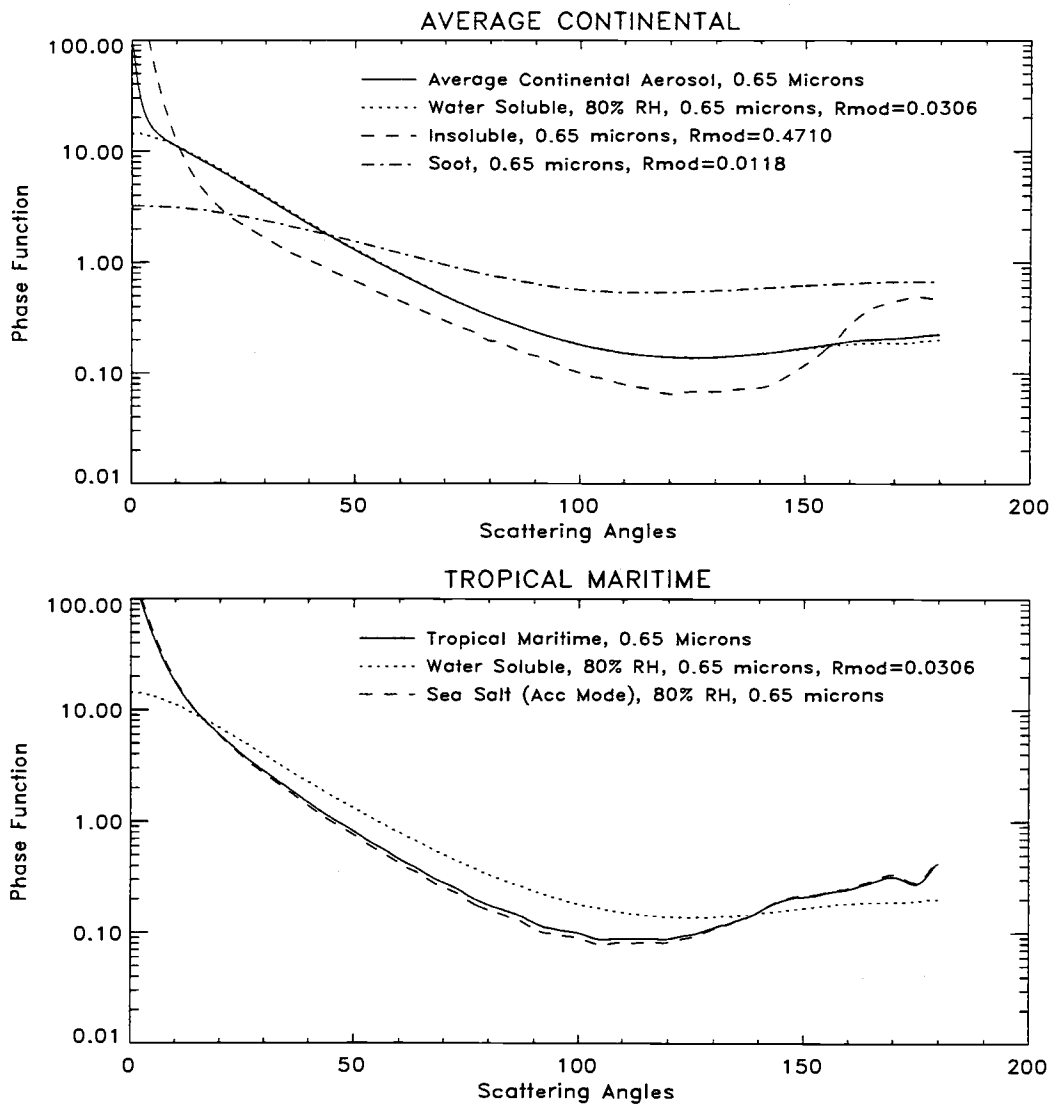

Figure 3.5. Phase function for average continental and tropical maritime mixtures and their components. The phase functions are computed for Channel 1 AVHRR (λ=0·65 μm).

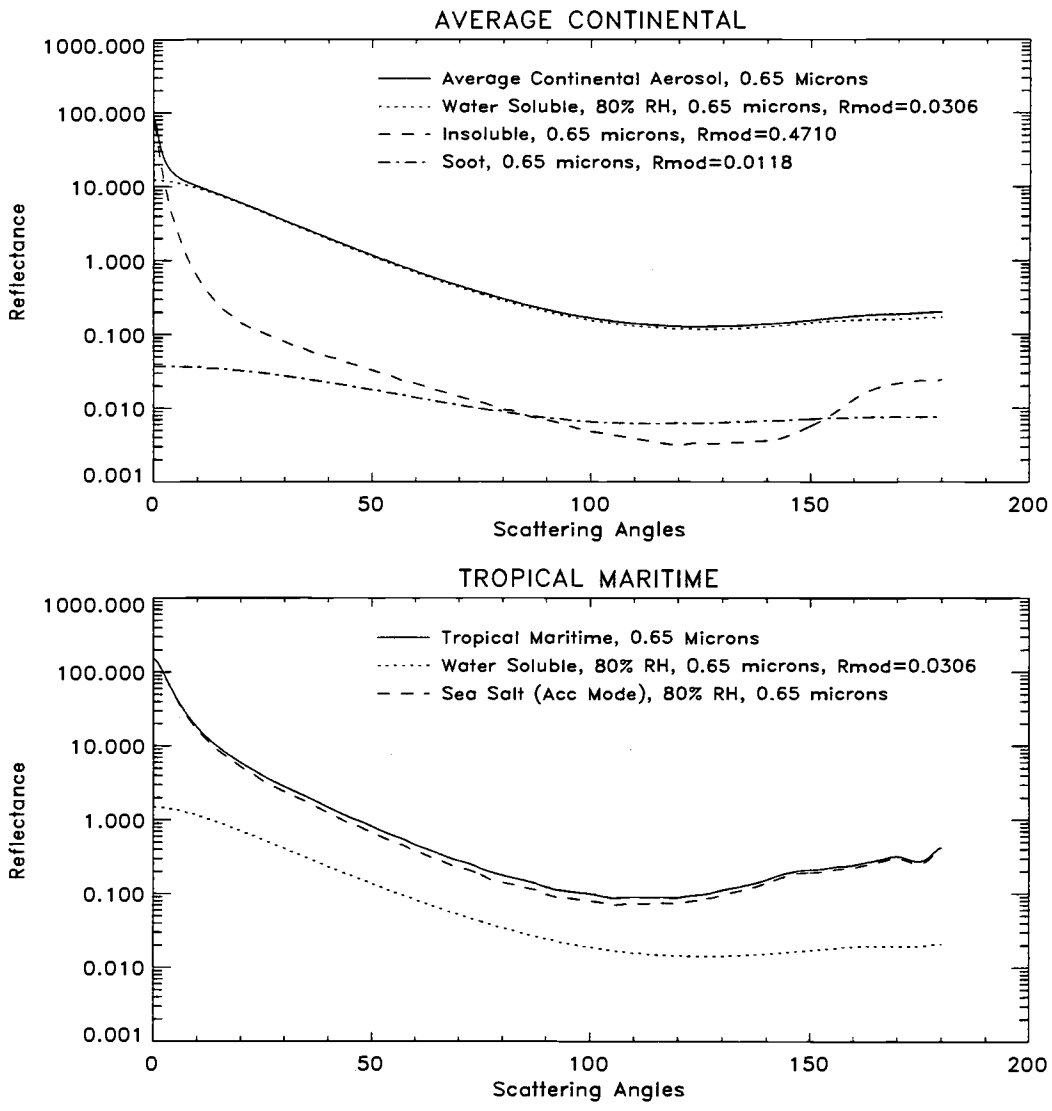

Figure 3.6. AVHRR Channel 1 reflectance as a function of scattering angle for average continental and tropical maritime mixtures and their components.

by arbitrarily setting $\tau_{TOT} = 1$. The water soluble component of the average continental mixture makes the largest contribution to radiance. Additional studies were conducted to examine the scattering behavior of aerosol particles over a wide range of absorber amounts and particle size. Calculations of scattering cross section and phase function were made for particles ranging in size from 0·007 to 39·9 μm, which more than spans the normal mode radius of 0·0306 μm for water soluble particles and 0·4160 μm for sea salt particles. Figures 3.7 and 3.8 show the ratio of Channel 1 (λ=0·65 μm) scattering cross section times phase function to Channel 2 (λ=0·80 μm) of AVHRR, as a function of scattering angle, for water soluble and sea salt particles over a range of particle sizes. Larger particles exhibit erratic scatter behavior at scattering angles greater than 80°, with characteristic back scatter components at high scattering angles. Figure 3.9 shows the ratio of scattering cross section times phase function for Channels 1 and 2 of AVHRR, as a function of scattering angle, for water soluble particles over a range of absorber amounts. For these calculations, the imaginary part of the complex index of refraction ranges from 0·0023, the normal value for m_i for water soluble particles and λ=0·63 μm, to 0·05, an absorber amount typical of highly absorbing particles such as soot. As the absorber amount increases, the single scatter albedo decreases (single scatter albedo is the ratio of scatter efficiency to scatter plus absorption efficiency), and the scatter power diminishes at all scattering angles. Back scatter effects disappear at high scattering angles with 20 times the normal absorber amount and a single scatter albedo below 0·75.

Based on the sensitivity studies presented in this section, it is reasonable to expect similar results from the various retrieval schemes used to derive aerosol optical properties from satellite observations. Phase functions for the four size distributions shown in Fig. 3.2 are similar over the range of scattering angles derived from the satellite observations in the INDOEX region for the 1996-2000 winter monsoon season (scattering angle ranges from 135 to 170°). Phase functions and reflectance for the average continental and tropical marine mixtures

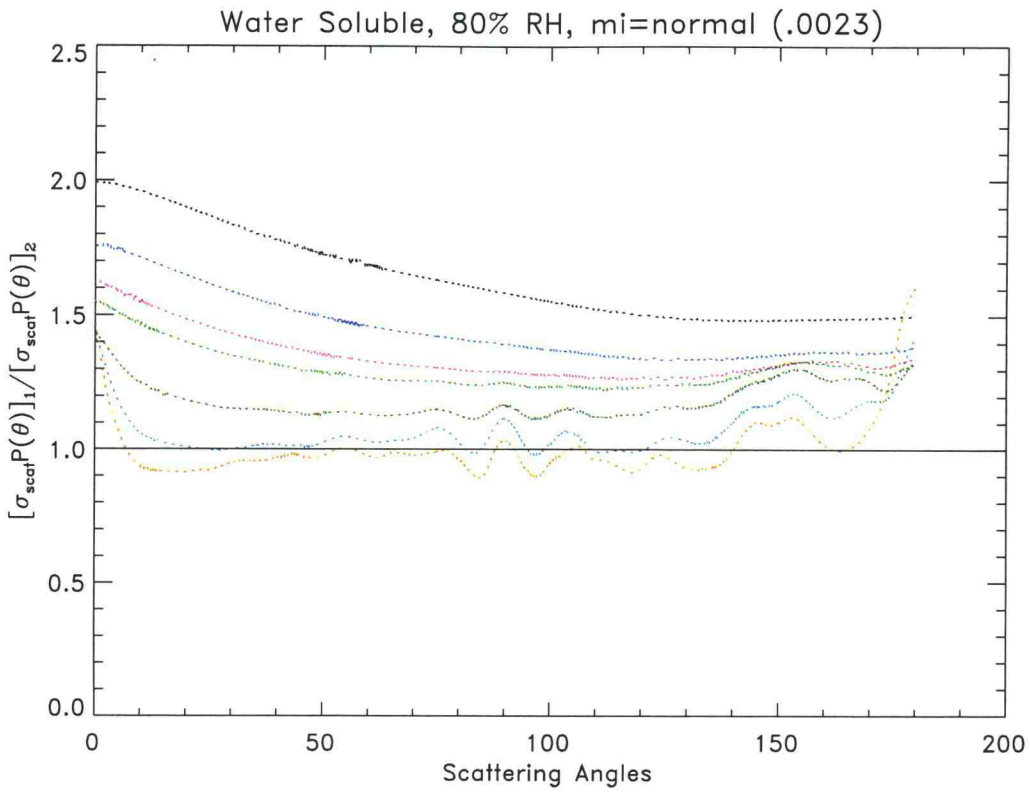

R_{mod} =	0.0100	0.0200	0.0306	0.0400	0.0800	0.1600	0.3200
$[\sigma_{ext}]_1/[\sigma_{ext}]_2$ =	1.6711	1.5221	1.4051	1.3429	1.1803	1.0474	0.9868
$[\sigma_{scat}]_1/[\sigma_{scat}]_2$ =	1.7355	1.5457	1.4200	1.3548	1.1884	1.0542	0.9944
R_{eff} =	0.0516	0.1015	0.1552	0.2029	0.4058	0.8115	1.6220
ω_1 =	0.9579	0.9772	0.9810	0.9819	0.9796	0.9690	0.9439
ω_2 =	0.9224	0.9623	0.9708	0.9732	0.9730	0.9628	0.9368

Figure 3.7. Ratio of Channel 1 (λ=0·65 μm) scattering cross section times the phase function to Channel 2 (λ=0·80 μm) of AVHRR, for water soluble particles over a range of particle sizes. Derived and plotted parameters are shown for a range of mode radii that vary from small (Rmod=0·01, black) to large (Rmod=0·32, red) particles.

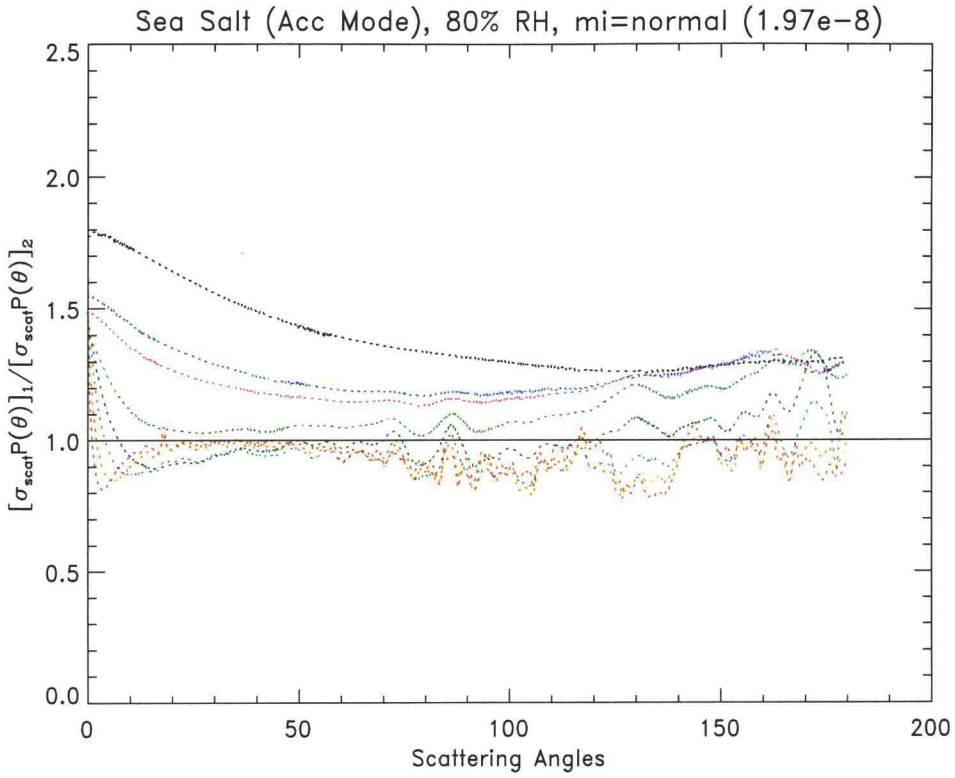

R_{mod} =	0.0400	0.0800	0.1000	0.2000	0.4160	0.8000	1.6000	3.2000
$[\sigma_{ext}]_1/[\sigma_{ext}]_2$ =	1.5215	1.3152	1.2542	1.0852	0.9872	0.9699	0.9857	0.9892
$[\sigma_{scat}]_1/[\sigma_{scat}]_2$ =	1.5215	1.3152	1.2542	1.0852	0.9872	0.9699	0.9857	0.9892
R_{eff} =	0.1407	0.2813	0.3516	0.7032	1.4627	2.8121	5.5860	10.5644
ω_1 =	1.0000	1.0000	1.0000	1.0000	1.0000	1.0000	1.0000	1.0000
ω_2 =	1.0000	1.0000	1.0000	1.0000	1.0000	1.0000	1.0000	0.9999

Figure 3.8. Ratio of Channel 1 (λ=0·65 μm) scattering cross section times the phase function to Channel 2 (λ=0·80 μm) of AVHRR, for sea salt particles over a range of particle sizes. Derived and plotted parameters are shown for a range of mode radii that vary from small (Rmod=0·04, black) to large (Rmod=3.2, red) particles.

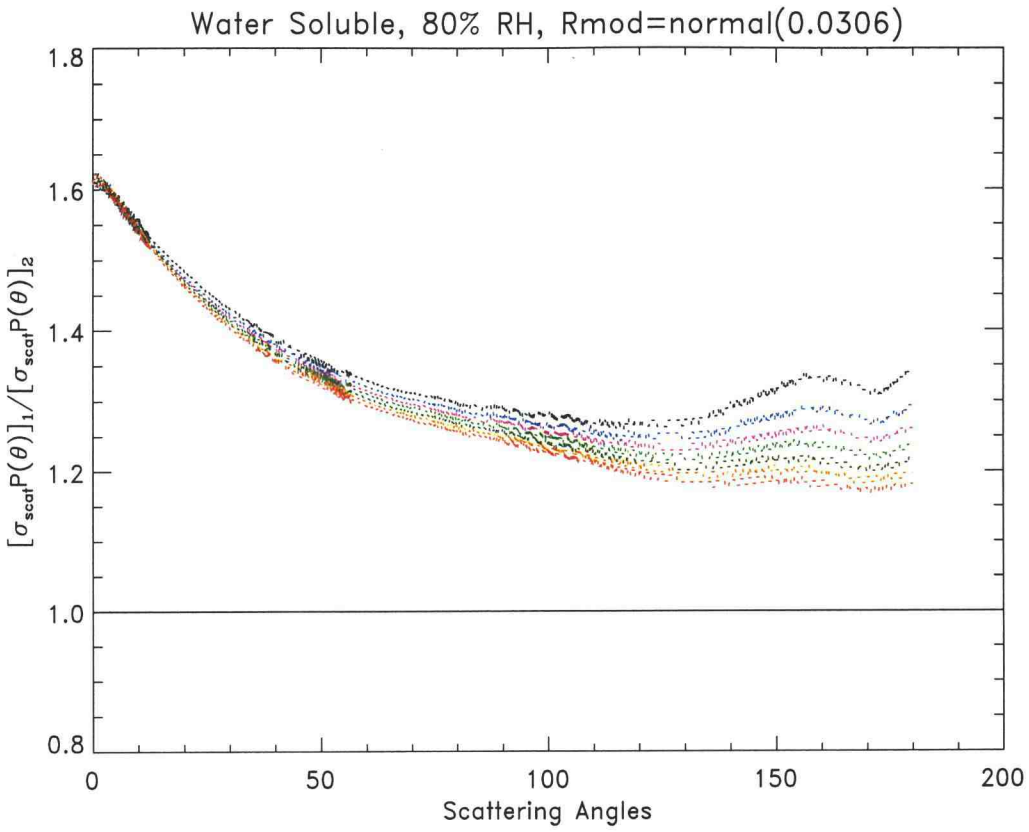

m_i =	0.0023	0.0100	0.0180	0.0260	0.0340	0.0420	0.0500
$[\sigma_{ext}]_1/[\sigma_{ext}]_2$ =	1.4051	1.4011	1.3882	1.3767	1.3651	1.3547	1.3443
$[\sigma_{scat}]_1/[\sigma_{scat}]_2$ =	1.4200	1.4113	1.4064	1.4025	1.3980	1.3944	1.3902
ω_1 =	0.9810	0.9233	0.8695	0.8215	0.7783	0.7393	0.7039
ω_2 =	0.9708	0.9165	0.8583	0.8064	0.7600	0.7183	0.6807

Figure 3.9. Ratio of Channel 1 (λ=0·65 μm) scattering cross section times the phase function to Channel 2 (λ=0·80 μm) of AVHRR, as a function of scattering angle, for water soluble particles over a range of absorber amounts. Derived and plotted parameters are shown for a range of m_i, the imaginary part of the complex index of refraction, which varies from low absorption values typical of water soluble particles (m_i=0·0023, black) to high absorption values typical of soot particles (m_i=0·05, red).

and their individual components are also similar over the range of scattering angles from INDOEX (Figs. 3.5 and 3.6). Figs. 3.7 and 3.8 show systematic differences in `scattering cross section ratios for both aerosol models across a range of particle sizes spanning two orders of magnitude. Increased absorber amount has little effect on the scattering cross section ratios in the range of INDOEX scattering angles (Fig. 3.9). Hence, sensitivity studies conducted to examine the critical determinants for retrieving optical properties from satellite observations show that, aside from some sensitivity to particle size, there is no indication that one size distribution or aerosol model will be superior to another.

Since size is a dominant effect, and absorption cannot be ignored, variations in aerosol type and optical depth over a region and from region to region will be accounted for in the 2-model retrieval scheme used in this study by using a mixture of average continental particles with relatively small particles that absorb, and larger essentially non-absorbing marine particles.

Chapter 4
The Retrieval of Aerosol Optical Depth and Radiative Forcing: Theory

4.1 Introduction

A primary objective of INDOEX was the determination of the aerosol radiative forcing for the Indian Ocean during the January-March winter monsoon. Estimates of aerosol burdens and the consequent radiative forcing derived from satellite imagery data were the primary means for achieving this objective, and the Advanced Very High Resolution Radiometer (AVHRR) on the NOAA-14 satellite was a major source of observations. Several schemes have been devised for retrieving aerosol properties from AVHRR observations (Durkee et al. 1991; Stowe et al. 1997; Higurashi and Nakajima 1999; Mischenko et al. 1999; Rajeev et al. 2000). The schemes are identical in that aerosol properties are derived from the departures of the observed visible and near infrared reflectances from those expected for cloud-free and aerosol-free ocean scenes. The reflectances against which the observations are compared are obtained through radiative transfer calculations for a prescribed set of aerosol models. The schemes differ in the methods used to identify cloud-free ocean scenes suitable for the retrieval of aerosol properties and in the aerosol models used to calculate the radiances expected for a cloud-free ocean. Here, the sensitivity of the retrieved aerosol properties and the resulting estimates of the aerosol direct radiative forcing to the aerosol models used in the retrieval schemes are explored.

Aerosol properties were derived from the NOAA-14 AVHRR observations using the results of radiative transfer calculations for the following aerosol models: 1) the tropical marine and average continental aerosols described by Hess et al.

(1998); 2) the model derived from aerosol composition and particle sizes deduced from data collected at the Kaashidhoo Climate Observatory (KCO) and used by Rajeev et al. (2000) to derive aerosol burdens and estimate the radiative forcing for the INDOEX region (Ramanathan et al. 2000); this model will be referred to as the First Field Phase (FFP) model, and 3) the models used in the NOAA Phase 1 and Phase 2 operational algorithms (Stowe et al. 1997). In the case of the tropical marine and average continental aerosols, a new retrieval scheme was developed in which reflectances at visible (0.64-μm AVHRR Channel 1) and near infrared (0.84-μm AVHRR Channel 2) wavelengths were used to derive: 1) the fraction of the two aerosol components contributing to a mixed aerosol, and 2) the resulting optical depth of the mixture. This scheme is similar to that suggested by Wang and Gordon (1994) for retrievals that employ multi-angle and multispectral observations, like MISR, and also by Kahn et al. (2000). These schemes offer a plausible link between aerosol size and optical properties by mixing aerosol types with distinctive sizes and optical properties. This type of retrieval is an alternative to those in which the index of refraction is held fixed, but particle size is adjusted based on the wavelength dependence of the retrieved optical depths (Durkee et al. 1991; Higurashi and Nakajima 1999; Mischenko et al. 1999).

Optical depths retrieved for the different aerosol models were compared with simultaneous surface-based measurements obtained with various radiometers deployed for INDOEX. The comparisons covered the winter monsoons for 1996-2000.

The retrieved optical depths along with the corresponding aerosol models were used in broadband radiative transfer calculations of the top of the atmosphere and surface aerosol direct radiative forcing under cloud-free conditions. Estimates of the top of the atmosphere forcing were found to be relatively insensitive to the choice of the aerosol model used to retrieve the aerosol properties. That is, as long as the estimate of the top of the atmosphere radiative forcing is derived based on the same aerosol model used to retrieve the aerosol properties, the radiative forcing will not be greatly affected by the choice of the aerosol model. On the other hand,

because the different models produce different amounts of absorption in the atmosphere, the radiative forcing at the surface (and that of the atmosphere) is, of course, sensitive to the aerosol model.

While the procedures for estimating the aerosol direct radiative forcing for cloud-free conditions are straightforward, those for determining the forcing under cloudy conditions require simultaneous measurements of the cloud properties. The forcing depends not only on the properties of the aerosol but also on the properties of the clouds and the vertical distribution of both the aerosol and the clouds (Haywood et al. 1997; Ramanathan et al., 2000). As part of this study, individual AVHRR fields of view were identified as either cloud-free, or overcast by optically thick clouds from a single-layered cloud system. The fields of view that were neither cloud-free nor overcast by optically thick, layered clouds were taken to be partly cloud covered. For the clouds encountered during INDOEX, few layered cloud systems met the criteria required for overcast fields of view (< 5%), even at the full, 1-km resolution of the AVHRR. In addition, because the criteria used to identify overcast fields of view were limited to identifying optically thick, layered cloud systems, fields of view overcast by thin cirrus, or overcast by clouds distributed in altitude, were potentially identified as being partly cloudy. As with other methods for determining cloud properties, the derived properties are a function of the procedures used to identify cloudy scenes and to extract the properties for the cloudy scenes. Results for different approaches to determining cloud properties diverge most for scenes in which the cloud elements cannot be resolved by the observing radiometer (Wielicki and Parker, 1992), as was common in INDOEX. Because of the range of possible cloud properties, sensitivity studies were performed in which different assumptions concerning the effects of clouds on the aerosol direct radiative forcing were employed to determine the range of the resulting aerosol direct radiative forcing at the top of the atmosphere and the surface.

4.2 Retrieval of Aerosol Properties

In order to retrieve aerosol properties, reflected sunlight measured with the AVHRR must be compared with that obtained with a radiative transfer model. Such comparisons require that the AVHRR observations of reflected sunlight be calibrated. Because there is no on-board calibration source for AVHRR Channels 1 and 2, the extensive ice sheets of Greenland and Antarctica were used to calibrate the observations (Loeb, 1997; Tahnk and Coakley, 2000a and b). The reflectances of the cloud-free fields of view were compared with those calculated assuming that the aerosol had a given set of properties. The aerosol optical depth, and possibly an index for particle size or aerosol type was selected to give the best agreement between observed and calculated reflectances. The selected optical depth and properties were then taken to be the retrieved values. In this section, the method used to identify cloud-free fields of view is briefly described. The aerosol models along with the radiative transfer model used to calculate the reflectances are also described. Finally, the procedures used to extract aerosol properties from the comparison of observed and calculated reflectances are described.

4.2.1 Scene Identification

Spatial coherence techniques are used with calibrated AVHRR observations in scene identification. Fields of view were identified as cloud-free if they exhibited locally uniform reflected sunlight and thermal emission on scales of ~ 8 km (2 × 2 pixel arrays) for the 4-km AVHRR Global Area Coverage (GAC) observations. For cloud-free ocean scenes, the standard deviation of the 0.64-μm (AVHRR

Channel 1) reflectance for localized arrays of pixels had to be less than 0.004. The standard deviation of the 11-μm (AVHRR Channel 4) emission had to be less than 0.5 mWm^{-2} sr^{-1} cm, equivalent to ~ 0.3 K for the brightness temperatures associated with the cloud-free oceans. Away from regions of sun glint, cloud-free ocean scenes were required to have a ratio of the near infrared (0.84 μm, AVHRR Channel 2) reflectance to visible (0.64 μm, AVHRR Channel 1) reflectance that was less than 0.85. Overcast pixels produce values of near unity for this ratio while pixels with vegetated land produce values > 1. Here, sunlight was taken to be outside of the sun glint region if the light was reflected at angles greater than 30° from the direction of specular reflection for a flat surface. The distribution of radiances for pixels that exhibited locally uniform reflection and emission and which also had low near infrared to visible reflectance ratios and lay within a ~ 250-km scale region were used to establish thresholds for visible reflectances and 11-μm emission suitable for the cloud-free ocean pixels within the region. Of the radiances for these pixels, the 95th percentile of the visible reflectance was taken as an upper limit and the 5th percentile of the 11-μm emission was taken as a lower limit for cloud-free pixels. These thresholds were applied to all fields of view that exhibited locally uniform emission and reflection and which had low near infrared to visible reflectance ratios and lay within a 150-km scale subregion centered within the larger ~ 250-km scale region. Likewise, fields of view were identified as overcast by a single-layered cloud system if they exhibited locally uniform emission at 11 μm. For overcast pixels, the standard deviation of the 11-μm radiance for the pixel arrays had to be less than 0.5 mWm^{-2} sr^{-1} cm, which for low-level clouds is equivalent to a standard deviation of 0.4 K in brightness temperatures. Pixels that exhibited neither locally uniform reflectances nor locally uniform emitted radiances were presumed to be partly cloud covered. The 50th percentile of the reflectances for the partly cloudy pixels was used as a minimum reflectance for pixels to be identified as overcast by optically thick clouds. This visible threshold was applied to the fields of view exhibiting locally uniform

emission that were not cloud-free in order to identify fields of view that were overcast by optically thick layered cloud systems. This procedure was repeated region by region and subregion by subregion until all fields of view within the overpass were identified. The regions and subregions were overlapped to ensure that all pixels were identified.

The goal in the design of the identification scheme was to identify ensembles of pixels that were representative of cloud-free pixels and pixels overcast by optically thick, layered clouds within the ~ 150 km region being studied. The scheme does not identify all cloud-free fields of view, nor does it identify all overcast fields of view within the region. In particular, cloudy fields of view overcast by a system of clouds residing in multiple cloud layers along with fields of view overcast by thin cirrus are identified as being partly cloud covered. For cloud-free fields of view, the identification scheme specifically avoids individual fields of view that may be surrounded by cloud and are thus likely to be cloud contaminated in favor of fields of views that are contiguous with all pixels exhibiting properties that are typical of cloud-free scenes. As discussed in Tahnk and Coakley (2000), about 15% of the 4-km AVHRR GAC fields of view were typically identified as being cloud-free for the Indian Ocean in the Northern Hemisphere. Thus, fields of view suitable for aerosol retrievals were plentiful. The majority of the 4-km fields of view were found to be partly cloudy. Relatively few (< 5%) were identified as being overcast by single-layered optically thick clouds and of these, a sizable fraction were associated with upper-level systems. By relaxing the criteria used to identify cloud-free fields of view, so that the identified fields of view were subjected to successively greater levels of cloud contamination, cloud contamination was found to contribute less than 0.05 to the retrieved 0.55-μm optical depth. Here, 0.55-μm is used as the reference wavelength for reporting optical depths. This level of cloud contamination is less than half of the average optical depths found for pristine ocean regions of the Southern Hemisphere.

4.2.2 Aerosol and Radiative Transfer Models

Table 4.1 lists characteristics of the aerosol models used in the retrievals. The properties are given for a relative humidity of 70%. As mentioned in the introduction, the average continental and tropical marine aerosol models were taken from Hess et al. (1998). These models, along with the FFP model, are multi-component models. For comparison, retrievals were also performed with the models used in the NOAA Phase 1 and Phase 2 retrieval algorithms (Stowe et al. 1997); these are single-component models.

Aerosol properties were retrieved by matching observed reflectances for the cloud-free fields of view to those computed for a particular aerosol. The reflectances were calculated using DISORT (Stamnes et al. 1988). Absorption by O_3, O_2, and H_2O within the AVHRR Channel 1 and 2 passbands was treated using the correlated *k*-distributions described by Kratz (1995). The McClatchey et al. (1972) tropical climatological profiles of temperature and humidity were used to calculate the reflectances. As discussed in Section 4.4, using midlatitude summer climatological profiles in place of the tropical profiles had little effect on the retrieved optical depths. As discussed by Rajeev et al. (2000), the aerosols were uniformly mixed below 1 km and distributed with a scale height of 0.8 km between 1 and 8 km. No aerosol was placed above 8 km. The vertical distribution is consistent with that derived from lidar returns in the INDOEX region as reported by Satheesh et al. (1999). In addition, as did Rajeev et al. (2000), optical properties of the aerosols were calculated using a relative humidity of 78% for 0–1 km, 62% for 1–2 km, and 35% above 2 km.

Reflectances were calculated for aerosol optical depths at a standard wavelength of 0.55 μm. The optical depths ranged from 0 – 0.9 in steps of 0.1; the solar zenith angle ranged from 0° – 85° in steps of 5°; the cosine of the view zenith angle

Table 4.1. Properties of Aerosol Models Used in Retrievals

Component	Number Fraction	Effective Radius (μm)	0.55-μm Extinction Efficiency	0.65-μm Extinction Efficiency	Single-scattering albedo	Asymmetry Parameter	0.80-μm Extinction Efficiency	Single-scattering albedo	Asymmetry Parameter
Average Continental									
Water Soluble	0.458	0.145	0.842	0.656	0.977	0.675	0.463	0.964	0.653
Insoluble	2.61×10^{-5}	3.60	2.26	2.30	0.750	0.811	2.34	0.776	0.794
Soot	0.542	0.039	0.481	0.380	0.173	0.302	0.284	0.133	0.263
Composite	*1.0*	*0.205*	*0.825*	*0.655*	*0.899*	*0.678*	*0.638*	*0.903*	*0.682*
Tropical Marine									
Water Soluble	0.983	0.145	0.842	0.656	0.977	0.675	0.463	0.964	0.653
Sea Salt (Acc. Mode)	0.017	1.324	2.56	2.62	1.000	0.781	2.64	1.000	0.785
Sea Salt (Coarse Mode)	2.17×10^{-6}	10.860	2.11	2.12	1.000	0.848	2.13	1.000	0.844
Composite	*1.0*	*1.011*	*2.01*	*2.00*	*0.998*	*0.771*	*2.01*	*0.997*	*0.774*

Table 4.1 (Continued). Properties of Aerosol Models Used in Retrievals

Component	Number Fraction	Effective Radius (μm)	0.55-μm Extinction Efficiency	0.65-μm Extinction Efficiency	Single-scattering albedo	Asymmetry Parameter	0.80-μm Extinction Efficiency	Single-scattering albedo	Asymmetry Parameter
FFP									
Water Soluble	0.202	0.145	0.842	0.656	0.977	0.675	0.463	0.964	0.653
Sea Salt (Acc. Mode)	1.20×10^{-4}	1.324	2.56	2.62	1.000	0.781	2.64	1.000	0.785
Sea Salt (Coarse Mode)	1.11×10^{-6}	10.860	2.11	2.12	1.000	0.848	2.13	1.000	0.844
Mineral (Transport)	1.83×10^{-5}	1.843	2.36	2.41	0.877	0.851	2.47	0.906	0.733
Soot	0.798	0.039	0.481	0.380	0.173	0.302	0.284	0.133	0.263
Composite	*1.0*	*0.500*	*0.863*	*0.725*	*0.847*	*0.704*	*0.694*	*0.867*	*0.711*
NOAA Phase 2									
–	1.0	0.349	2.17	1.92	1.000	0.744	1.58	1.000	0.732
NOAA Phase 1									
–	1.0	0.085	0.315	0.246	1.000	0.595	0.180	1.000	0.595

ranged from 0.3 – 1.0 in steps of 0.1, and the relative azimuth angle ranged from 0° – 180° in steps of 10°. The ocean surface was taken to be Lambertian with an albedo of 0.005 at both wavelengths and for all retrieval schemes. This albedo was chosen so as to minimize the RMS differences between retrieved optical depths and those measured at the surface for both visible and near infrared wavelengths. When comparing with observed reflectances, the calculated reflectances were linearly interpolated to the desired sun-earth-satellite geometry.

4.2.3 Aerosol Retrieval Schemes

Three types of retrievals were used. In the simplest scheme, reflectances were calculated for a single aerosol model and then optical depths were retrieved by seeking agreement between calculated and observed reflectances at one wavelength, for example, the 0.64-μm Channel 1 of AVHRR (Stowe et al., 1997; Rajeev et al. 2000).

In the second, the new scheme developed for this study, two aerosol models were used and reflectances were calculated for the visible and near infrared wavelength channels of the AVHRR. The retrieved optical depth and the fraction of each aerosol type contributing to the retrieved optical depth were selected so that the observed visible and near infrared reflectances agreed with the calculated values as illustrated in Figure 4.1. The reflectances at the two wavelengths were calculated for the sun-earth-satellite viewing geometry associated with the observation. Aerosol properties at 0.65 μm were used in calculations of the reflectances for AVHRR Channel 1 at 0.64 μm, and properties at 0.80 μm were used in calculations of the reflectances for AVHRR Channel 2 at 0.84 μm.

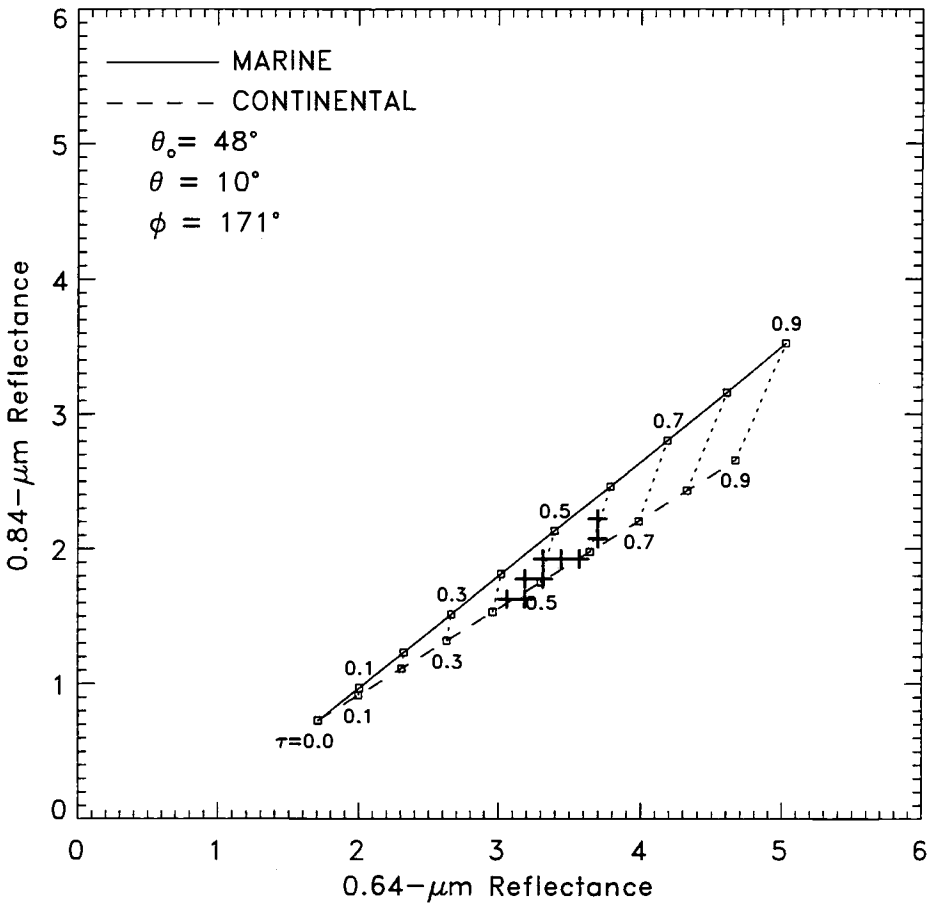

Figure 4.1. Calculated and observed 0.64 and 0.84-μm reflectances for ~100 km region of the Arabian Sea. Average values are given for the solar zenith, θ_0, satellite zenith, θ, and relative azimuth angles, ϕ of the observations, expressed in degrees. Observations (+) are from NOAA-14 AVHRR for a pass during the INDOEX Intensive Field Phase, February 1999. Reflectances are given for the average continental (dashed line) and tropical marine (solid line) aerosol models of Hess et al. (1998). Dotted lines are lines of constant 0.55-μm optical depth for mixtures of the average continental and tropical marine aerosol.

Fig. 4.1 shows the cloud-free reflectances for the individual models, the tropical marine aerosol (solid line) and the average continental aerosol (dashed line). Dotted lines joining the lines associated with the individual models are lines of constant optical depths for various aerosol mixtures. The dependence of the reflectances on optical depth shown in Fig. 4.1 suggests that a natural rendition of the reflectances would be as a mixture of the reflectances contributed by each component. The combined reflectance would then be given by

$$r_i(\tau) = f r_{iC}(\tau) + (1-f) r_{iM}(\tau), \tag{4.1}$$

where $r_i(\tau)$ is the cloud-free ocean reflectance in AVHRR channel i = 1, 2 when the optical depth of the mixed aerosol is τ at the standard wavelength; $r_{iC}(\tau)$ is the channel i reflectance for the cloud-free ocean over which an average continental aerosol has optical depth τ at the standard wavelength; $r_{iM}(\tau)$ is the corresponding reflectance for the tropical marine aerosol; f is the fraction of the mixture that is taken to be the average continental aerosol, and $1-f$ is the fraction of the mixture that is taken to be the tropical marine aerosol. As defined, f plays the role of a mixing fraction as commonly used to describe the thermodynamic properties of air parcels that undergo mixing. In this case, for f = 1, the aerosol is the average continental aerosol; for f = 0, the aerosol is the tropical marine aerosol. Because the slopes of the Channel 2 to Channel 1 reflectances are numerically rather similar for the average continental and the tropical marine aerosols, which, of course, is unfortunate for the design of a retrieval scheme, the slope of the Channel 2 to Channel 1 reflectances is approximately given by

$$\frac{r_1(\tau)-r_{10}}{r_2(\tau)-r_{20}} \cong f\left(\frac{r_{1C}(\tau)-r_{10}}{r_{2C}(\tau)-r_{20}}\right)+(1-f)\left(\frac{r_{1M}(\tau)-r_{10}}{r_{2M}(\tau)-r_{20}}\right), \tag{4.2}$$

where r_{i0} is the ocean reflectance under cloud-free and aerosol-free conditions for channel i. In addition, since the reflectances are almost linear functions of the optical depth, as indicated by the lines associated with the separate aerosol models in Fig. 4.1, (4.2) is approximately equivalent to

$$\frac{r_1(\tau)-r_{10}}{r_2(\tau)-r_{20}} \cong f\left(\frac{r_{1C}(\tau_0)-r_{10}}{r_{2C}(\tau_0)-r_{20}}\right)+(1-f)\left(\frac{r_{1M}(\tau_0)-r_{10}}{r_{2M}(\tau_0)-r_{20}}\right), \tag{4.3}$$

with τ_0 a reference optical depth at the standard wavelength. Here $\tau_0 = 0.9$. For each cloud-free pixel, f is derived from (4.3). Discrepancies between values of the slopes calculated using (4.1) separately for Channels 1 and 2 and those obtained using (4.3) are, of course, zero for $f = 0$ and $f = 1$. They reach maxima for $f = 0.5$, but the discrepancies never exceed 5% of the slope for the range of viewing geometries and optical depths considered. Thus, the aerosol mixing fraction, f, is derived from the slope of the Channel 1 to Channel 2 reflectance departures from the values expected for cloud-free and aerosol-free conditions. Once f is determined, the optical depth at the standard wavelength is derived from the reflectances themselves, as given by (4.1).

To illustrate the relationship between f, τ and the reflectances, the crosses (+) in Fig. 4.1 represent the reflectances from the NOAA-14 AVHRR for the cloud-free pixels found within a 100-km scale portion of the Arabian Sea during

INDOEX. Each point is now interpreted as being due to a specific mixture of the two aerosols and the mixture produces a specific optical depth at the standard wavelength, as indicated in the figure.

The average continental and tropical marine aerosol models, described by Hess et al. (1998), were chosen for this retrieval scheme with the following considerations. First, the aerosol over the Indian Ocean was expected to be a mixture of a continental haze with absorbing aerosols, as is the case for the average continental model. Second, the aerosol was also expected to have a prominent marine component, particularly when levels of pollution from the continent were low. Third, the average continental and tropical marine aerosols, for most viewing geometries, spanned the largest portion of the two-channel reflectance domain like that shown in Fig. 4.1. In other words, the slopes of the curves in Fig. 4.1 for the two-channel reflectances produced individually by the two aerosol models have the largest separation when the two models are the tropical marine and average continental aerosols. The slopes of the curves are governed primarily by the size of the particles responsible for scattering. In the case of the tropical marine aerosol, the particle sizes are relatively large, effective radius ~ 1.0 μm (Table 4.1), and for the average continental aerosol the particle sizes are relatively small, effective radius ~ 0.2 μm. Increasing the amount of sunlight absorbed by these aerosols by adding soot as an additional component to each has little effect on the slopes of the reflectance curves. The additional absorption simply diminishes the reflectances produced by a given optical depth thereby leading to higher retrieved optical depths for a given set of reflectances.

For simplicity, the retrieval scheme just described will be referred to as the 2-channel, 2-model scheme. To complete this retrieval scheme, rules were prescribed for dealing with reflectances that lay outside the domain bracketed by the reflectances associated with mixtures of the two aerosol models. For reflectances outside the bracketed domain, the retrieved aerosol type was set to the model which had reflectances nearest those observed, either the average continental or the tropical marine aerosol model, and the optical depth was taken to be that which

produced the smallest RMS differences between the observed and calculated reflectances for both channels. Because it uses reflectances at two wavelengths in a least squares solution, this procedure differs from that typically employed in single-channel, single aerosol model retrieval schemes. This 2-channel, single-model scheme is the third retrieval scheme considered here. Differences between the results obtained with the different retrieval schemes are explored in Sections 4.4 and 4.5.

The single scattering approximation is useful for illustrating how reflectivities are partitioned between scattering and absorption for the two aerosol models. In the single scattering approximation, for an optically thin atmosphere, the reflectance reaching a satellite sensor due to molecular and aerosol scattering above a dark background is given by

$$R(\theta,\theta_0,\phi)=\frac{\omega_0\tau_0 P_0(\theta,\theta_0,\phi)}{4\mu}, \tag{4.4}$$

where

θ = view zenith angle

θ_0 = solar zenith angle

ϕ = azimuth of scattered radiation relative to the solar beam

μ = cosine(θ)

$\tau_0 = \tau_a + \tau_r$ (τ_a, τ_r = aerosol and Rayleigh optical depths)

$\omega_0 = \frac{\omega_a\tau_a + \omega_r\tau_r}{\tau_0}$ (ω_a, ω_r = aerosol and Rayleigh single scattering albedos)

and

$$P_0(\theta,\theta_0,\phi)=\frac{P_a\omega_a\tau_a+P_r\omega_r\tau_r}{\omega_0\tau_0}$$ (P_a, P_r = aerosol and Rayleigh phase functions).

The background is assumed to be a Lambertian ocean surface with an albedo of 0.005. Figure 4.2 shows the single scattering approximation for the aerosol models and viewing geometry used in Fig. 4.1. The observations which fell within the lines representing the average continental and tropical models using reflectances generated by DISORT (Fig. 4.1), fall outside the lines when the single scattering approximation is used to generate the reflectances (Fig. 4.2a). If the two models are adjusted by a factor derived by comparing reflectances at an optical depth of 0.9 from Figs. 4.1 and 4.2a, the observations from Fig. 4.1 fall within the lines representing the 2 models in the single scattering approximation (Fig. 4.2b). The adjustment factors (0.87 for 0.64-μm reflectance, and 0.70 for 0.84-μm reflectance) represent the effect of gaseous absorption (O_3 and O_2 in Channel 1, and H_2O in Channel 2) on satellite-received radiances.

Figs. 4.2a and 4.2b show distinctly different scattering characteristics for the two models. At all non-zero values of optical depth, reflectivities for the average continental model are lower than for the tropical model due to the presence of absorbing aerosols.

4.3 Radiative Forcing

Once the mixing fraction and optical depth of the aerosol mixture was obtained, the diurnally averaged broadband, 0.2 – 4.0-μm, net radiative flux at the top of the

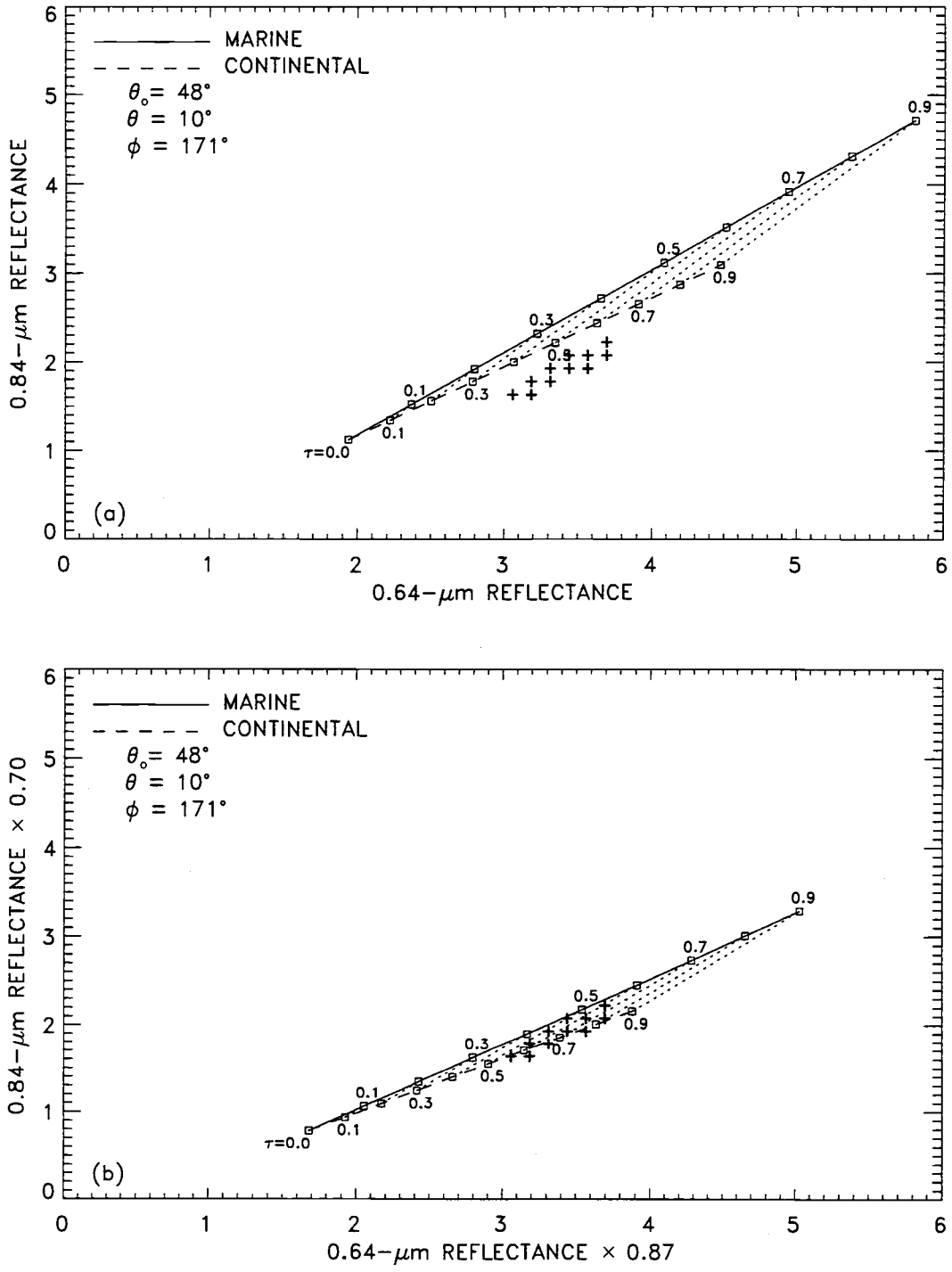

Figure 4.2. Same as Fig. 4.1 using the single scattering approximation for scattering (a), and with an adjustment for gaseous absorption (b).

atmosphere and surface were calculated. For cloud-free pixels, the diurnally averaged broadband radiative fluxes are given by

$$F = fF_C(\tau) + (1-f)F_M(\tau), \tag{4.5}$$

where, as in (4.1), f is the fraction of the mixture determined to be the average continental aerosol; $F_C(\tau)$ is the diurnally averaged radiative flux associated with the average continental aerosol for the optical depth at the standard wavelength, τ, and $F_M(\tau)$ is the corresponding flux for the tropical marine aerosol. The form of (4.5) for the radiative fluxes is justified because scattering by the cloud-free atmosphere approximates single-scattering for the range of 0.55-μm optical depths (0.1–0.9) being considered. The diurnally averaged quantities were derived assuming that the optical depth and mixing fraction remained constant at the retrieved values for the particular day and latitude-longitude box.

For the broadband radiative transfer model, the solar spectrum was divided into 13 spectral intervals: 12 intervals of approximately equal widths were distributed between 0.2 and 0.9 μm and one interval covered 0.9 – 4.0 μm and was used to account for absorption by water vapor as described by Lacis and Hansen (1974). Scattering and absorption by aerosols in the 0.9 – 4.0-μm band were calculated using optical properties at 1.0 μm. Optical depths for Rayleigh scattering were taken to be given by

$$\tau_{R\lambda} = \tau_{R0}\left(\frac{\lambda_0}{\lambda}\right)^4, \tag{4.6}$$

with $\tau_{R0} = 0.098$, the Rayleigh optical depth at $\lambda_0 = 0.55$ μm. The Rayleigh optical depths are consistent with the those given by Pendorf (1957). Rayleigh optical depths were set to zero for wavelengths greater than 0.9 μm. Absorption cross sections for ozone were taken from data given in Houghton (1989). Absorption calculated using these cross sections agree with the absorption calculated using the Lacis and Hansen (1974) parameterization. For these broadband fluxes the ocean albedo was taken to be Lambertian and the value was set to the planar albedo obtained from Cox and Munk (1954) for a surface wind speed of 5 m sec^{-1}. The ocean albedo is almost independent of wavelength and the spherical albedo is 0.06.

The aerosol direct radiative forcing was calculated for $1° \times 1°$ latitude-longitude regions. For regions that contained cloud-free pixels and for which no upper-level clouds were evident, the optical depth and aerosol mixing fraction derived for the cloud-free pixels were used to derive the diurnally averaged broadband fluxes for both the cloud-free portions of the region, and the portions overcast by low-level clouds. Regions were taken to contain only low-level clouds provided the 5^{th} percentile of the 11-μm emission for the pixels in the region satisfied $I_{5th} > I_C$ with $I_C = 75$ mWm^{-2} sr^{-1} cm, which is equivalent to a brightness temperature of 275 K and to the emission with opaque clouds at an altitude of 4 km in the tropics. I_C was chosen to be well below the mode of the 11-μm emission associated with pixels overcast by the low-level, layered clouds encountered in INDOEX.

For regions with only low-level clouds, the average radiative forcing was taken to be given by

$$F = \frac{[n_S + (1 - A_{CP})n_P]F_S + (A_{CP}n_P + n_O)F_O}{n}, \tag{4.7}$$

where F_S is the radiative flux for the cloud-free pixels; n_S is the number of cloud-free pixels; A_{CP} is the average fraction of the partly cloudy pixels that is overcast; n_P is the number of partly cloudy pixels; n_O is the number of pixels overcast by optically thick layered clouds; F_O is the flux associated with the overcast pixels, and n is the total number of pixels in the region. To determine A_{CP}, reflectances at 0.64 μm were taken to be given by the analogous relationship,

$$r = \frac{n_S r_S + (A_{CP}n_P + n_O)r_O}{n}, \tag{4.8}$$

where r_S is the average reflectance associated with cloud-free pixels and r_O is the average reflectance associated with pixels overcast by optically thick layered clouds. As noted in Section 4.5, r_O = 0.44 and A_{CP} = 0.48 are suitable average values for low-level clouds in the INDOEX region. For the range of viewing geometries used in the retrievals, the reflectance for overcast pixels is consistent with a visible optical depth of 8. In the evaluation of the aerosol direct radiative forcing for overcast regions, a cloud with a visible optical depth of 8 was imbedded in the haze between 1 and 2 km.

For the period being analyzed, cloud-free pixels in each 1° × 1° latitude-longitude region were used to derive an average mixing fraction, optical depth, top of the atmosphere and surface net solar radiative fluxes for cloud-free conditions.

For regions that contained no cloud-free pixels on a particular satellite pass, these average cloud-free radiative fluxes were used to determine the radiative fluxes for the portions of region estimated to be cloud-free at the time of observation. The average optical depth and aerosol mixing parameter were used to obtain the radiative fluxes for the portions of the region overcast by low-level, layered clouds.

Regions were taken to be overcast by upper-level clouds when their average 11-μm emission fell below I_C and their 0.64-μm reflectance was greater than r_O. The aerosol direct radiative forcing was set to zero for these regions. Two different approaches were used for regions that were not overcast by upper-level clouds but which, based on the 5th percentile of the 11-μm emission, contained upper-level clouds. In the first, the direct radiative forcing was set to zero for all 1° × 1° latitude-longitude regions that showed evidence of upper-level clouds. In the second, regions containing upper-level clouds were not included in the analysis. Instead, the radiative forcing for a particular geographic region was set to the average of all 1° × 1° latitude-longitude boxes for which no upper-level clouds were present. The effect of the latter approximation is to overestimate the direct radiative forcing due to the aerosol. Some of the upper-level clouds are bound to attenuate the effect of the aerosols on the top of the atmosphere and surface radiative fluxes. On the other hand, setting the radiative forcing to zero for all upper-level clouds leads to an underestimation of the direct radiative forcing due to aerosols. Thin cirrus and upper-level clouds that cover only a portion of a 1° × 1° latitude-longitude box will not fully attenuate the effect of the aerosol. Presumably, the average radiative forcing due to the aerosol falls between these two limiting cases. Finally, as discussed in Section 4.5, estimates of the top of the atmosphere and surface aerosol direct radiative forcing were made in which the forcing was also set to zero for portions of regions overcast by low-level layered clouds.

4.4 Comparison of Retrieved Optical Depths and Surface Measurements

The optical depths retrieved using the various schemes were compared with surface measurements. At KCO, NASA's Aerosol Robotic Network (AERONET) (Holben et al. 1998) maintained a CIMEL radiometer for which observations began in February 1998. Jayaraman et al. (2000) made shipboard measurements from the Indian RV *Sagar Kanya* beginning with cruises in 1996. During the February-March 1999 Intensive Field Phase (IFP) Devaux et al. (2000) made optical depth measurements from the INDOEX operations center on Hulule and Quinn et al. (2000) made observations from the NOAA RV *Ron Brown*. Figure 4.3 shows comparisons of retrieved aerosol optical depths for the 2-channel, 2-model retrieval scheme described in Section 4.2, and single-channel, single-model schemes using the FFP model, and the NOAA-Phase 1 and Phase 2 aerosol models. Surface and satellite observations were compared if they were within one hour of each other and the satellite observations yielded at least 12 cloud-free pixels suitable for aerosol retrievals within 30 km of the surface measurements. All matchups which satisfied these conditions are shown in Fig. 4.3. The error bars in the figure give the standard deviation of the retrieved optical depths for all pixels satisfying the matchup criteria and the standard deviation of the optical depths measured at the surface for the hour before and after the satellite overpass. Here, the surface observations at 0.67 μm were compared with retrieved optical depths at 0.65 μm. The retrieved optical depth was derived from the optical depth at the reference wavelength (0.55 μm) using the size distribution and the optical properties of the various components listed in Table 4.1. No corrections were applied to account for the effects of the small shift in wavelength between 0.65 and 0.67 μm. For the FFP model, the bias (0.055) and the RMS difference (0.070) are somewhat larger than those reported earlier (0.01 and 0.036, respectively) by Rajeev et al. (2000). The

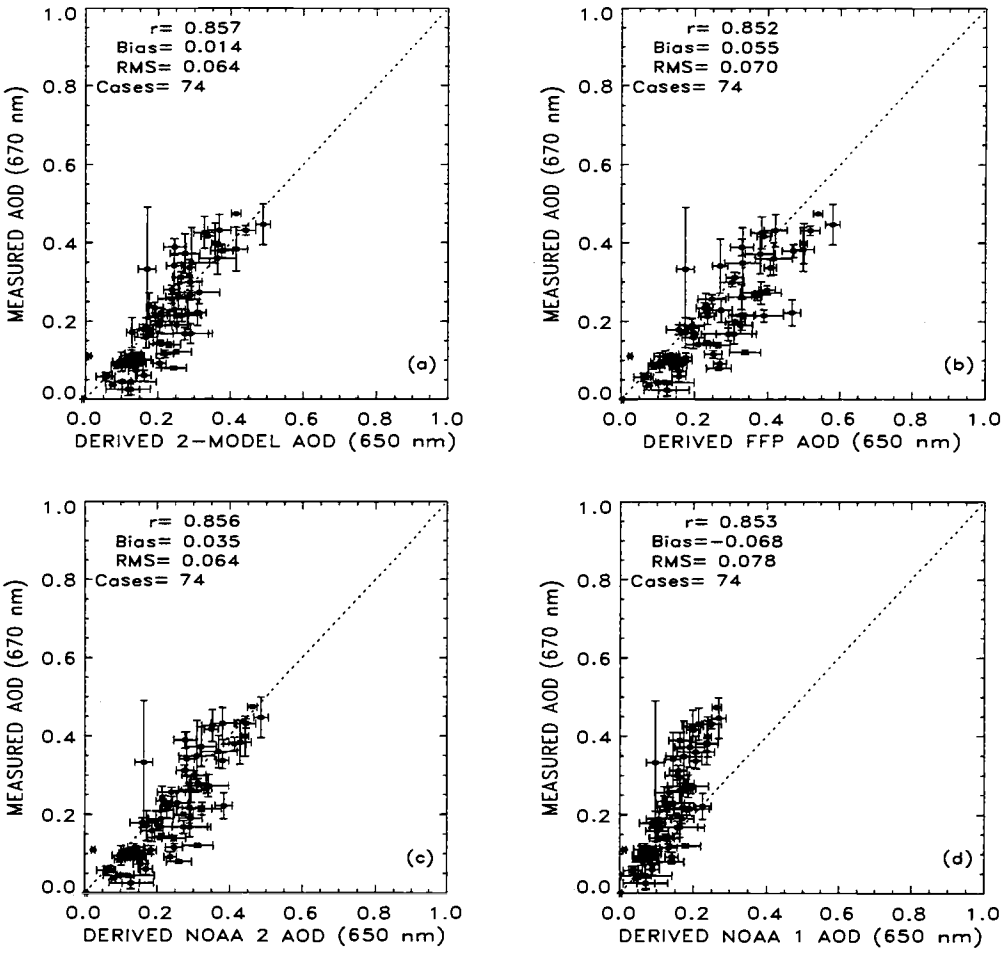

Figure 4.3. 0.67-μm optical depths measured by surface and shipboard sun photometers and 0.65-μm optical depths retrieved using a) the 2-channel, 2-model retrieval; b) the FFP model; c) the NOAA Phase 2 model; and d) the NOAA Phase 1 model. The FFP and NOAA retrievals are all single-channel retrievals. Error bars for the retrieved optical depths give the standard deviation for the fields of view that were within ± 30 km of the surface measurements. Error bars for the surface measurements give the standard deviation of the optical depths for ± 1 hr surrounding the satellite overpass.

differences are attributed to 1) the use of data for 1996-2000 in these comparisons as opposed to data for 1998 only in the earlier study; 2) the use of a different cloud-screening algorithm; 3) the use of different criteria for selecting observations for comparison, and 4) different ocean reflectances used in the retrievals. The current cloud screening and matchup criteria allow more points to be included in the comparison and thus account for the larger RMS difference. The difference in ocean reflectance probably accounts for the larger bias.

The results in Fig. 4.3 demonstrate that for all models, the retrieved optical depths were highly correlated with the optical depths measured at the surface. Furthermore, with the exception of the NOAA Phase 1 model, the various aerosol models and retrieval schemes yielded average differences with the surface measurements that were considerably smaller than the RMS differences. Also, the RMS differences were similar for all models. In other words, the NOAA Phase 1 model aside, no aerosol model or retrieval scheme provided significantly better agreement with the surface measurements of optical depths than the others. The shortcomings of the NOAA Phase 1 model were recognized earlier and motivated the switch to the Phase 2 model (Stowe et al. 1997).

As described in Section 4.2, the retrieval of aerosol properties reduced to a 2-channel, single-model retrieval scheme in which the RMS difference between observed and calculated 0.64 and 0.84-μm reflectances was minimized when the slope of the 0.84 to 0.64-μm reflectance relationship shown in Fig. 4.1 fell outside the range of values expected for the average continental and tropical marine aerosol models. Figure 4.4 compares the surface measurements to this two-channel, single aerosol model retrieval scheme for the NOAA Phase 2, the FFP, the tropical marine and the average continental aerosol models taken separately. For the NOAA Phase 2 and the FFP model, differences with the single-channel retrieval scheme are revealed through comparison of the results in Fig. 4.3b with 4.4a and Fig. 4.3c with 4.4b. In all cases, the biases are relatively small compared with the RMS differences about the mean difference. These results indicate that the reflectances at the two wavelengths measured by the AVHRR provide little additional constraint

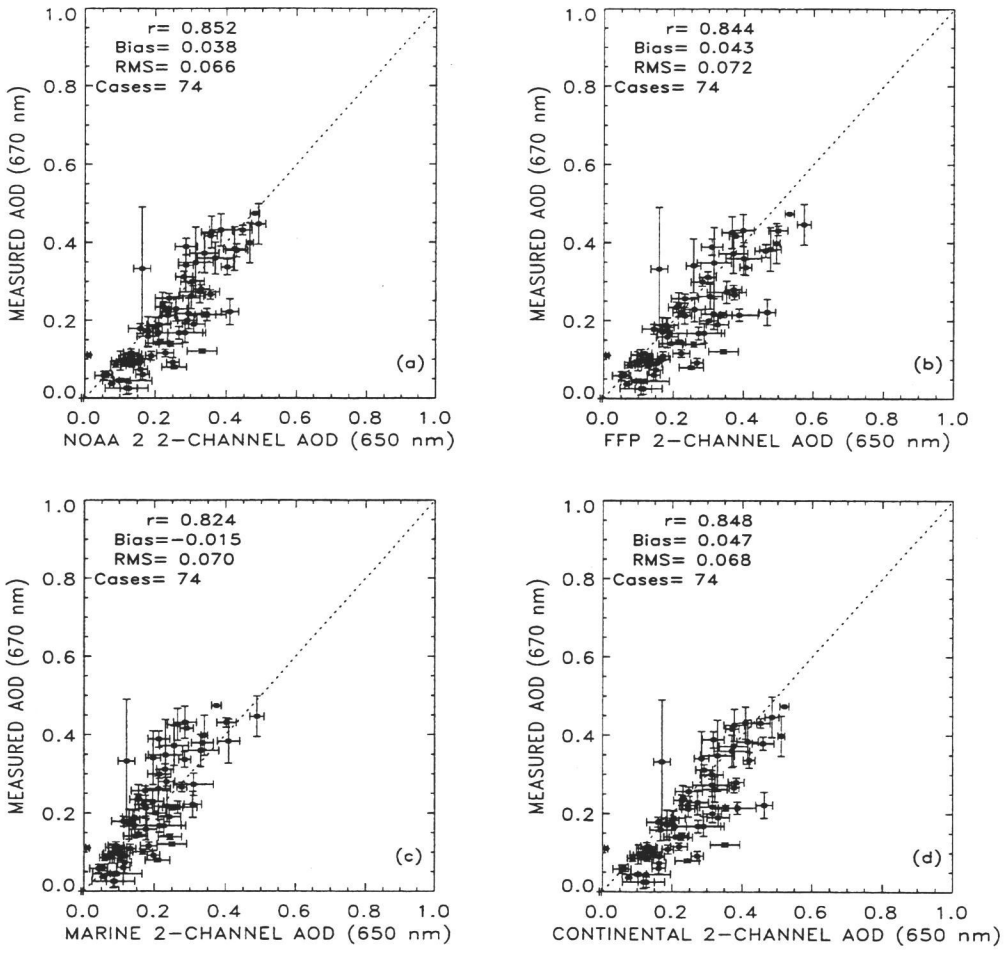

Figure 4.4. Same as Fig. 4.3 except that all retrievals are single aerosol model, 2-channel retrievals as described in Section 4.2. Results are for: a) the FFP model; b) the NOAA Phase 2 model; c) the tropical marine aerosol model; and d) the average continental aerosol model.

on aerosol properties. This finding may appear to contradict earlier work (Durkee et al. 1991; Higurashi and Nakajima 1999; Mischenko et al. (1999). In the earlier studies, however, differences in aerosol size indices were obtained only after compositing hundreds of retrievals in order to produce regional scale, monthly mean aerosol properties from daily observations. The 74 cases used here, even though they represent all possible matchups, were evidently too few to discover the benefits gained through using observations at the two wavelengths.

Figure 4.5 shows the optical depths retrieved at 0.90-μm and compared with values measured at the surface at 0.87 μm. As with the comparisons at visible wavelengths, no attempt was made to account for the small shift in wavelengths between the retrieved and measured optical depths. For the NOAA Phase 1 and Phase 2 models and for the FFP model, the 0.90-μm optical depths were obtained following the same procedures used to derive the 0.65-μm optical depths but with the Channel 2 (0.84 μm) reflectances replacing the Channel 1 (0.64 μm) reflectances for both the observed and calculated reflectances. For the 2-channel, 2-model retrieval scheme, the retrieved 0.90-μm optical depth was derived from the fractions retrieved for the two aerosol components and the optical depth at the standard wavelength retrieved for the aerosol mixture. The figure shows that the agreement at 0.90 μm was similar to that at 0.65 μm although the correlation between the satellite derived and surface-measured optical depths was somewhat weaker.

Instead of comparing optical depths, however, the value of the observations at two distinct wavelengths is better demonstrated by comparing the ratio of the retrieved optical depths at the two wavelengths with the corresponding ratio for the surface measurements, as is done in Figure 4.6. The dotted lines in the figure indicate the ratio of the optical depths that should have been obtained if the retrievals accurately represented the physical processes that gave rise to the observed reflectances. The scatter of results away from the lines reflects the

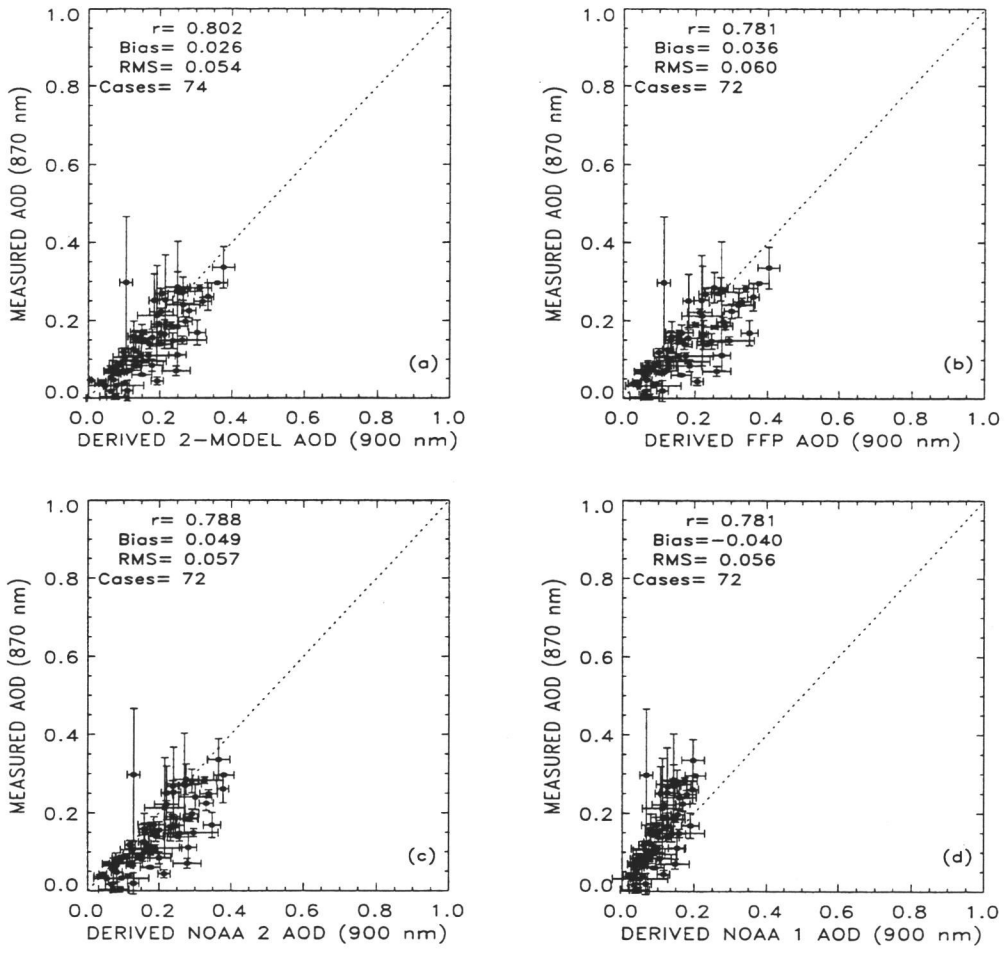

Figure 4.5. Same as Fig. 4.3 except for surface measurements at 0.87 μm and retrieved optical depths at 0.90 μm.

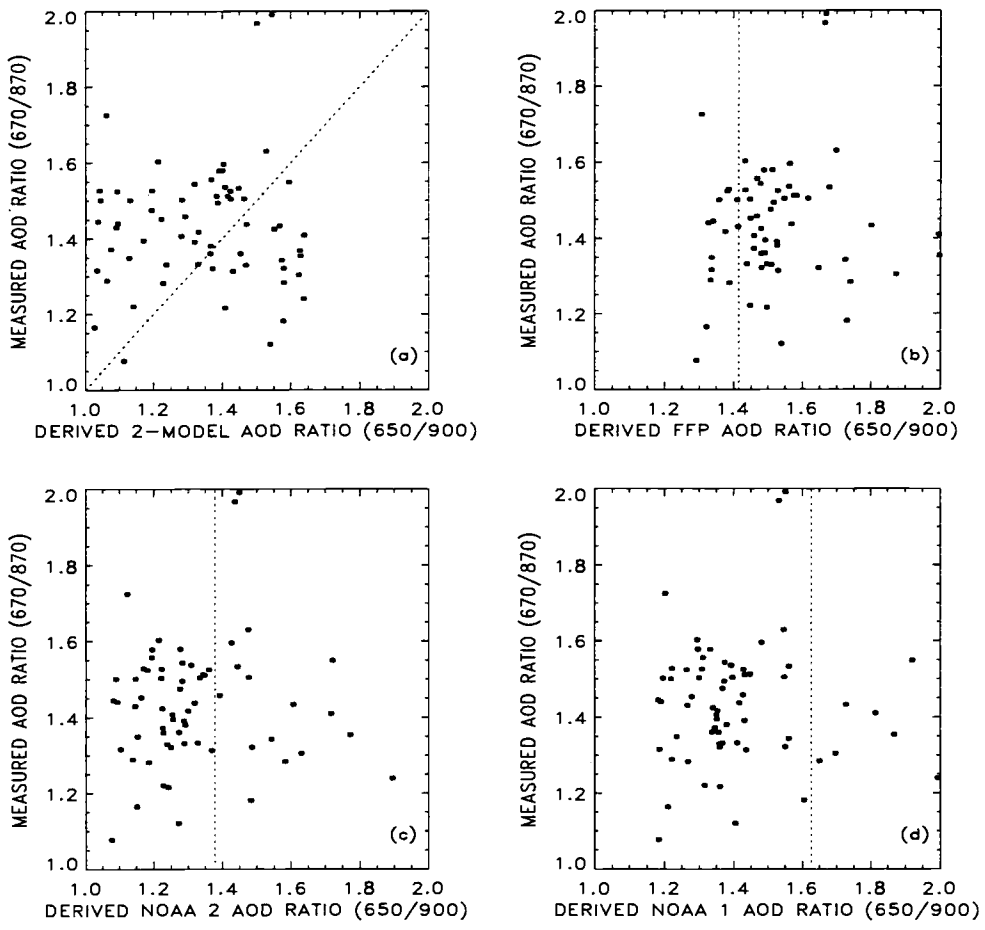

Figure 4.6. Ratios of optical depths at 0.67 and 0.87 μm for surface measurements and at 0.65 and 0.90 μm for optical depths retrieved from the NOAA-14 AVHRR, for a) the 2-channel, 2-model scheme; b) the FFP model; c) the NOAA Phase 2 model; and d) the NOAA Phase 1 model. Dotted lines indicate the ratios that would have been obtained had the processes that gave rise to the radiances been properly modeled in the retrieval schemes.

inadequacies in the retrievals. Such inadequacies are common to all retrieval schemes, regardless of which aerosol model is being used.

Because reflectances at 0.84 μm are affected by water vapor and those at 0.64 μm by ozone, optical depths and 0.84 to 0.64-μm optical depth ratios were derived using midlatitude profiles of water vapor and ozone instead of the tropical profiles. For the 2-channel, 2-model retrieval, the change in the profiles caused a change in optical depth of 0.028 at 0.65 μm and 0.002 at 0.90 μm. These changes had no perceptible effect on the appearance of the optical depth ratios shown in Fig. 4.6a.

4.5 Evaluation of Aerosol Direct Radiative Forcing

The sensitivity of the top of the atmosphere and surface net solar radiative fluxes to changes in aerosol concentrations is presented in Table 4.2 for the NOAA Phase 1, NOAA Phase 2, FFP, average continental, and tropical marine aerosols for cloud-free conditions. The results are for diurnally averaged shortwave radiative fluxes for 30°S – 30°N on 1 March, conditions appropriate for INDOEX. The sensitivities are normalized to unit 0.55-μm optical depth, but they were obtained by calculating the fluxes for small optical depths and for small changes in the optical depths such that the changes in the fluxes were linearly proportional to the changes in the optical depths. Table 4.2 also gives results for the tropical marine and average continental aerosols when the region is overcast by low-level cloud. As discussed in the previous section, these results were obtained for a cloud with visible optical depth of 8 imbedded in haze between 1 and 2 km. The net fluxes decrease with increasing aerosol burden with the exception of the top of the atmosphere flux for the average continental aerosol when optically thick low-level clouds, imbedded in the haze, become overcast. Under such conditions, absorption

Table 4.2. Radiative Forcing Sensitivity.

Aerosol Model	$dF/d\tau$ (Wm^{-2} Unit Optical $Depth^{-1}$)	
	Top of Atmosphere	Surface
Cloud-Free		
NOAA Phase 1	−55	−57
NOAA Phase 2	−40	−41
FFP	−23	−94
Tropical Marine	−38	−43
Average Continental	−30	−78
Overcast		
Tropical Marine	−10	−12
Average Continental	+10	−34

of sunlight by the aerosol is sufficient to reduce the albedo of the Earth-atmosphere system compared with its value for similarly overcast but aerosol-free conditions.

Figure 4.7 shows a comparison of observed top of the atmosphere radiative fluxes with those derived using the average continental and tropical marine aerosol models. The observed fluxes are obtained from the Clouds and Earth's Radiant Energy System (CERES) radiometer on the Tropical Rain Measurement Mission (TRMM) satellite. For all 1° × 1° latitude-longitude regions in which satellite cloud-free fields of view matched in time and were collocated with surface measurements of optical depth at KCO, the shortwave broadband radiance was

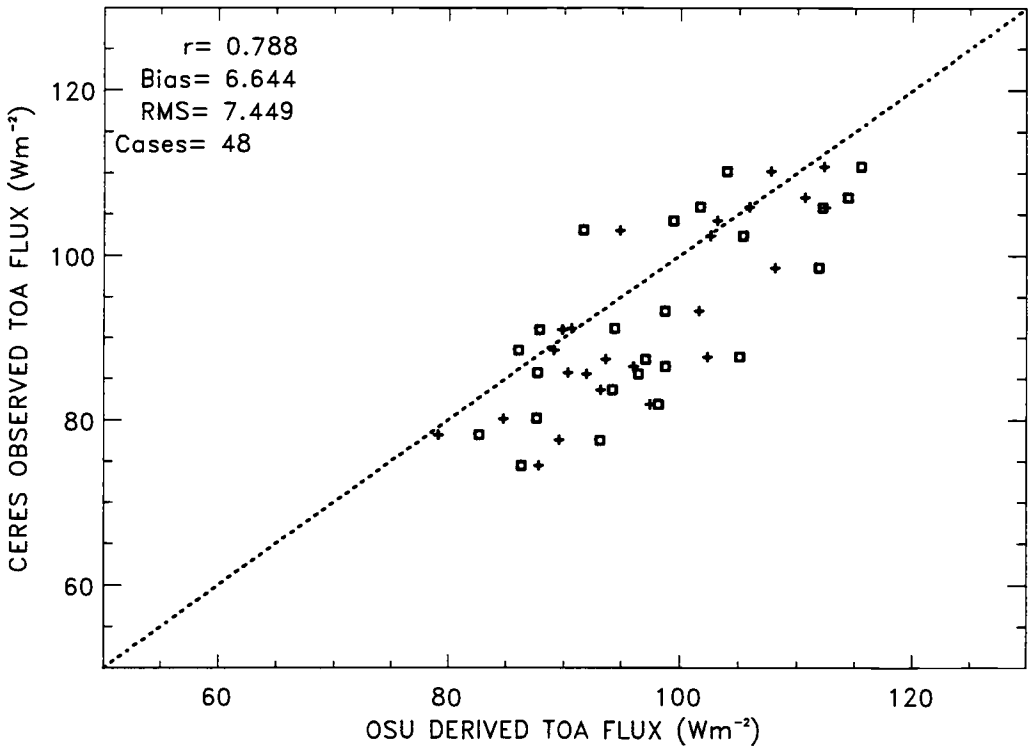

Figure 4.7. CERES and OSU-derived reflected shortwave fluxes for KCO when AERONET optical depths were available. Radiances from average continental (squares) and tropical marine (crosses) aerosol models were used to determine the derives radiative fluxes.

used in conjunction with radiance lookup tables for the two models to derive optical depths at the reference wavelength. These optical depths were then used in the broadband radiative transfer model to generate the radiative fluxes. As the figure indicates, the derived fluxes were fairly consistent with the CERES fluxes for both models, though the derived fluxes were somewhat larger than the CERES fluxes by about 6%.

For cloud-free conditions, the results in Table 4.2 illustrate the wide range of the aerosol direct radiative forcing possible for different aerosols. The radiative forcing is a function of aerosol particle size and the extent to which the aerosol absorbs sunlight. At the top of the atmosphere, the radiative flux is least sensitive per unit optical depth to the FFP model, for which the sensitivity is -23 Wm^{-2} per unit 0.55-μm optical depth. This sensitivity is close to the -25 Wm^{-2} per unit 0.5-μm optical depth value obtained by Satheesh and Ramanathan (2000) who correlated surface measurements of aerosol optical depths with top of the atmosphere radiative fluxes derived from CERES measurements. The top of the atmosphere flux is most sensitive to the NOAA Phase 1 aerosol, for which the sensitivity is -55 Wm^{-2} per unit 0.55-μm optical depth. As indicated in Table 4.1, the differences arise from the relatively strong absorption and relatively large particles in the FFP model, compared with the lack of absorption and relatively small particles in the NOAA Phase 1 model.

For the top of the atmosphere aerosol direct radiative forcing, however, the large sensitivity obtained for the NOAA Phase 1 model is compensated somewhat by the smaller optical depths retrieved using that model. The compensation is illustrated in Figure 4.8 which shows the top of the atmosphere aerosol direct radiative forcing under cloud-free conditions derived for the same cases that were used to compare retrieved and surface measurements of aerosol optical depth. In Fig. 4.8, the radiative forcing derived for the NOAA Phase 1, NOAA Phase 2, and the FFP models are compared with that derived using the 2-channel, 2-model scheme described in Section 4.2. Whereas the sensitivity of the top of the atmosphere radiative flux to optical depth for the NOAA Phase 1 model is more than twice that of the FFP model, the difference in the radiative forcing calculated for the NOAA Phase 1 model is only 40% greater than the forcing calculated for the FFP model. Also for comparison, Fig. 4.8d shows the direct radiative forcing for the FFP and average continental aerosol models based on the optical depths retrieved using only Channel 1 (0.64-μm) reflectances. The high degree of

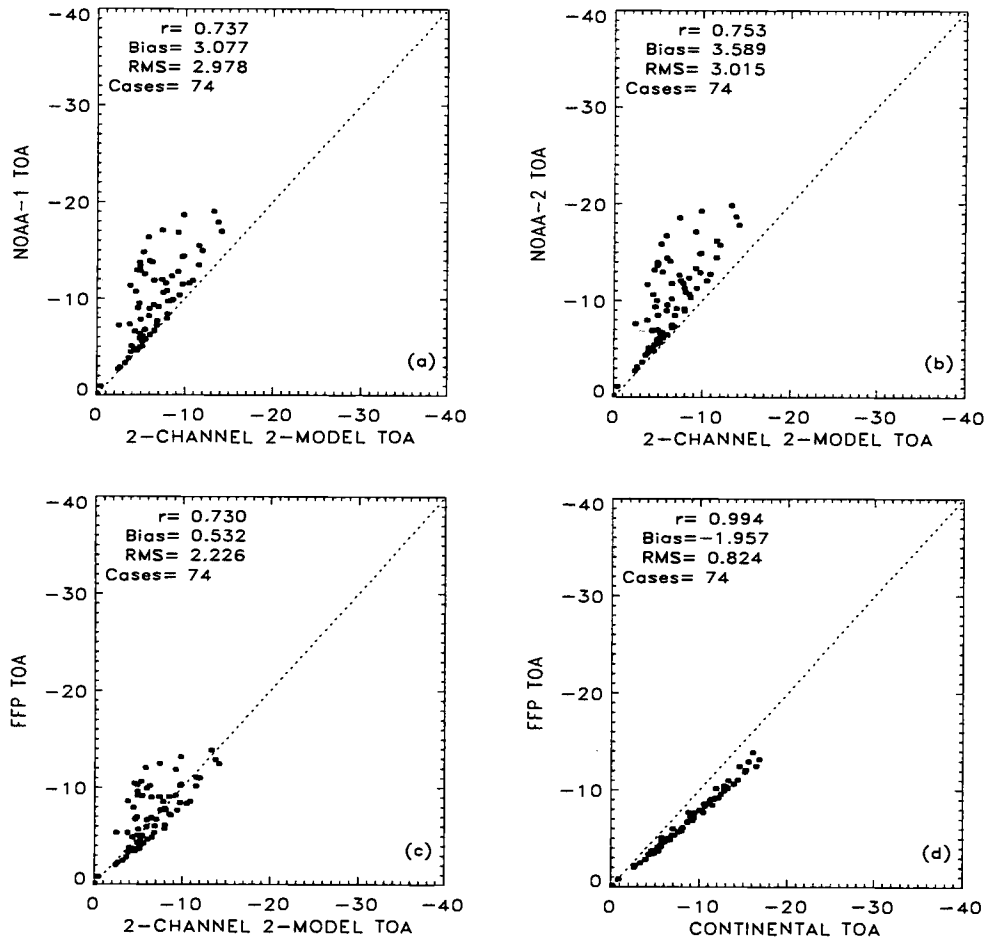

Figure 4.8. Top of the atmosphere, diurnally averaged, aerosol direct radiative forcing (Wm^{-2}) under cloud-free conditions for the cases used in Fig. 4.3. Results for the 2-model, 2-channel scheme are compared with a) the NOAA Phase 1 model, b) the NOAA Phase 2 model; and c) the FFP model. Results for the average continental aerosol model in a single-channel retrieval are compared with the FFP model in d).

correlation for the radiative forcing derived using the two models reflects the dependence of the forcing in both cases on the departure of the 0.64-μm reflectance from that expected for cloud-free and aerosol-free conditions. The FFP model absorbs more sunlight and thus produces somewhat less forcing than does the average continental model. Differences in the top of the atmosphere radiative forcing between the 2-channel, 2-model scheme and the other models is smallest for the FFP model. For the 2-channel, 2-model scheme the average radiative forcing is 6.8 Wm^{-2}, so the difference with the FFP model is less than 10% on average.

The reason that the broadband radiative forcing is highly correlated with the 0.64-μm reflectance is revealed in Figure 4.9. The figure shows that for the range of sun-earth-satellite viewing geometry: solar zenith angles, 0° – 85°, satellite zenith angles, 0° – 72°, and relative azimuth angles, 90° – 180°, lying outside the region of sun glint, and for 0.55-μm optical depths ranging from 0.1– 0.9, the calculated departures of the broadband reflectances from those expected for cloud-free and aerosol-free conditions are highly correlated with the corresponding departures calculated for the 0.64-μm reflectances. The lines in the figure are linear least squares fits relating the broadband to the narrow band reflectances. Results are shown for the FFP and NOAA Phase 1 models. These two models bracket the range of slopes for the least squares fits for all the models. Because the correlation is high, $r^2 > 0.93$, the results indicate that the departures of the reflectances at 0.64-μm from those expected for cloud-free and aerosol-free conditions are good predictors of the aerosol direct radiative forcing. Based on the least squares fits shown in Fig. 4.8, and for a departure of the 0.02 in the 0.64-μm reflectance from the reflectance associated with cloud-free and aerosol-free oceans, typical of the values obtained in INDOEX, the relative difference in the top of the atmosphere aerosol direct radiative forcing is less than 40%. This result is consistent with the results shown in Fig. 4.8.

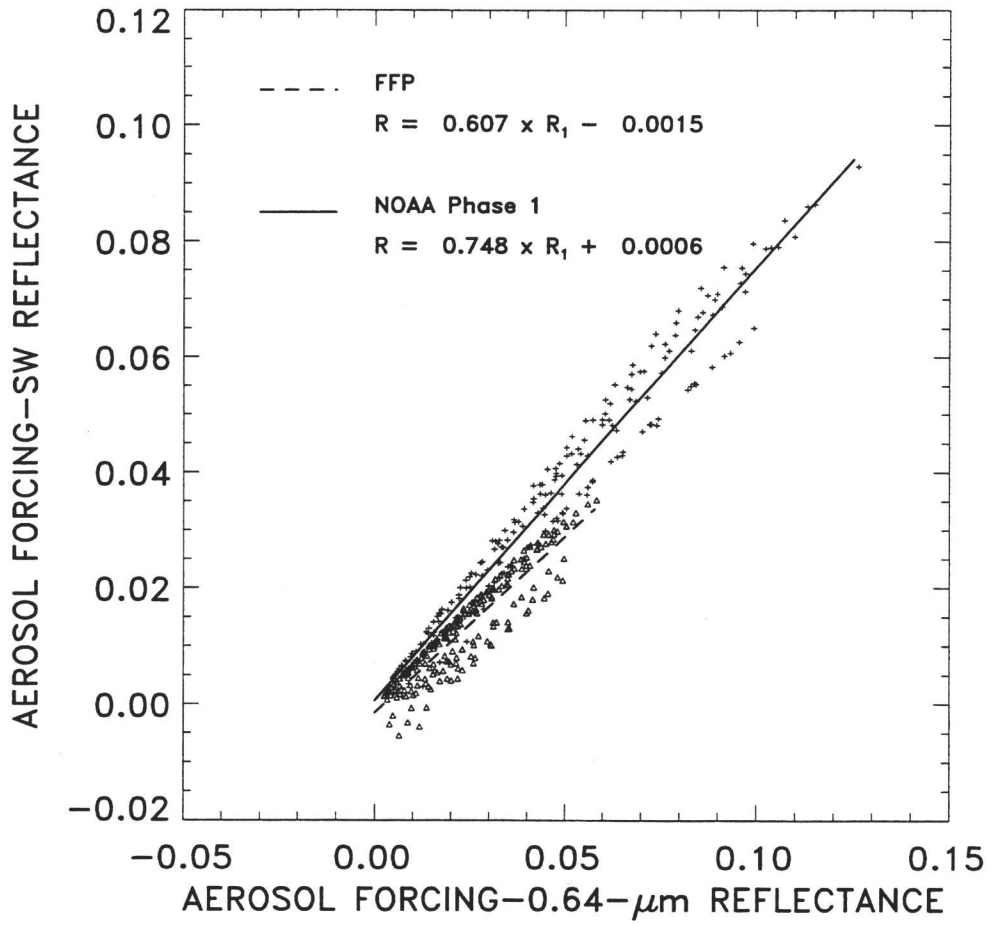

Figure 4.9. Departures of shortwave (0.2–4 μm) and 0.64-μm cloud-free ocean reflectances from aerosol-free values for all sun-target-satellite viewing geometries outside of the sun glint domain and in the direction of backscattered sunlight and for 0.55-μm optical depths (0.1–0.9). Lines are linear least squares fits to the reflectances for the FFP (dashed line, Δ) and the NOAA Phase 1 (solid line, +) models.

Figure 4.10 gives averages of the cloud-free aerosol direct radiative forcing calculated for an 8-day sample of NOAA-14 passes over the INDOEX region drawn from February and March 1999. The values in the parentheses are the

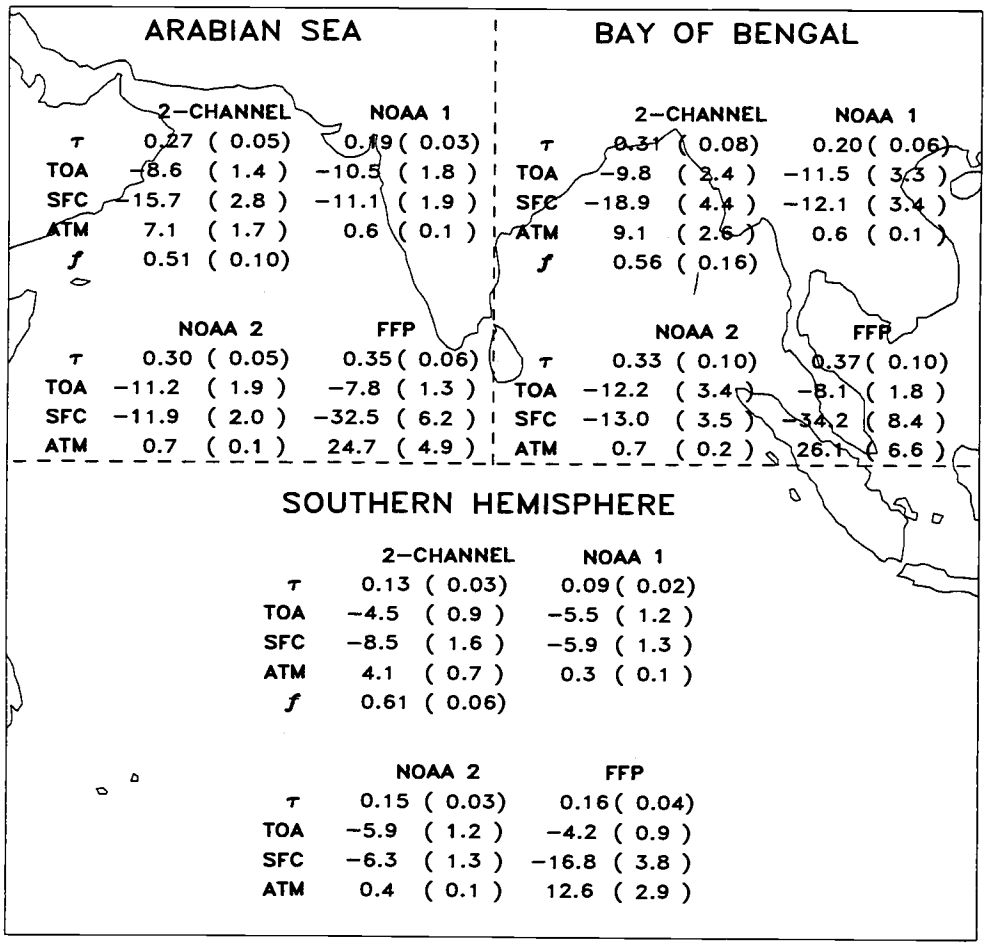

Figure 4.10. 8-day average, and standard deviation of the daily regional averages (parentheses) aerosol optical depths and the direct radiative forcing under cloud-free conditions for the Arabian Sea, Bay of Bengal, and the Indian Ocean in the Southern Hemisphere. The 8 days were sampled from the February–March 1999 INDOEX IFP.

standard deviation of the daily averages for the region and reflect the day-to-day variability in the regional means. The results show the differences obtained using the different aerosol models and retrieval schemes. The forcing represents the diurnally averaged, cloud-free radiative forcing for the Arabian Sea, the Bay of Bengal, and the Indian Ocean in the Southern Hemisphere. Consistent with the results in Figs. 4.8 and 4.9, the differences in the top of the atmosphere radiative forcing for the NOAA Phase 1 and FFP models are typically less than 40%, even though the optical depths retrieved using the two models differ by almost a factor of two. The optical depths, top of the atmosphere, and surface cloud-free aerosol direct radiative forcing shown in Fig. 4.10 are consistent with the sensitivities given in Table 4.2. Slight differences (~5%) result from departures of the observing dates from the 1 March date used in Table 4.2 and from allowance for small but systematic variations in the radiative forcing sensitivity with latitude. The average top of the atmosphere and surface radiative forcing obtained with the 2-channel, 2-model scheme is clearly a mixture of the radiative forcing obtained with the average continental and tropical marine models. This result is fortuitous in that the aerosol mixing fraction varied little from one region to the next. Had the retrieved optical depths and values of the mixing fraction been correlated, the average forcing would not necessarily have reflected the weighted average of the forcing associated with the component aerosols. The sensitivity per unit 0.55-μm optical depth of the surface forcing for the 2-channel, 2-model scheme lies in the −50 to −60 Wm^{-2} range, less than the −70 to −75 Wm^{-2} range deduced empirically by Satheesh and Ramanathan (2000), which in turn, is less than the −90 to −100 Wm^{-2} range obtained for the FFP model. For both the 2-channel, 2-model scheme and the FFP aerosol model, the atmospheric absorption due to the aerosol in the Southern Hemisphere is unrealistic given the lack of absorption found in the *in situ* aircraft and shipboard observations for the Southern Hemisphere (Clarke et al., 2000; Quinn et al., 2000).

Table 4.3 gives the diurnally averaged aerosol direct radiative forcing under average cloud conditions for the three regions shown in Fig. 4.10. The results are

for the same 8-day sample used to obtain the results shown in the figure. The values in parentheses are the standard deviations of the daily means for the regions. As discussed earlier, the diurnally averaged forcing is calculated by taking the aerosol properties and cloud conditions constant at the values deduced from the NOAA-14 afternoon observations and performing radiative transfer calculations for the variation of the incident sunlight associated with the date and latitude of the observations.

Table 4.3 also gives the cloud conditions in terms of the quantities described in Section 4.3. In particular, the table gives the average 0.64-μm reflectances for the AVHRR fields of view found to be overcast by optically thick, low-level, layered clouds, and the estimate of the cloud cover for partly cloudy pixels obtained using an average value of 0.44 for the overcast reflectance. As discussed in Section 4.3, Table 4.3 provides three estimates for the aerosol direct radiative forcing under average cloud conditions: 1) for all regions in which upper-level clouds were detected, the radiative forcing was set to zero, referred to as "Average Low"; 2) except for the relatively few cases in which upper-level clouds completely covered the $1° \times 1°$ latitude-longitude region, the radiative forcing was averaged only for regions that contained no upper-level clouds, referred to as "Average High," and 3) the radiative forcing was also set to zero for portions of regions overcast by low-level clouds, referred to as "Average-Zero, All Clouds." For all three estimates, the radiative forcing was set to zero for $1° \times 1°$ latitude-longitude regions overcast by upper-level clouds. Differences between "Average High" and "Average Low" were 60% for the top of the atmosphere radiative forcing. Because of the balance between average continental and tropical marine aerosols, and because of their compensating effects for the top of the atmosphere radiative forcing for scenes overcast by low-level clouds, the top of the atmosphere forcing obtained by setting the forcing to zero for all $1° \times 1°$ latitude-longitude regions that contained upper-level clouds and for all fractions of regions overcast by low-level clouds, "Average-Zero, All Clouds," fell close to that obtained for the "Average Low" estimates. In

all cases, the magnitude of the surface forcing obtained by setting the forcing to zero for either upper or low-level clouds is too small. As indicated by the results in Table 4.2, while clouds diminish the surface forcing somewhat, the resulting forcing remains a sizable fraction of that for cloud-free conditions. The range in values for the forcing given in Table 4.3 provides an estimate of the uncertainty that arises through the inability to characterize cloud conditions and the effect of the clouds on the aerosol direct radiative forcing.

Table 4.3. Composite regional means and (standard deviations of the daily regional means) for an 8-days sampled from February and March 1999. As described in the text, "Average Low," "Average High," and "Average-Zero, All Clouds," refer to extreme estimates of the radiative forcing under average cloud conditions.

Parameter	**Arabian Sea**	**Bay of Bengal**	**Southern Hemisphere**
Optical Depth	0.27 (0.05)	0.31 (0.08)	0.13 (0.03)
F	0.51 (0.10)	0.56 (0.16)	0.61 (0.06)
Frequencies of Occurrence			
Cloud-free pixels	0.23 (0.06)	0.13 (0.04)	0.08 (0.02)
Overcast pixels	0.01 (0.01)	0.02 (0.01)	0.04 (0.01)
Partly cloudy pixels	0.76 (0.06)	0.85 (0.04)	0.88 (0..03)
Regions containing upper level clouds, but not overcast	0.18 (0.06)	0.39 (0.09)	0.31 (0.08)
Regions overcast by upper level clouds	0.03 (0.01)	0.17 (0.08)	0.11 (0.06)
Low-level cloud properties			
Cloud cover, partly cloudy pixels	0.41 (0.03)	0.50 (0.07)	0.50 (0.06)
Reflectance, overcast pixels	0.27 (0.09)	0.57 (0.12)	0.47 (0.02)
Radiative Forcing (Wm^{-2})			
Cloud-Free			
TOA	− 8.6 (1.4)	− 9.8 (2.4)	− 4.5 (0.9)
Surface	− 15.7 (2.8)	− 18.9 (4.4)	− 8.5 (1.6)
Average-Low			
TOA	− 4.5 (0.8)	− 3.0 (1.2)	− 1.4 (0.2)
Surface	− 10.3 (1.8)	− 7.4 (2.9)	− 3.7 (0.6)
Average-High			
TOA	− 5.5 (0.9)	− 4.9 (1.9)	− 2.1 (0.2)
Surface	− 12.5 (2.2)	− 12.0 (4.3)	− 5.3 (0.6)
Average-Zero, All Clouds			
TOA	− 4.6 (0.8)	− 3.1 (1.2)	− 1.5 (0.2)
Surface	− 8.4 (1.6)	− 6.0 (2.4)	− 2.9 (0.5)

Chapter 5
The Retrieval of Aerosol Optical Depths and Radiative Forcing: Results

5.1 Introduction

Anthropogenic aerosols affect the Earth's climate in two ways: they reflect and absorb solar radiation, thereby giving rise to what is referred to as the direct radiative forcing, and they increase the numbers and decrease the sizes of cloud droplets, which increases cloud albedo, thereby giving rise to the indirect radiative forcing (Charlson et al. 1992; Andreae 1995, Charlson and Heintzenberg 1995). Both effects alter sunlight reflected and absorbed by the Earth-atmosphere system. These changes are expected to lead to changes in atmospheric and oceanic temperatures, and consequently, altered weather and climate variability patterns. Knowledge of the spatial distribution of aerosols and their effect on the Earth's energy budget is key to reliable assessments of climate change. The variability of aerosol concentrations coupled with the variability of their physical and optical properties makes direct measurements of aerosols and their properties on global scales impractical. Consequently, remote sensing of aerosols from satellites is essential to determining the temporal and spatial distribution of aerosols and estimating the aerosol direct radiative forcing of climate.

The Indian Ocean Experiment (INDOEX) was an intensive field experiment designed in part to determine the radiative forcing due to anthropogenic aerosols on regional (Arabian Sea and Indian Ocean) and seasonal (winter monsoon) scales. During the winter monsoon months of January to March, the Arabian Sea and the Indian Ocean are an ideal laboratory for the study of aerosols and their effect on the Earth's radiation budget. Monsoon winds from Asia transport aerosol rich

continental air from heavily populated areas of the Asian subcontinent to largely cloud-free ocean areas. Here, observations from the NOAA-14 Advanced Very High Resolution Radiometer (AVHRR) are used to determine the spatial and temporal distribution of aerosol optical depth and the effect of the aerosols on the radiation budget for the Indian Ocean for the period January to March, 1996-2000. The results provide the context for the 15 February–26 March 1999 INDOEX Intensive Field Phase (IFP), during which extensive surface, shipboard, and aircraft observations were made of the aerosol.

The method used to retrieve optical depths employed the optical properties of continental and marine aerosols in conjunction with the reflected sunlight at visible (0.64-μm, AVHRR Channel 1) and near infrared wavelengths (0.84-μm, AVHRR Channel 2) to determine the relative contributions of the two aerosol types and the optical depth of the mixture for each cloud-free pixel found to be suitable for retrieval (Coakley et al. 2000). The continental aerosol was chosen because it had relatively small particles and contained a substantial fraction of soot so that it absorbed sunlight. The marine aerosol by comparison had relatively large particles and was practically nonabsorbing. The 2-channel, 2-aerosol model retrieval scheme, unlike single-channel, single-model schemes (Stowe et al., 1997; Rajeev et al. 2000), was used to determine aerosol type and burden for each retrieval, so that in principle, variations in absorption due to aerosols could be allowed for in space and time. Consequently, the link between aerosol type and burden and the effects of the aerosol on the atmospheric and surface radiation budget could be explored. The retrieved mixing fractions, however, proved to be reasonably constant for all regions and all times. The spatial distributions of the optical depth and radiative fluxes for the Northern and Southern Hemispheres suggest that pollution sources on the Asian subcontinent have a nearly permanent influence in the Northern Hemisphere during the months of the winter monsoon.

The observations of optical depth and radiative fluxes allow analysis of the day-to-day and year-to-year variations on regional scales. Because aerosols have short atmospheric residence times and are subject to relatively efficient and rapid

removal processes, such as precipitation, their concentrations are best represented by asymmetric distribution functions, such as the gamma distribution function. Analysis of the variability in aerosol optical depths suggests that short term *in situ* measurements of aerosol concentrations offer few constraints for assessing the performance of models that calculate concentrations (e.g., Chin et al., 1996, Roelofs et al., 1998, Adams et al., 1999, among others) when the measured concentrations are compared with climatological concentrations generated by the models.

5.2 Analysis

Daily NOAA-14 AVHRR 4-km Global Area Coverage (GAC) measurements (Kidwell, 1994) were collected for January to March, 1996-2000. Analyses were performed for ascending daytime passes in the INDOEX region: 30°S to 30°N and 50°E to 110°E. Prior to performing the aerosol retrievals, reflectances in Channel 1, at 0.64 μm, and Channel 2, at 0.84 μm, were calibrated using the extensive ice sheets of Greenland and Antarctica (Tahnk and Coakley, 2000a,b).

The methods used to retrieve aerosol optical depths and the aerosol direct radiative forcing were described in Coakley et al. (2000). Briefly, each 4-km AVHRR GAC pixel was identified as being either cloud-free, partly cloud covered, or overcast by a single-layered, optically thick cloud system. For pixels identified as cloud-free ocean, outside the region of sun glint, and viewed in the direction of backscattered sunlight, reflectances in Channels 1 and 2 were used in a 2-channel, 2-aerosol model retrieval scheme to determine the relative concentration of continental and marine aerosols for the pixel and the optical depth at a standard wavelength, 0.55 μm, for the mixture. The relative concentration was expressed as

a mixing fraction: f = 1 for a mixture that was entirely continental, and $f = 0$ for a mixture that was entirely marine. The aerosol models used in the retrievals were the average continental aerosol and the tropical marine aerosol described by Hess et al. (1998). The relative concentration and optical depth were used along with the date and latitude of the observation to calculate the cloud-free, direct radiative forcing of the aerosol mixture at the top of the atmosphere and the surface. For each $1° \times 1°$ latitude-longitude region, the aerosol properties and cloud-free radiative forcing were composited along with the numbers of cloud-free, partly cloudy, and overcast pixels as well as other cloud related indices to form daily, monthly, and seasonal composites for each 1°-scale region. Estimates of the diurnally averaged radiative forcing were derived assuming that the aerosol mixture, optical depth, and cloud conditions encountered at the time of the NOAA-14 overpass were constant for the daylight hours.

Most of the cloud cover encountered in INDOEX failed to fill the 4-km field of view of the AVHRR GAC data. For broken cloud systems, cloud properties are defined by the method used to detect the clouds and extract the properties. Different methods produce different results (Wielicki and Parker, 1992). Consequently, the effect of clouds on the aerosol direct radiative forcing for INDOEX is rather uncertain. As discussed in Coakley et al. (2000), in order to determine how clouds affected the aerosol direct radiative forcing, several approximations were used to estimate the forcing for average cloud conditions. Here, the simplest of the approximation was adopted: the radiative forcing was set to zero for all $1° \times 1°$ latitude-longitude regions for which upper-level clouds were present, and for all portions of regions overcast by low-level clouds. The forcing obtained with this approximation was within 50% of that obtained for extreme conditions: a lower limit obtained by setting the forcing to zero for all regions that contained upper-level cloud but accounted for the forcing when low-level clouds were present, and an upper limit obtained by setting the forcing for regions with upper-level clouds equal to the average forcing obtained when only low-level clouds were present. Upper-level clouds were presumed to be present if the 5^{th}

percentile of the 11-μm emission for the region was less than 75 mWm^{-2} sr^{-1} cm, equivalent to a brightness temperature of 275 K and to an opaque cloud at 4 km in a tropical atmosphere. Of the regions that met this condition, less than 15% also had any cloud-free pixels, indicating that the regions were largely cloud covered. Setting the forcing to zero for such regions mimics the attenuation of the effects of the aerosol on the top of the atmosphere and surface radiative fluxes when the aerosol layer lies beneath the cloud. The surface forcing, of course, is nonzero for all but the thickest of clouds; setting the forcing to zero for overcast regions will lead to area-averaged estimates that are too small. In the case of low-level clouds, setting the forcing to zero at the top of the atmosphere is consistent with the cancellation of the forcing for the average continental and tropical marine aerosols when low-level clouds are imbedded in the haze (Coakley et al., 2000). Because it absorbs sunlight, the average continental aerosol leads to a reduction in planetary albedo for regions overcast by low-level clouds that are imbedded in the haze. The tropical marine aerosol is nonabsorbing and, for a given optical depth, increases the albedo of regions overcast by low-level clouds by an amount that is comparable to the reduction caused by the average continental aerosol. The near cancellation of the top of the atmosphere aerosol direct radiative forcing for overcast, low-level clouds arose in INDOEX because, as will be shown later, the mixing fractions of the two aerosols were approximately the same for all regions and all years.

For regions that had no upper-level clouds, the fraction of the region overcast by low level clouds was estimated by taking the average fractional coverage for partly cloudy pixels to be 0.48. This value was consistent with comparisons of 0.64-μm reflectances for pixels overcast by low-level, layered clouds, and the reflectances for pixels that were only partly covered by these clouds.

For estimates of the aerosol optical depth, mixing fraction, and cloud-free radiative forcing, tests were performed to determine how many cloud-free pixels, suitable for retrievals within a $1° \times 1°$ latitude-longitude box, were required to ensure that the average properties derived for the box represented the true mean for the region. For this test, sixty passes were randomly chosen from the 3 months of

each of the 5 years so that each pass had at least one 1° square that contained at least 50 cloud-free pixels suitable for aerosol retrievals. For each pass, a set of 20 randomly selected optical depths were extracted from a single 1° square that contained more than 50 pixel-scale aerosol retrievals. As shown in Figure 5.1, RMS differences of the mean optical depth from the true mean for the square were calculated as a function of the number of observations included in the average. The true mean was obtained by averaging over all cloud-free pixels suitable for aerosol retrievals in the square. For all of the years studied, 12 observations within a square produced an average 0.55-μm optical depth that differed from the true mean with an RMS difference of 0.04. Consequently, a minimum of 12 cloud-free pixels suitable for aerosol retrievals within a 1° × 1° latitude-longitude region was imposed in order for the region to be included in the daily composite.

As was done for the daily composites, tests were performed to determine the number of daily observations required for each 1° × 1° latitude-longitude region in order to obtain a representative monthly mean. Using daily composites for all satellite passes for each month of the 5-year period, RMS differences between the mean for a 1° square and its true mean were calculated as a function of the number of daily composites contributing to the monthly mean. Only regions that contained at least 20 daily composites were included in this test. Figure 5.2 shows RMS departures of the monthly average aerosol optical depth for 1° × 1° latitude-longitude regions as a function of the number of daily values included in the average. The Arabian Sea, Bay of Bengal, and Southern Hemisphere were treated separately since they appeared to exhibit distinctly different aerosol regimes. In addition, a distinction was made between low and high optical depths within a region. As will be discussed later, for regions that have mean optical depths that are small, the standard deviations are also small. Consequently, the RMS differences for these regions showed little sensitivity to the number of daily estimates used to form a monthly mean. Regions with large mean optical depths, on the other hand, also had large standard deviations in optical depth. For such regions RMS differences between the mean and true mean generally decreased as

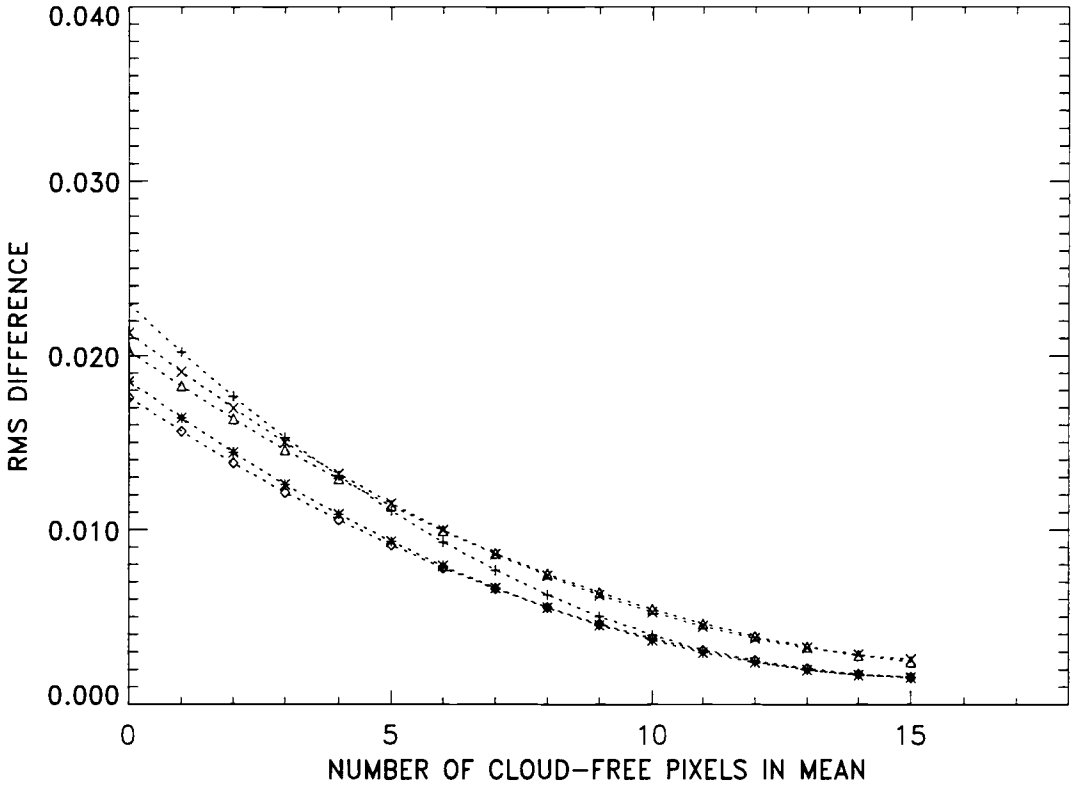

Figure 5.1. RMS departure of the daily average aerosol optical depth from the true average optical depth for 1° × 1° latitude-longitude regions as a function of the number of 4-km cloud-free pixels used to obtain the average. RMS differences are plotted for years 1996 (+), 1997 (*), 1998 (◊), 1999 (Δ), and 2000(×).

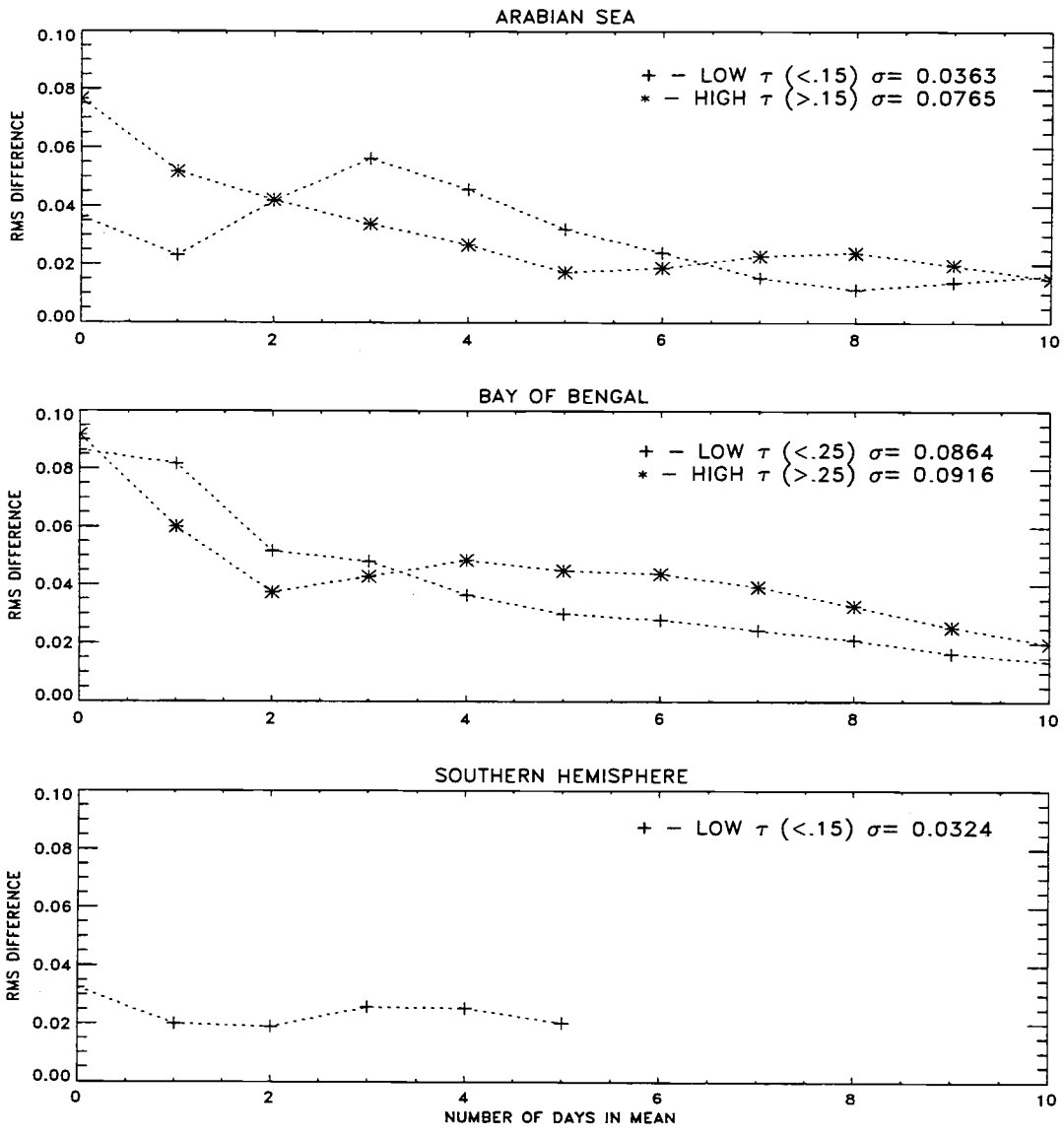

Figure 5.2. RMS departure of monthly average aerosol optical depth from the true average for 1° × 1° latitude-longitude regions as a function of the number of daily values included in the average. RMS differences are plotted for low and high optical depths in the Arabian Sea and Bay of Bengal, and low optical depths in the Southern Hemisphere. The standard deviation of the 1° × 1° latitude-longitude regional means is shown for each region and optical depth condition.

the number of daily estimates used to compute the monthly mean increased. For all of the years studied, monthly means constructed from 5 daily estimates produced an optical depth that departed from the true mean with an RMS difference of 0.04. At least 5 daily composites were required in order for a $1° \times 1°$ latitude-longitude region to be counted in the monthly composites.

Seasonal composites for each year and each $1° \times 1°$ latitude-longitude region were then constructed from the monthly mean composites. The seasonal composites for each of the 5 years were combined to construct the 5-year composite and the year-to-year variations within the 5-year period.

5.3 Aerosol Optical Depths and Mixing Fractions

Figure 5.3 shows the seasonal averages for each of the 5 years and Figure 5.4 shows the 5-year seasonal average optical depth at 0.55 μm and its year-to-year standard deviation for the INDOEX region. The boxes in Fig. 5.4 identify the regions referred to as the Arabian Sea, the Bay of Bengal, and the Indian Ocean in the Southern Hemisphere. The figure also shows $10° \times 10°$ latitude-longitude subregions which will be discussed later. These subregions were chosen because the aerosol properties were expected to be reasonably homogeneous with regard to sources and they represented regions that were heavily polluted and regions that were relatively pristine. Table 5.1 gives the regional averages of the aerosol mixing fraction, optical depths, cloud conditions, and aerosol direct radiative forcing for each year and each region.

A dominant feature of the year-to-year composites shown in Fig. 5.3 is the persistence of a large area in the Arabian Sea and Bay of Bengal characterized by high optical depths. Figure 5.5 shows the surface winds for January 1999 obtained

Table 1a. Composite statistics (mean and day-to-day regional variation) for 1996 and the specified regions.

Parameter	Arabian Sea	Bay of Bengal	No Hem	So Hem
Optical Depth	0.23(0.03)	0.31(0.09)	0.25(0.03)	0.15(0.03)
f	0.70(0.11)	0.76(0.12)	0.72(0.10)	0.64(0.09)
Frequency of Occurrence				
Cloud-free pixels	0.19(0.08)	0.10(0.06)	0.15(0.06)	0.09(0.03)
Overcast pixels	0.01(0.01)	0.04(0.04)	0.02(0.02)	0.03(0.01)
Partly cloudy pixels	0.79(0.08)	0.86(0.06)	0.82(0.05)	0.89(0.03)
Regions containing upper level clouds	0.22(0.10)	0.43(0.14)	0.32(0.08)	0.48(0.11)
Regions overcast by upper level clouds	0.04(0.03)	0.09(0.07)	0.06(0.03)	0.07(0.04)
Radiative Forcing (Wm^{-2})				
Cloud-free				
Top of the atmosphere	-7.4(1.0)	-9.5(2.3)	-8.1(1.0)	-5.3(0.9)
Surface	-15.2(2.4)	-20.8(5.9)	-17.1(2.4)	-10.3(1.4)
Atmosphere	7.8(1.6)	11.4(3.7)	9.0(1.6)	5.0(0.6)
Average				
Top of the Atmosphere	-3.5(0.8)	-2.7(0.8)	-3.2(0.6)	-1.6(0.3)
Surface	-7.3(1.8)	-6.0(2.0)	-6.7(1.4)	-3.0(0.5)
Atmosphere	3.8(1.3)	3.3(1.4)	3.5(1.0)	1.4(0.4)

Table 1b. Composite statistics (mean and day-to-day regional variation) for 1997 and the specified regions.

Parameter	Arabian Sea	Bay of Bengal	No Hem	So Hem
Optical Depth	0.27(0.04)	0.31(0.06)	0.29(0.03)	0.17(0.04)
f	0.73(0.13)	0.79(0.12)	0.75(0.11)	0.73(0.10)
Frequency of Occurrence				
Cloud-free pixels	0.20(0.07)	0.12(0.06)	0.16(0.05)	0.08(0.03)
Overcast pixels	0.01(0.01)	0.03(0.02)	0.02(0.01)	0.04(0.02)
Partly cloudy pixels	0.79(0.07)	0.85(0.06)	0.82(0.05)	0.88(0.03)
Regions containing upper level clouds	0.22(0.13)	0.41(0.13)	0.31(0.10)	0.45(0.12)
Regions overcast by upper level clouds	0.04(0.04)	0.09(0.06)	0.06(0.04)	0.07(0.04)
Radiative Forcing (Wm^{-2})				
Cloud-free				
Top of the atmosphere	-8.7(1.3)	-9.6(1.6)	-9.1(1.0)	-6.0(1.4)
Surface	-18.1(2.3)	-21.3(4.0)	-19.4(2.1)	-12.4(2.4)
Atmosphere	9.4(1.5)	11.8(2.6)	10.3(1.5)	6.4(1.2)
Average				
Top of the Atmosphere	-4.2(0.9)	-3.1(1.0)	-3.7(0.8)	-1.9(0.3)
Surface	-8.9(1.9)	-7.0(2.3)	-7.9(1.8)	-3.7(0.6)
Atmosphere	4.7(1.4)	3.9(1.6)	4.2(1.3)	1.8(0.4)

Table 1c. Composite statistics (mean and day-to-day regional variation) for 1998 and the specified regions.

Parameter	Arabian Sea	Bay of Bengal	No Hem	So Hem
Optical Depth	0.23(0.04)	0.30(0.06)	0.26(0.04)	0.16(0.03)
f	0.67(0.11)	0.80(0.10)	0.72(0.09)	0.69(0.08)
Frequency of Occurrence				
Cloud-free pixels	0.18(0.08)	0.13(0.06)	0.15(0.06)	0.08(0.03)
Overcast pixels	0.01(0.01)	0.03(0.02)	0.02(0.01)	0.02(0.01)
Partly cloudy pixels	0.81(0.08)	0.85(0.06)	0.83(0.06)	0.89(0.02)
Regions containing upper level clouds	0.24(0.14)	0.38(0.12)	0.31(0.09)	0.51(0.12)
Regions overcast by upper level clouds	0.04(0.04)	0.09(0.04)	0.06(0.03)	0.08(0.04)
Radiative Forcing (Wm^{-2})				
Cloud-free				
Top of the atmosphere	-7.5(1.2)	-9.4(1.7)	-8.3(1.0)	-5.5(1.1)
Surface	-15.2(2.3)	-21.2(4.2)	-17.7(2.2)	-11.2(2.0)
Atmosphere	7.6(1.5)	11.9(2.7)	9.4(1.4)	5.6(1.1)
Average				
Top of the Atmosphere	-3.5(0.9)	-3.2(0.8)	-3.3(0.6)	-1.6(0.3)
Surface	-7.0(1.9)	-7.2(1.9)	-7.1(1.5)	-3.1(0.5)
Atmosphere	3.5(1.4)	4.0(1.4)	3.8(1.0)	1.5(0.4)

Table 1d. Composite statistics (mean and day-to-day regional variation) for 1999 and the specified regions.

Parameter	**Arabian Sea**	**Bay of Bengal**	**No Hem**	**So Hem**
Optical Depth	0.24(0.04)	0.31(0.06)	0.27(0.03)	0.13(0.02)
f	0.53(0.13)	0.59(0.17)	0.55(0.12)	0.61(0.06)
Frequency of Occurrence				
Cloud-free pixels	0.20(0.07)	0.10(0.05)	0.15(0.06)	0.08(0.02)
Overcast pixels	0.01(0.01)	0.04(0.03)	0.02(0.02)	0.04(0.02)
Partly cloudy pixels	0.79(0.07)	0.86(0.06)	0.83(0.05)	0.88(0.02)
Regions containing upper level clouds	0.23(0.12)	0.46(0.10)	0.35(0.08)	0.42(0.11)
Regions overcast by upper level clouds	0.04(0.03)	0.08(0.05)	0.06(0.03)	0.06(0.03)
Radiative Forcing (Wm^{-2})				
Cloud-free				
Top of the atmosphere	-8.0(1.3)	-9.9(1.7)	-8.7(1.0)	-4.8(0.9)
Surface	-14.7(2.7)	-19.2(3.5)	-16.3(2.1)	-9.1(1.4)
Atmosphere	6.7(1.7)	9.3(2.6)	7.6(1.6)	4.4(0.6)
Average				
Top of the Atmosphere	-3.8(0.9)	-2.7(0.9)	-3.2(0.7)	-1.7(0.3)
Surface	-7.1(1.8)	-5.3(1.8)	-6.2(1.4)	-3.1(0.5)
Atmosphere	3.3(1.4)	2.6(1.4)	3.0(1.0)	1.4(0.4)

Table 1e. Composite statistics (mean and day-to-day regional variation) for 2000 and the specified regions.

Parameter	**Arabian Sea**	**Bay of Bengal**	**No Hem**	**So Hem**
Optical Depth	0.24(0.05)	0.27(0.07)	0.25(0.04)	0.15(0.04)
f	0.41(0.14)	0.59(0.14)	0.47(0.12)	0.54(0.10)
Frequency of Occurrence				
Cloud-free pixels	0.22(0.08)	0.09(0.05)	0.16(0.06)	0.07(0.02)
Overcast pixels	0.02(0.01)	0.04(0.03)	0.03(0.01)	0.03(0.01)
Partly cloudy pixels	0.75(0.11)	0.87(0.11)	0.81(0.10)	0.89(0.10)
Regions containing upper level clouds	0.21(0.11)	0.56(0.13)	0.37(0.09)	0.50(0.10)
Regions overcast by upper level clouds	0.03(0.03)	0.13(0.08)	0.07(0.04)	0.10(0.04)
Radiative Forcing (Wm^{-2})				
Cloud-free				
Top of the atmosphere	-8.2(1.5)	-8.6(2.1)	-8.3(1.4)	-5.4(1.2)
Surface	-13.7(2.6)	-16.6(4.2)	-14.6(2.5)	-9.8(1.8)
Atmosphere	5.5(1.6)	8.1(2.5)	6.3(1.4)	4.4(0.7)
Average				
Top of the Atmosphere	-4.2(0.7)	-1.7(0.6)	-2.9(0.5)	-1.4(0.2)
Surface	-7.0(1.3)	-3.5(1.2)	-5.1(1.1)	-2.7(0.4)
Atmosphere	2.8(1.0)	1.8(0.9)	2.2(0.8)	1.3(0.3)

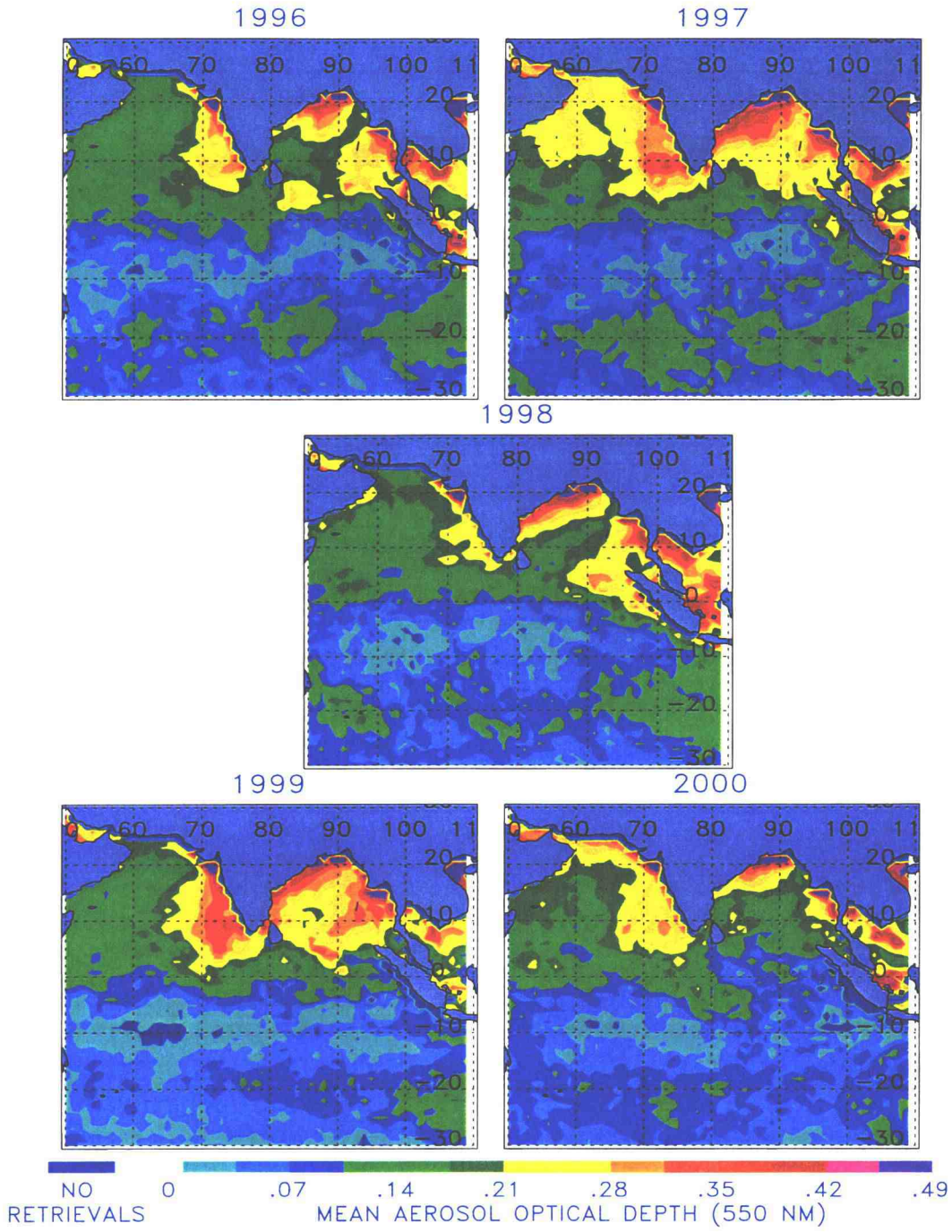

Figure 5.3. January-March composites of aerosol optical depth for 1996-2000.

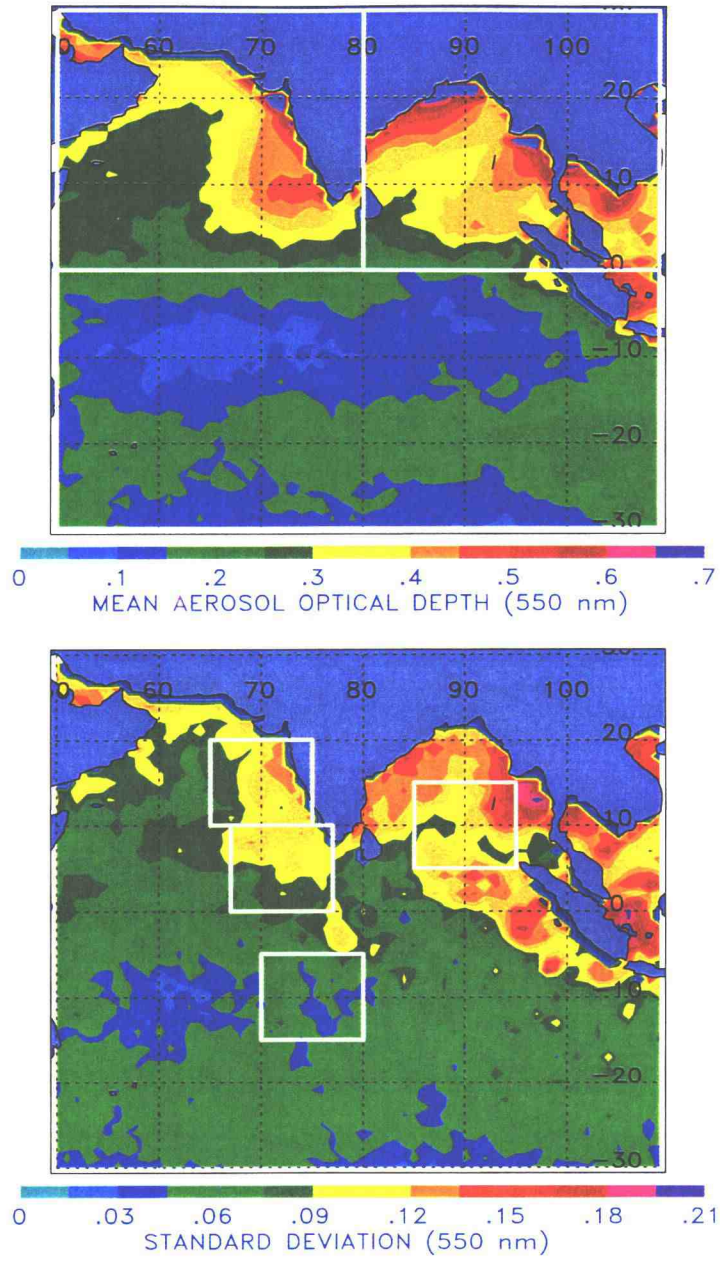

Figure 5.4. 5-year January-March average and year-to-year standard deviation of 0.55-μm optical depth. The boxes in the figures identify regions and 10° × 10° latitude-longitude subregions referenced in the analysis.

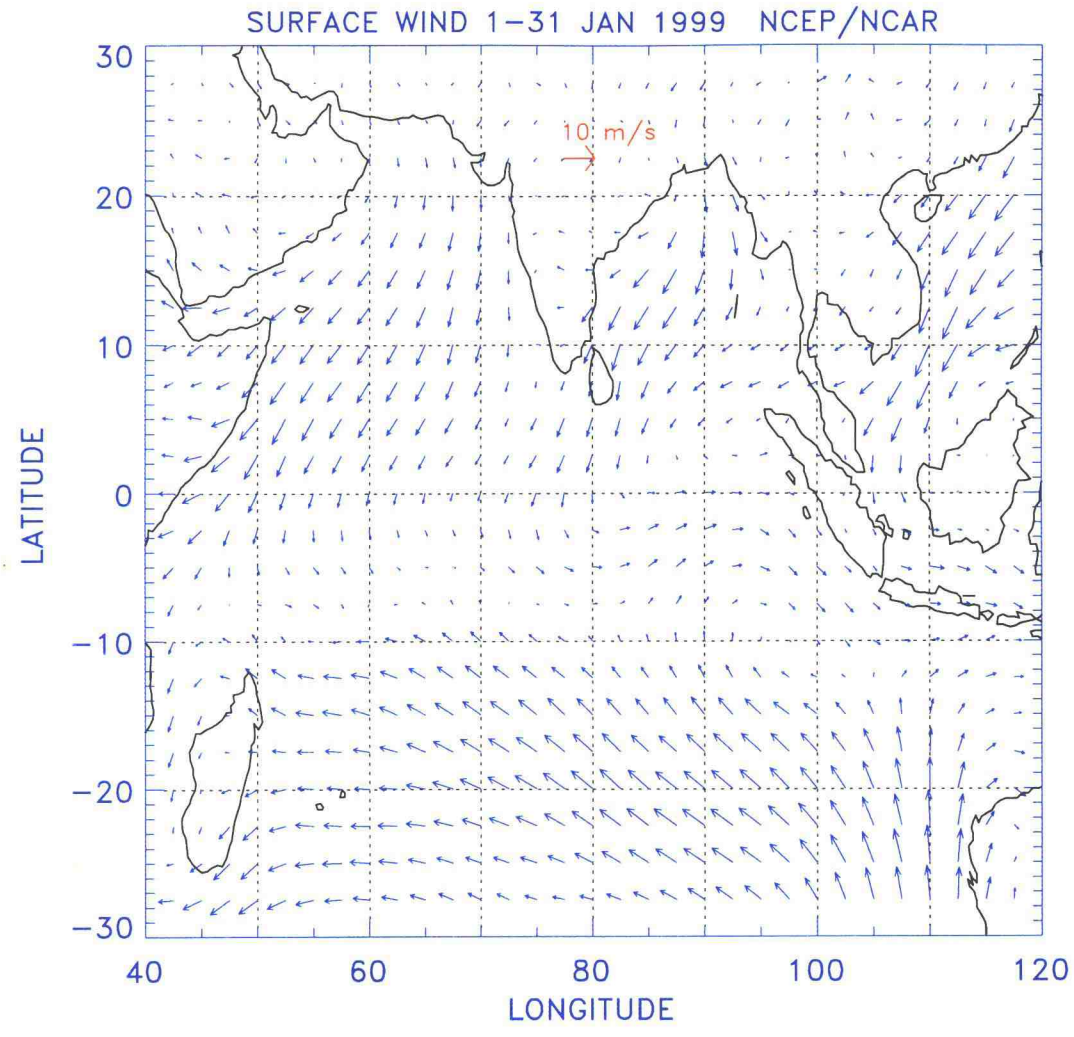

Figure 5.5. Prevailing monthly mean atmospheric circulation at the surface during January 1999 based on the NCEP/NCAR Reanalysis (from http://www.cdc.noaa.gov).

transport of aerosols from the continental areas into otherwise pristine ocean regions. Northeasterlies transport aerosols from the Indian subcontinent into the Arabian Sea and from the Indian subcontinent and Southeast Asia into the Bay of Bengal. Optical depths in the Bay of Bengal were unusually high during February and March 1999 when particles from extensive forest fires in Southeast Asia were transported into the Bay of Bengal where they stagnated.

Both the mean optical depth and its year-to-year standard deviation mark the regions affected by pollution haze and suggest the likely sources of the haze. As indicated by the optical depths in the Southern Hemisphere, pristine oceans appear to have low optical depths that rarely exceed 0.2. Polluted regions have optical depths that range from 0.2 – 0.3 and higher, depending on their proximity to sources. The spatial pattern of the optical depth and its standard deviation suggests that the Asian subcontinent affects the entire Northern Hemisphere region. On the seasonal scale, differences between optical depths in the Northern and Southern Hemisphere regions leads to the conclusion that the optical depths are elevated by at least 0.05 due to the sources of haze pollution, with the increases being substantially larger, 0.1 – 0.3, depending, of course, on the distance to the pollution sources.

Figure 5.6 shows monthly averages and daily standard deviations of regional means for the Arabian Sea, the Bay of Bengal, and the Indian Ocean in the Southern Hemisphere. There is little trend in the regional scale optical depths either with month or year. Climatologically, the elevated optical depths in the Northern Hemisphere appear to be a constant feature. For the $10° \times 10°$ latitude-longitude subregions, differences between monthly mean optical depths are, of course, more apparent, as shown in Figure 5.7. During the IFP the optical depths were among the largest obtained for the Arabian Sea and the Bay of Bengal during the 5-year period.

The regional scale monthly means and daily standard deviations for the aerosol mixing fraction, f, are shown in Figure 5.8. Again, with the exception of the results for 1999 and 2000, there is no obvious trend in the mixing parameter. The radical

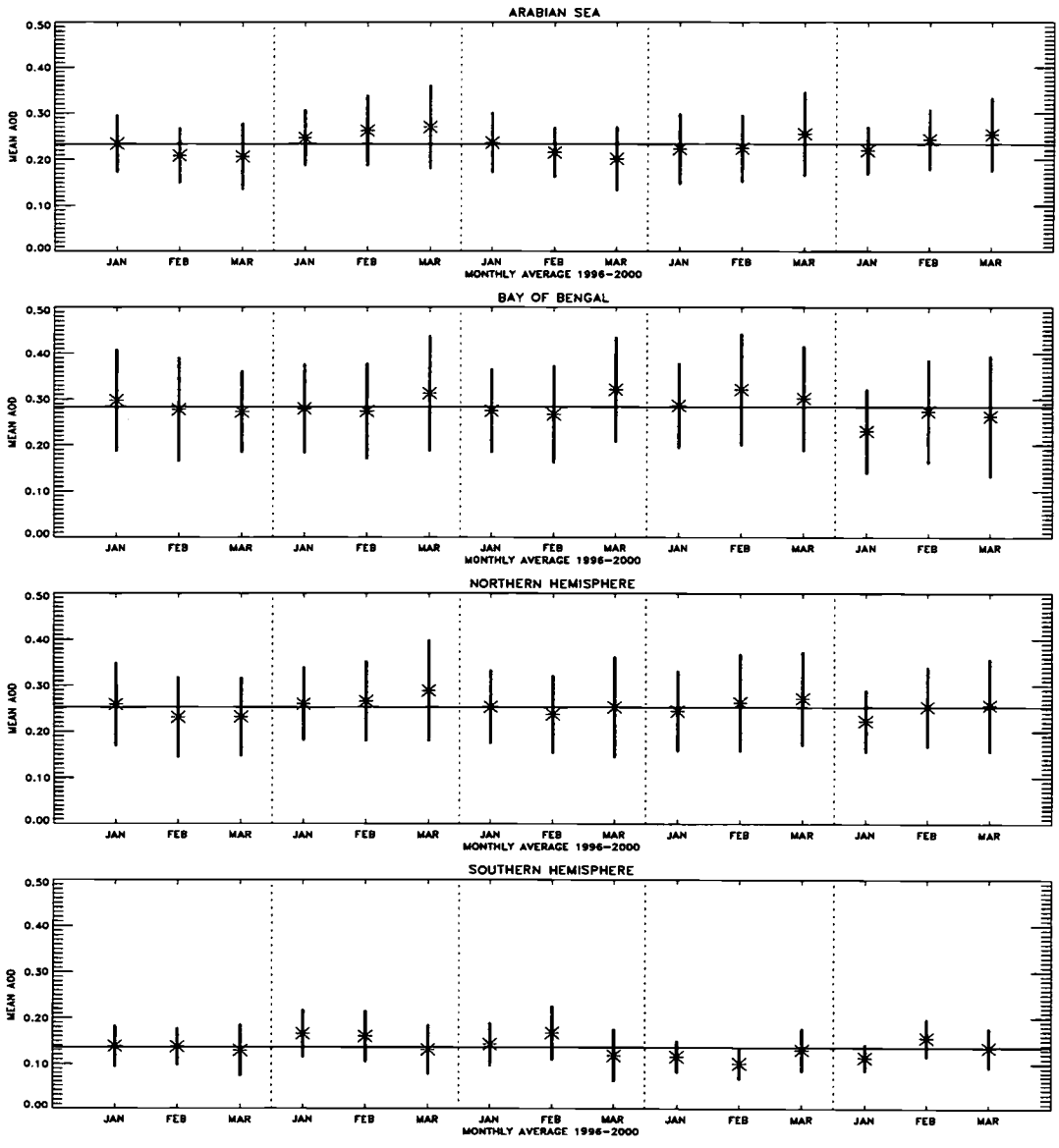

Figure 5.6. Monthly mean 0.55-μm optical depth for January-March 1996-2000 for the specified regions. The bar represents the daily standard deviation about the mean for the region.

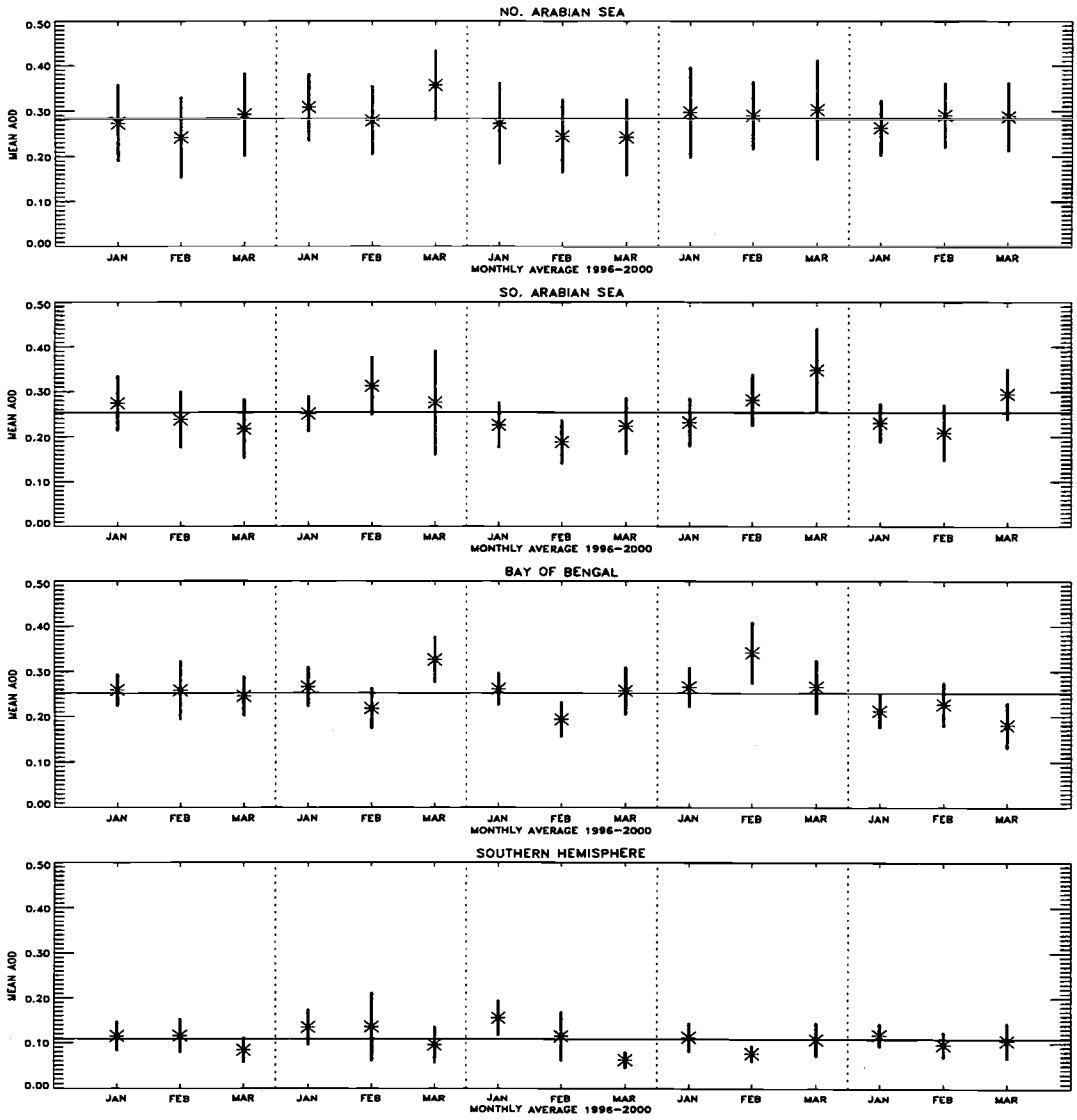

Figure 5.7. Monthly mean 0.55-μm optical depths for January-March 1996-2000 for the specified 10° × 10° latitude-longitude subregions. The bar represents the standard deviation of the daily means for the subregion.

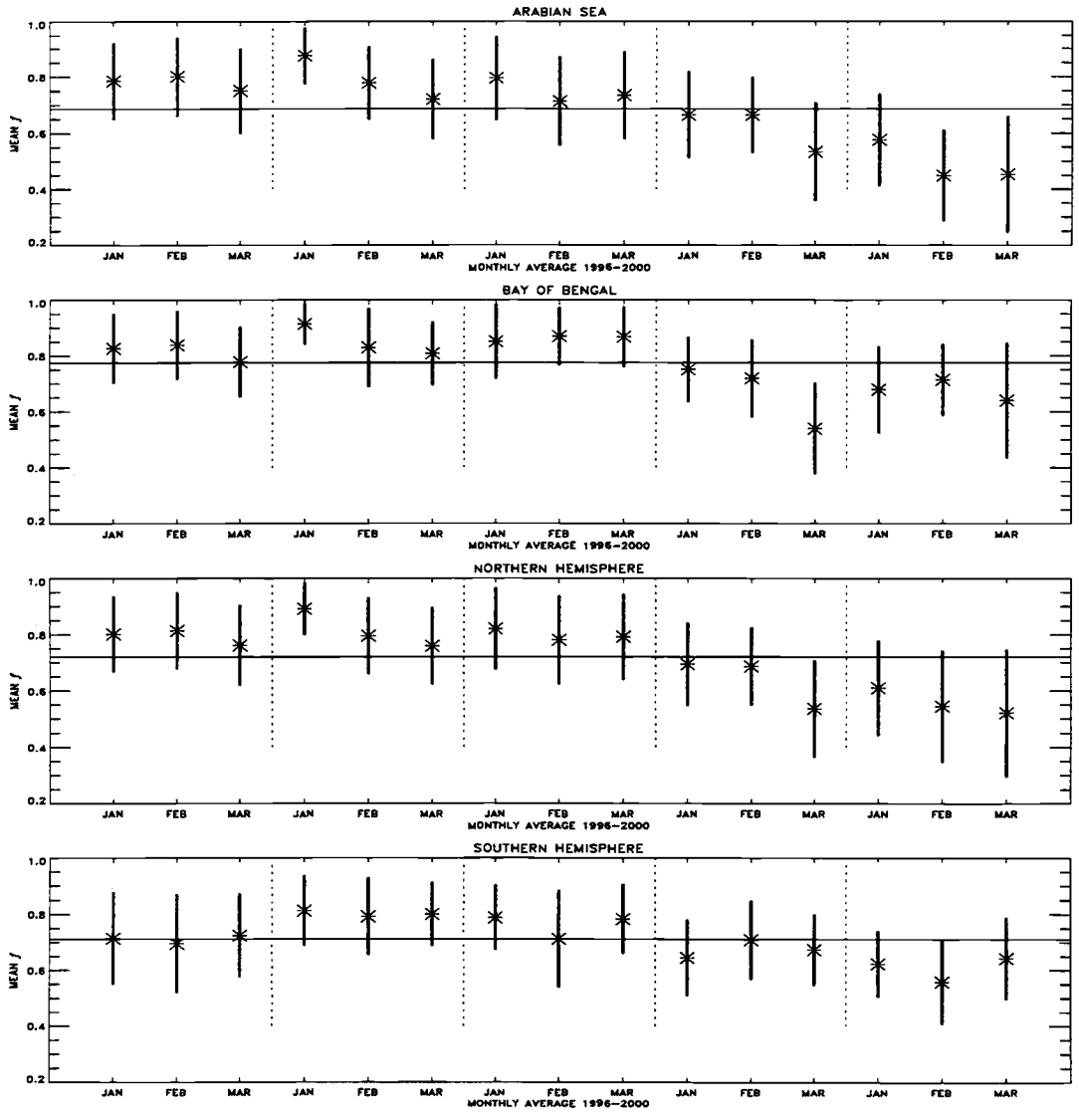

Figure 5.8. Monthly means of the aerosol mixing fraction, *f*, for January-March 1996-2000 for the specified regions. The bar represents the standard deviation of the daily means for the region.

change in the mixing fraction obtained for 2000 might be due either to the drift in orbit of the NOAA-14 satellite toward later equator crossing times, or to changes in the radiometric response of the AVHRR. Because of the later equator crossing time, the solar zenith angles were distinctly higher for 2000 than for the other years. With the higher solar zenith angles, retrievals must be made with lower levels of reflected sunlight, thereby amplifying any errors in calibration and the radiative transfer results. The calibrations for the Channel 1 and Channel 2 reflectances were checked using extensive ice sheets of Greenland and Antarctica. The radiometric response of the NOAA-14 AVHRR for 2000 had undergone a marked change from its behavior in previous years (Tahnk and Coakley 2000b). Once the altered response had been incorporated, retrieved optical depths were compared with those measured at the Kaashidhoo Climate Observatory (KCO), and the comparisons were not noticeably different for 2000 than those obtained for the previous years. Unfortunately, as Coakley et al. (2000) noted, comparisons of retrieved and measured optical depths provide few constraints on the aerosol properties retrieved using AVHRR radiances. Consequently, the source of the trend in f, whether real or due to fundamental errors in the calculated radiances used in the retrievals, or to an error in the calibration of the AVHRR, remains elusive.

5.4 Day-to-Day and Year-to-Year Variability in Optical Depth

The similarity in spatial patterns shown in Fig. 5.4 for the optical depth and its year-to-year standard deviation suggests that the variability of the optical depth for a region is proportional to the long term average optical depth. Figure 5.9 shows the March 1996–2000 average optical depth and the standard deviation of the

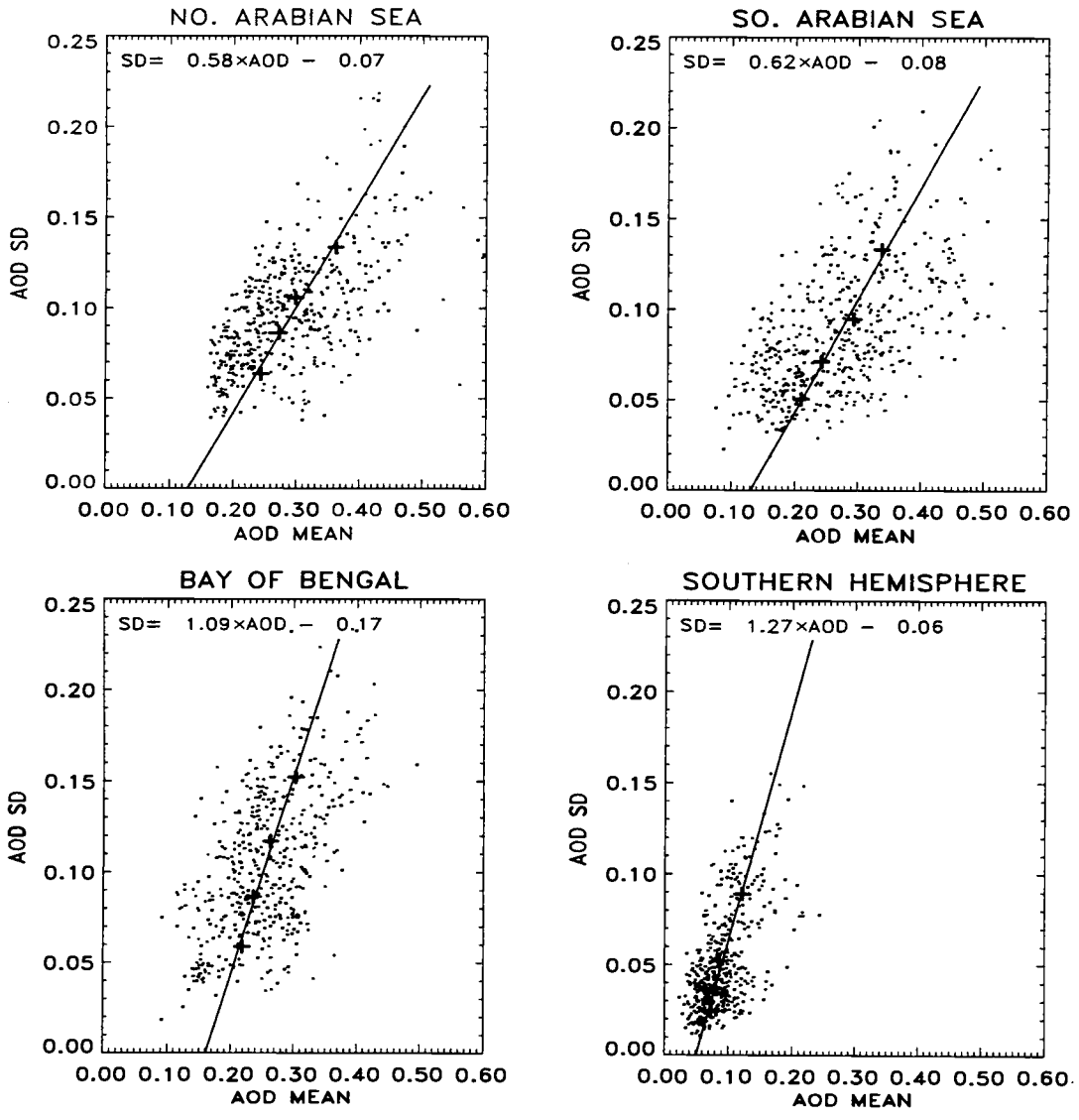

Figure 5.9. Average and day-to-day standard deviation of the 0.55-μm optical depth for March 1996-2000 for the specified 10° × 10° latitude-longitude subregions. The line represents a least squares fit to the averages for each quartile of the monthly mean optical depth.

daily optical depth for the 1° × 1° latitude-longitude boxes that are part of the 10° × 10° latitude-longitude subregions identified in Fig. 5.4. The figure shows linear least-squares fits of the daily standard deviation as a function of the monthly mean optical depth. The fits were obtained by dividing the monthly mean optical depths into quartiles and using the average standard deviation and mean optical depth for each quartile, as indicated by the cross, in the least-squares analysis. As shown in the figure, the standard deviation of the daily optical depth was reasonably well predicted by the monthly mean optical depth. Such behavior is expected of species with short atmospheric residence times. Concentrations of particles build over a period until removed, primarily through scavenging by precipitation. On monthly time scales, regions with heavy aerosol burdens experience a much wider range of aerosol concentrations than do regions with low burdens.

The relationship between the mean and standard deviation of the optical depth is captured by the gamma distribution function. The probability of finding the daily optical depth to be between τ and $\tau + d\tau$ is given by

$$P(\tau) = \frac{1}{\Gamma(\nu)}\left(\frac{\nu}{\bar{\tau}}\right)^{\nu} \tau^{\nu-1} e^{-\nu\tau/\bar{\tau}}, \tag{5.1}$$

where $\bar{\tau}$ is the monthly average optical depth, $\Gamma(\nu)$ is the gamma function, and the standard deviation of the optical depth is given by

$$\sigma = \frac{\bar{\tau}}{\sqrt{\nu}}. \tag{5.2}$$

Figure 5.10 shows the gamma distribution functions obtained for the four subregions. Clearly, the distribution function provides a useful representation for the variability of the daily optical depths for the 1° × 1° latitude-longitude boxes. Note that the distributions in Fig. 5.10 reflect variability of the optical depth in both time and space while those in Fig. 5.9 reflect variability in time only.

The relationship between monthly mean and the standard deviation of the daily optical depths also holds for the 5-year monthly means and the standard deviation of the monthly mean optical depths as shown in Figure 5.11. The figure gives the 5-year mean optical depth for each of the 1° × 1° latitude-longitude boxes of the subregion and the corresponding standard deviation of the 5 monthly means. As with Fig. 5.9, the distributions reflect the variability of the optical depth in time only. Figure 5.12 shows the gamma distribution functions for the four subregions.

The results in Figs. 5.9 and 5.11 indicate that whether affected by pollution or pristine, for the 1° × 1° latitude-longitude scale, the standard deviations of the monthly means were practically identical to the standard deviations of the daily means. The relatively large ratio of the monthly to daily variability in optical depths results from the short atmospheric residence times of the particles coupled with the episodic character of the sources and sinks that allow burdens to rise to large values. The results in Figs. 5.10 and 5.12, on the other hand, indicate that while for polluted regions the standard deviation associated with the spatial distribution is somewhat smaller for the monthly than for the daily means, the spatial structure for pristine regions is considerably smaller for the monthly means, as would be expected for species with short residence times.

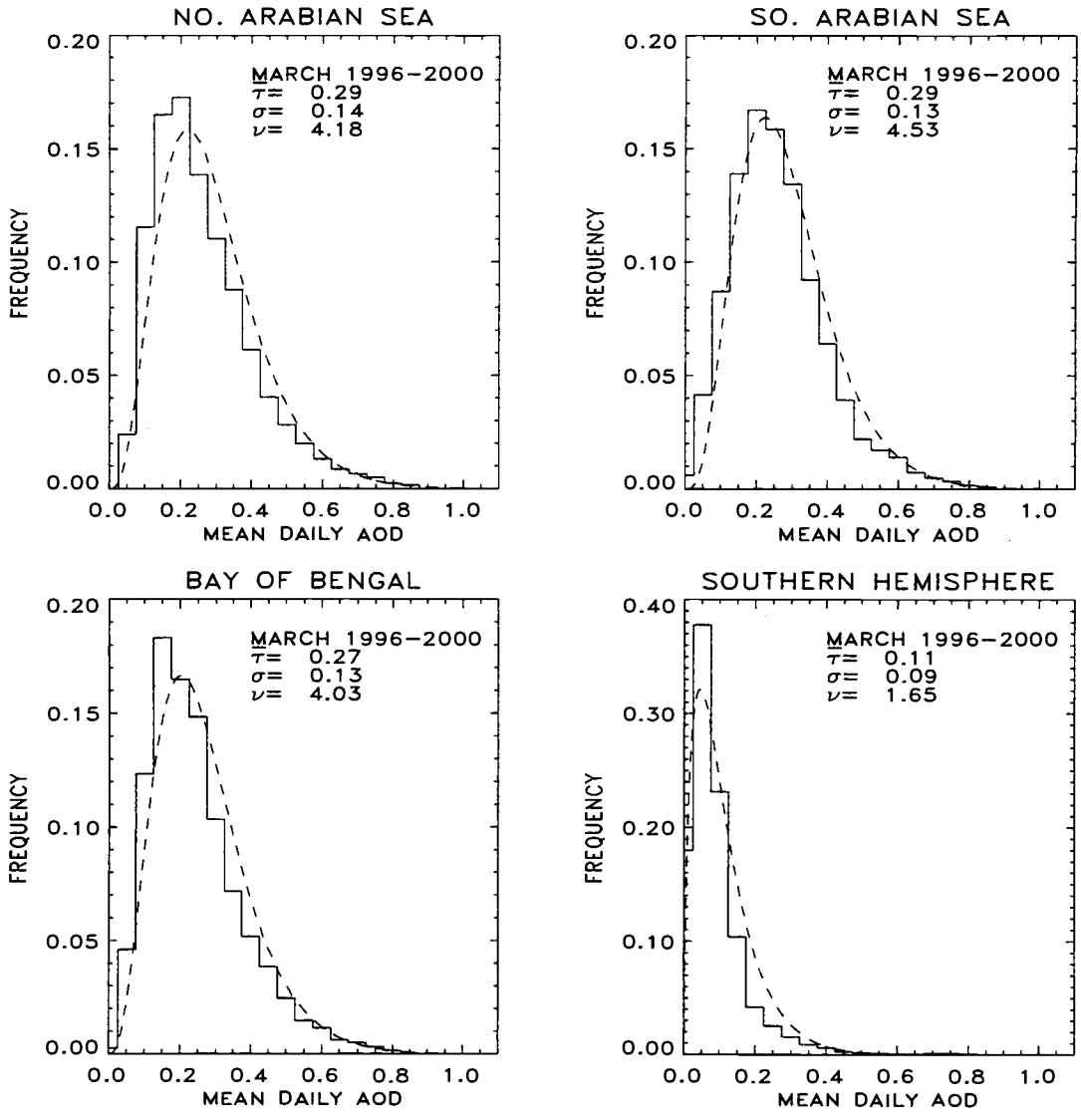

Figure 5.10. Frequencies of the daily 0.55-μm optical depths for 1° × 1° latitude-longitude boxes within the specified 10° × 10° latitude-longitude subregion. The observations are for March 1996-2000. The dashed line is the gamma distribution function fit to the observations.

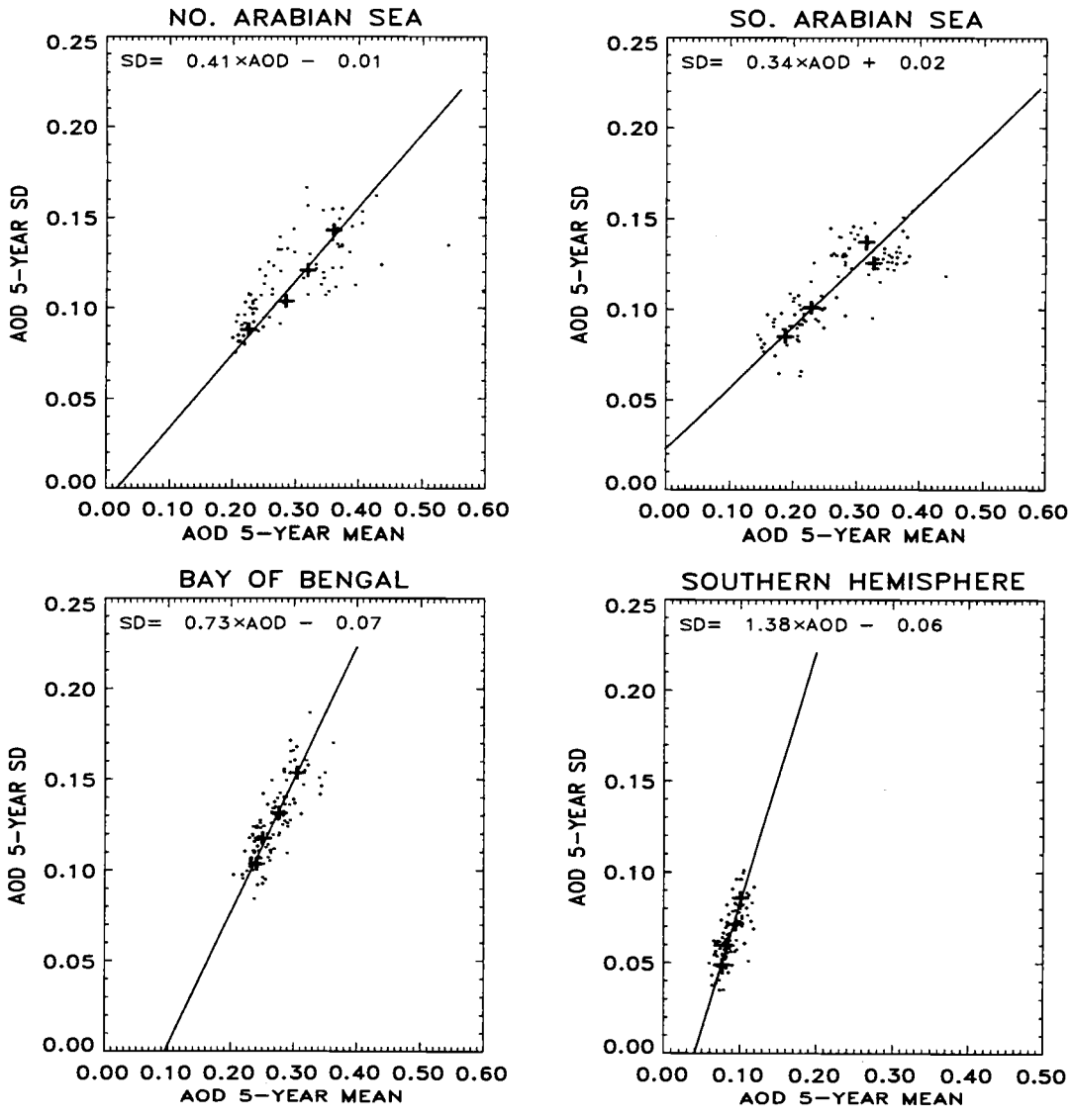

Figure 5.11. Same as Fig. 5.9 but averages of March for 5 years and year-to-year standard deviations.

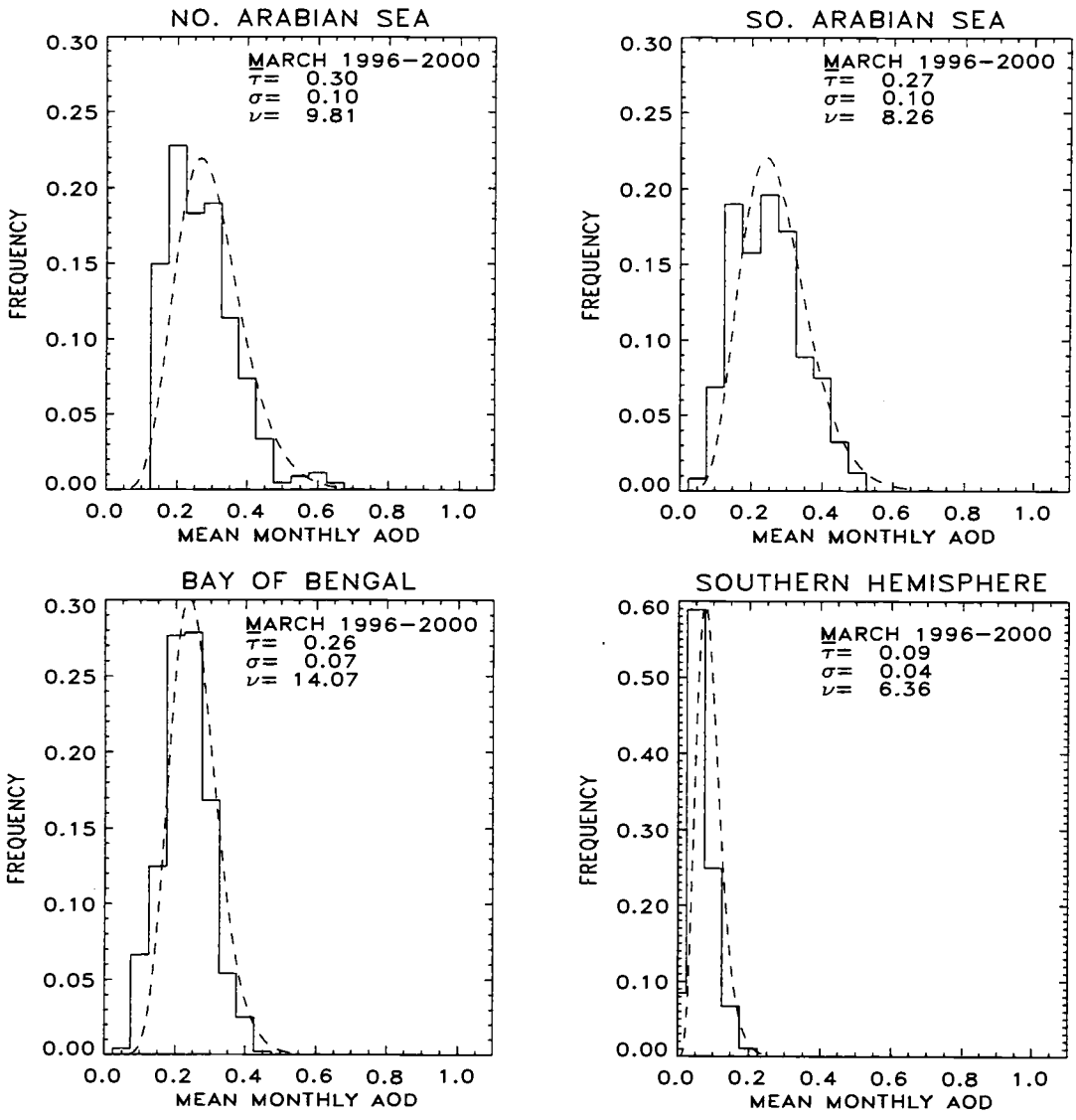

Figure 5.12. Same as Fig. 5.10 but for the monthly means.

As noted in the Introduction, in recent years models have been developed to estimate concentrations of various aerosols. In assessing model performance, averages of station data for the chemical components of aerosols are compared with concentrations of the components produced by the models. Since for the $1° \times 1°$ latitude-longitude scale, the monthly mean optical depths appear to be as variable as the daily means, short-term station data is of little use in establishing trends on either seasonal or regional scales. Records of many years appear to be required to establish the trends.

5.5 Aerosol Radiative Forcing

Figures 5.13-5.15 show the yearly seasonal average and Figure 5.16 the 5-year seasonal average aerosol direct radiative forcing at the top of the atmosphere, the surface, and in the atmosphere for cloud-free conditions. Figures 5.17-5.19 show the yearly seasonal average and Figure 5.20 shows the 5-year seasonal average aerosol direct radiative forcing for average cloud conditions. As mentioned in Section 5.2, the radiative forcing is the diurnally averaged estimate derived by taking the aerosol mixture, optical depth, and cloud conditions retrieved at the time of the NOAA-14 daytime overpass to be constant for the daylight hours. As with the optical depth, perturbations to the radiation budget by the aerosol are clearly evident in the Northern Hemisphere when comparisons are made with the Southern Hemisphere. The perturbation to the radiation budget of the northern Indian Ocean due to the aerosol direct radiative forcing is -2 Wm^{-2} for most of the Northern Hemisphere, with -6 Wm^{-2} near pollution sources. The surface forcing is typically more than twice the top of the atmosphere forcing. The higher surface forcing is due to the absorption of sunlight by the aerosol.

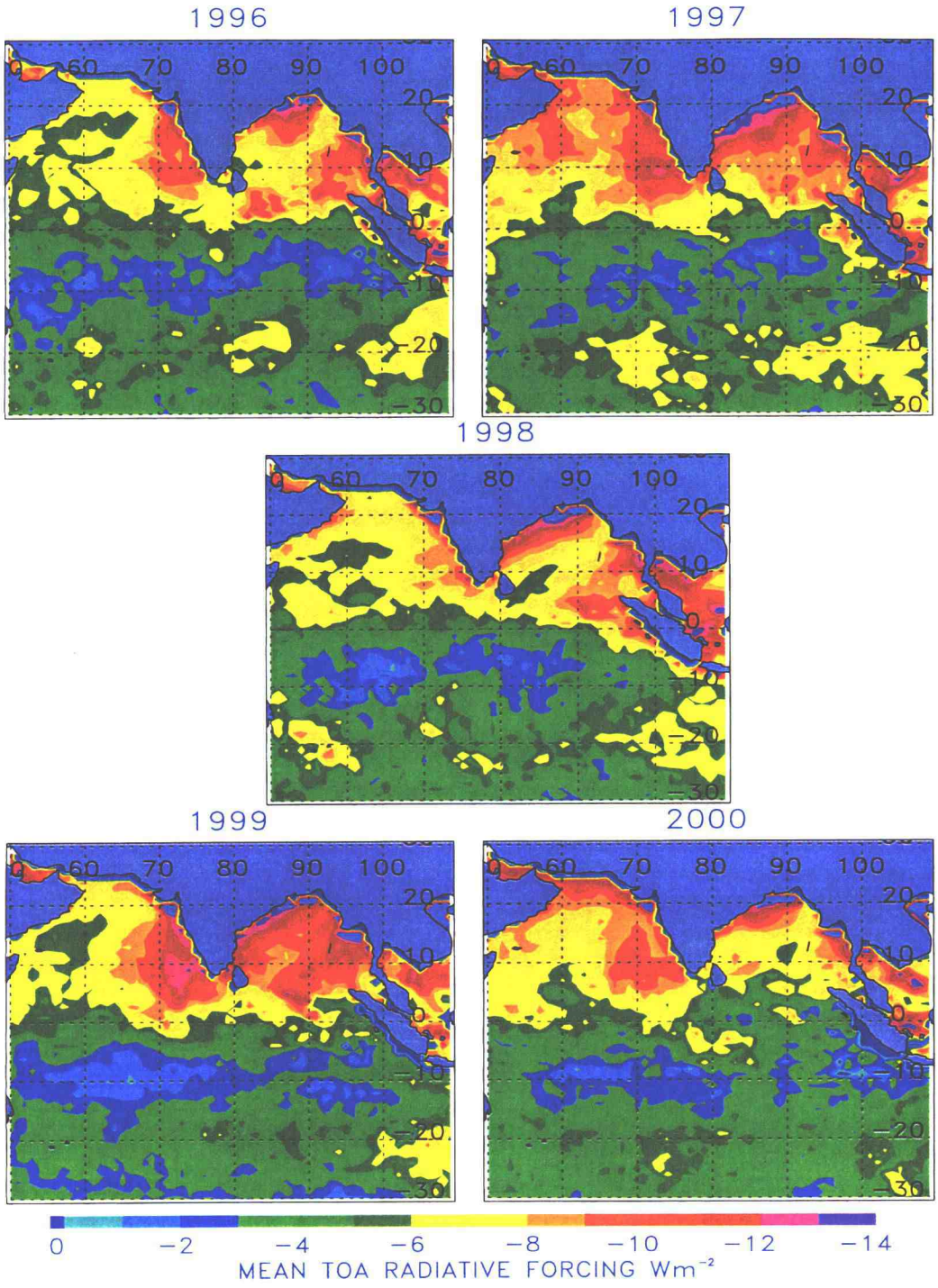

Figure 5.13. Seasonally averaged aerosol direct radiative forcing for 1996-2000 for top of the atmosphere and cloud-free conditions.

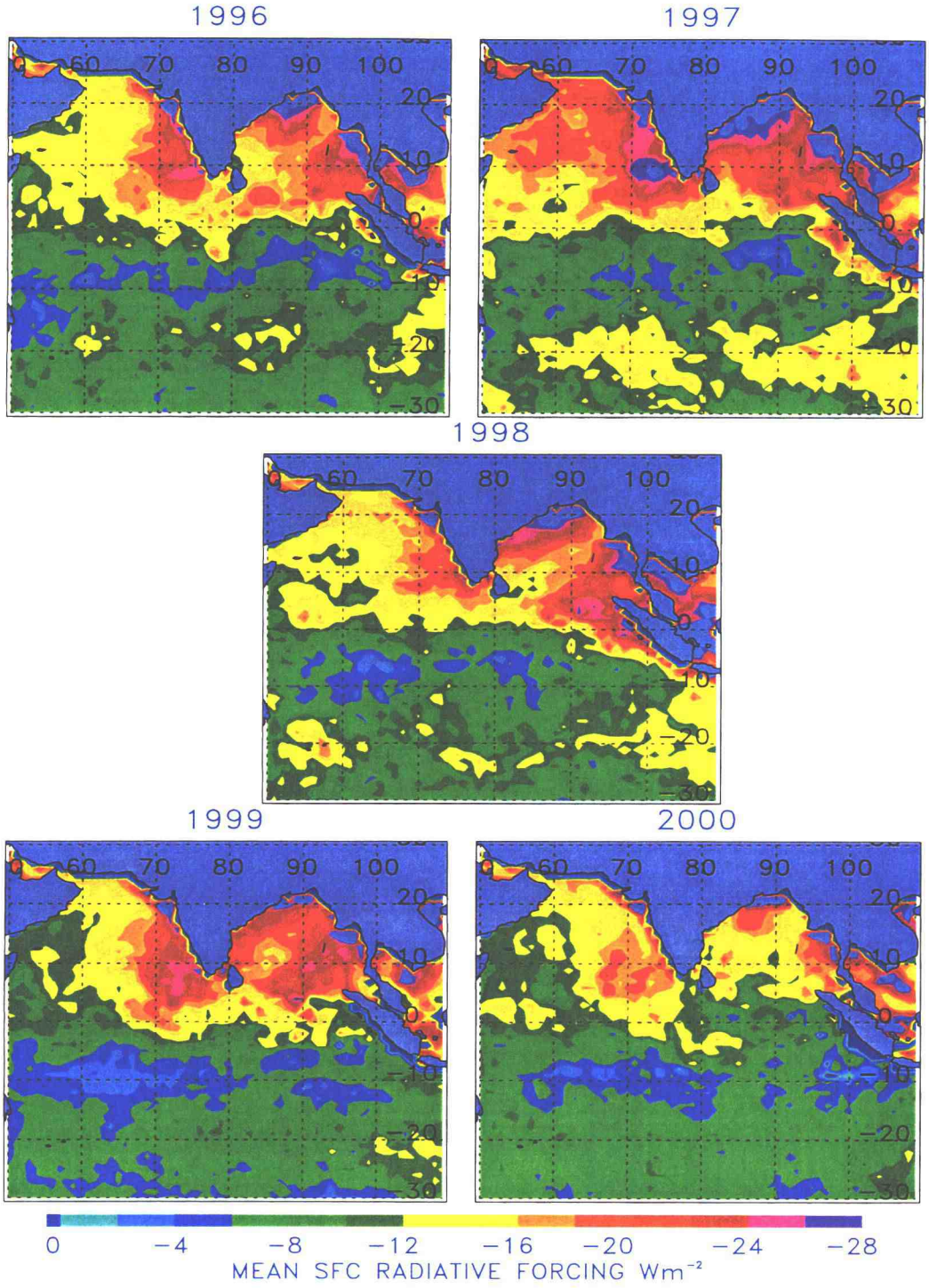

Figure 5.14. Seasonally averaged aerosol direct radiative forcing for 1996-2000 for the surface and cloud-free conditions.

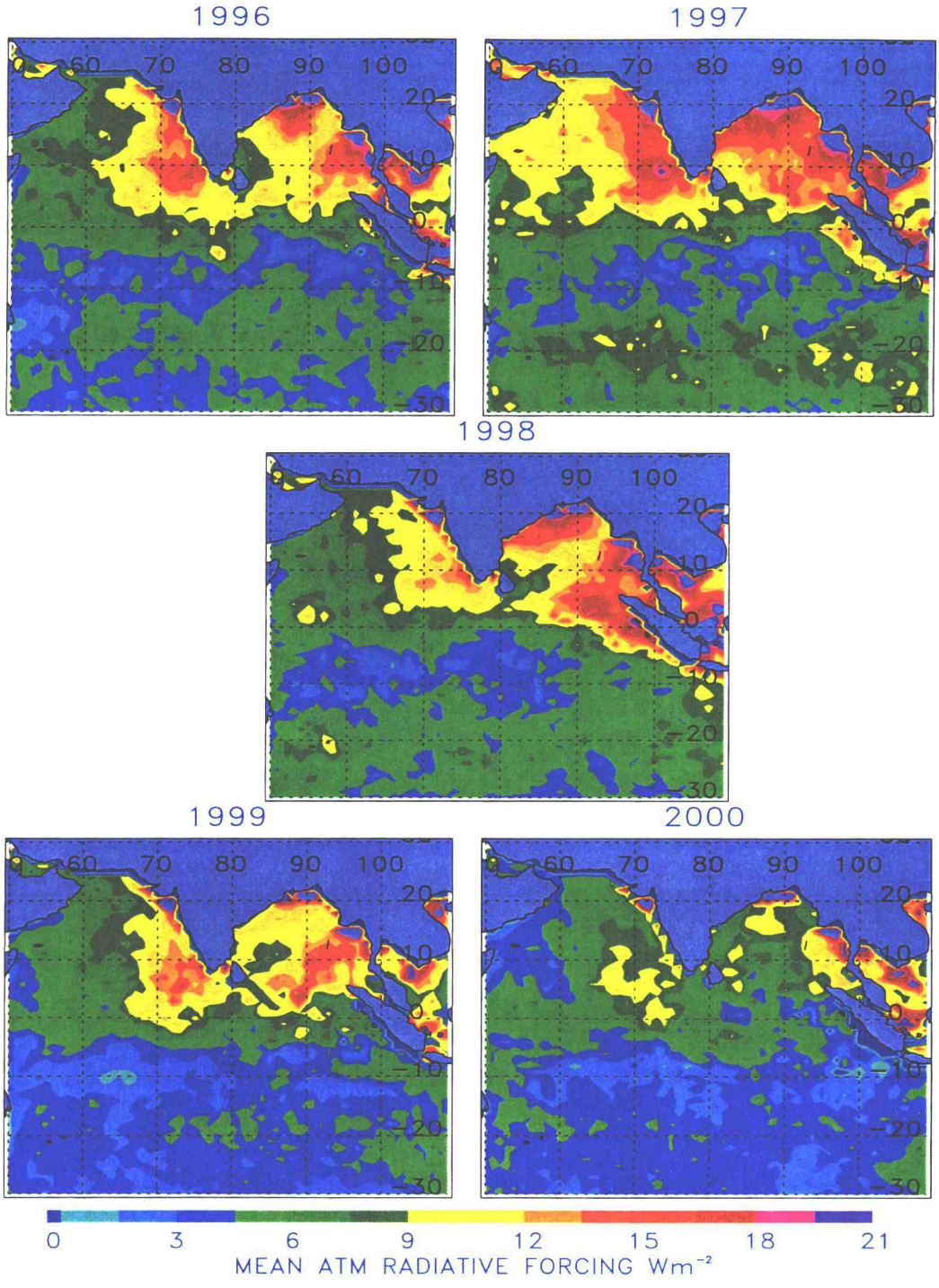

Figure 5.15. Seasonally averaged aerosol direct radiative forcing for 1996-2000 for the atmosphere and cloud-free conditions.

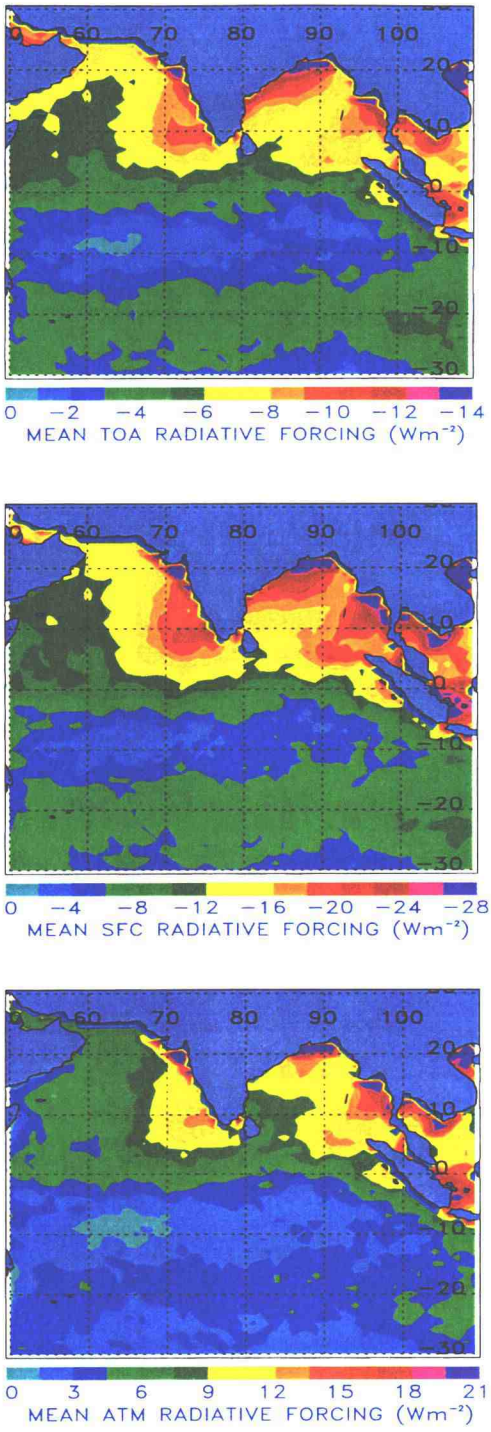

Figure 5.16. 5-year seasonal average aerosol direct radiative forcing for top of the atmosphere, surface, and atmosphere, for cloud-free conditions.

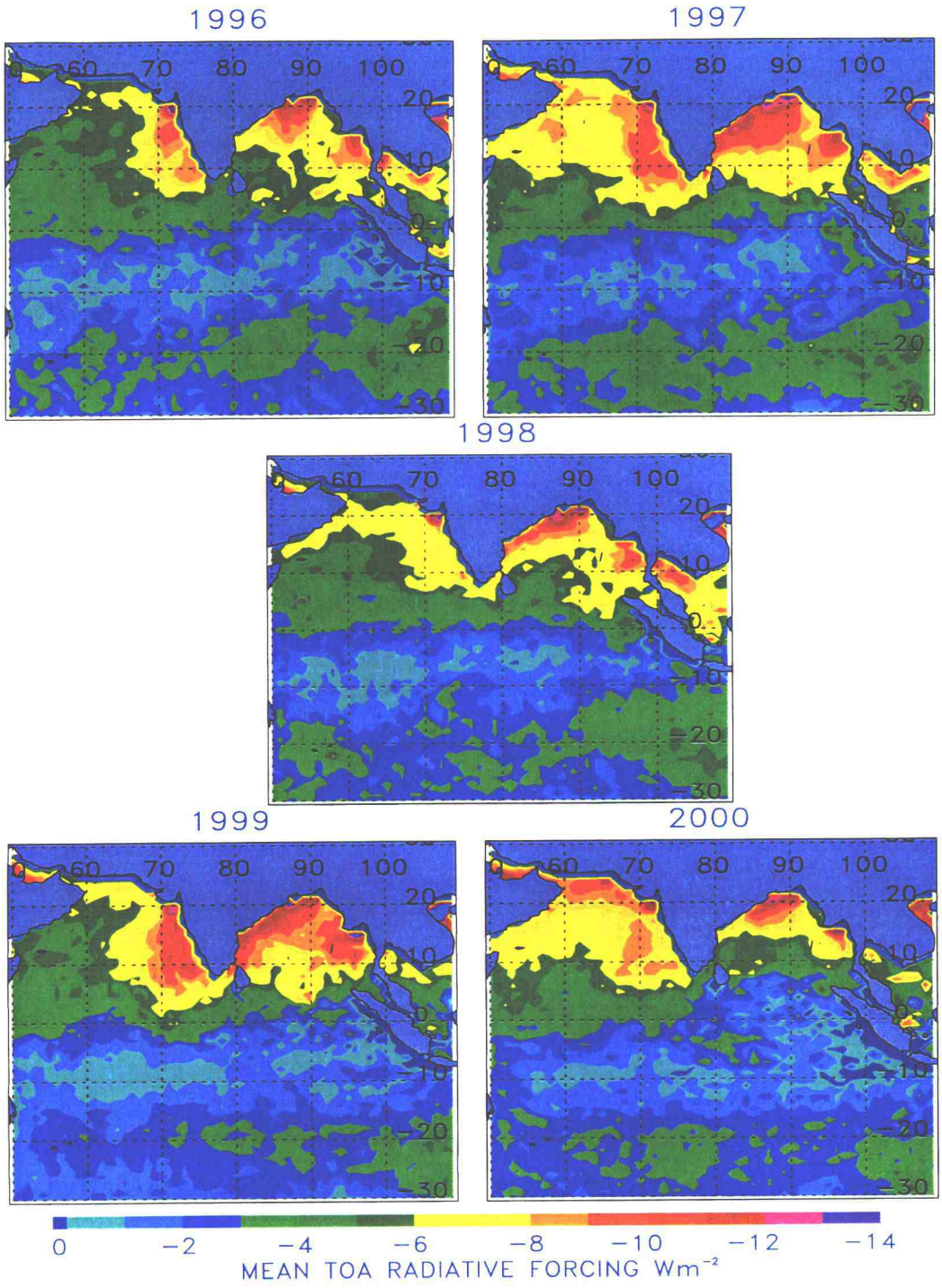

Figure 5.17. Seasonally averaged aerosol direct radiative forcing for 1996-2000 for top of the atmosphere and average cloud conditions.

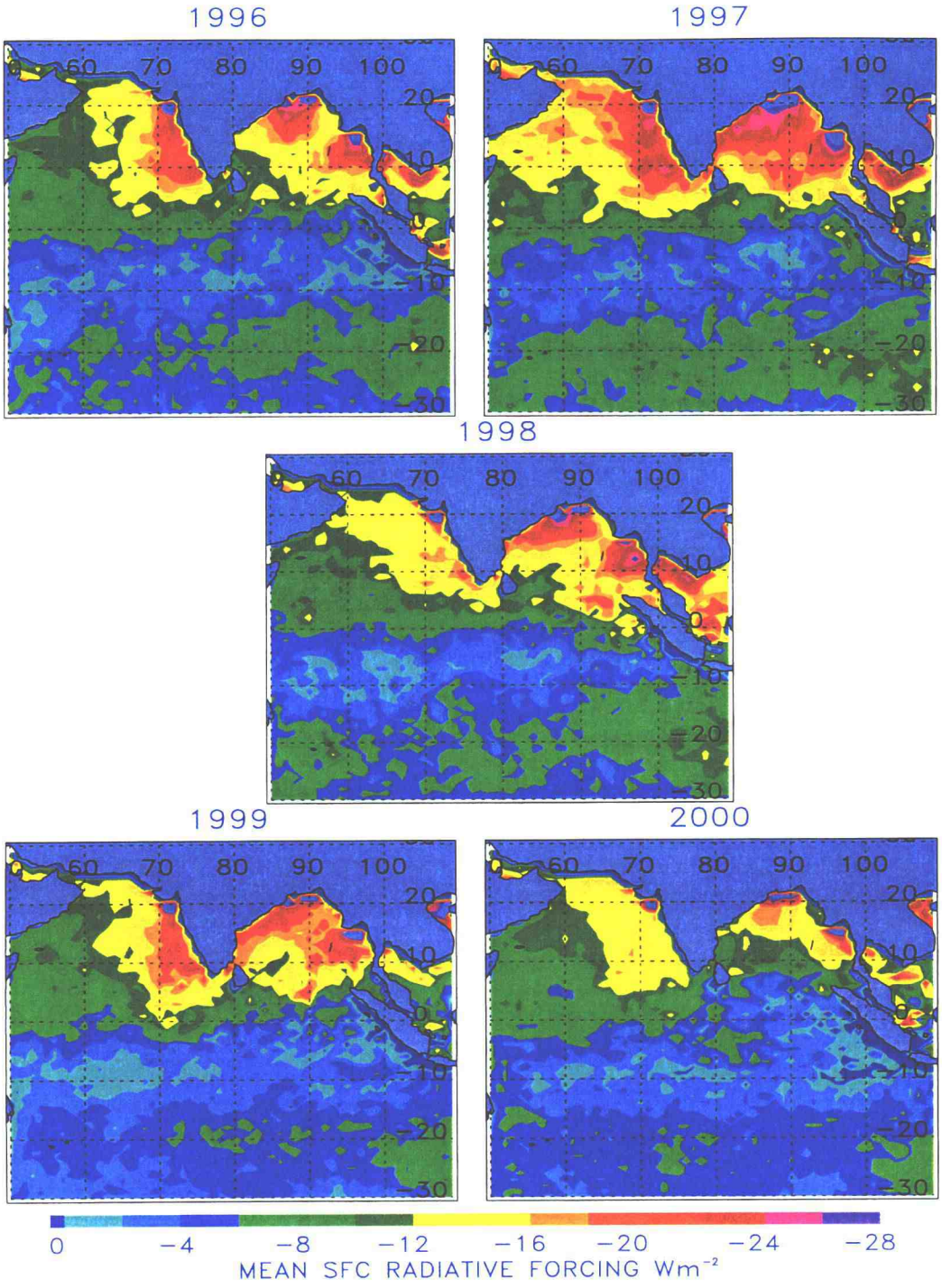

Figure 5.18. Seasonally averaged aerosol direct radiative forcing for 1996-2000 for the surface and average cloud conditions.

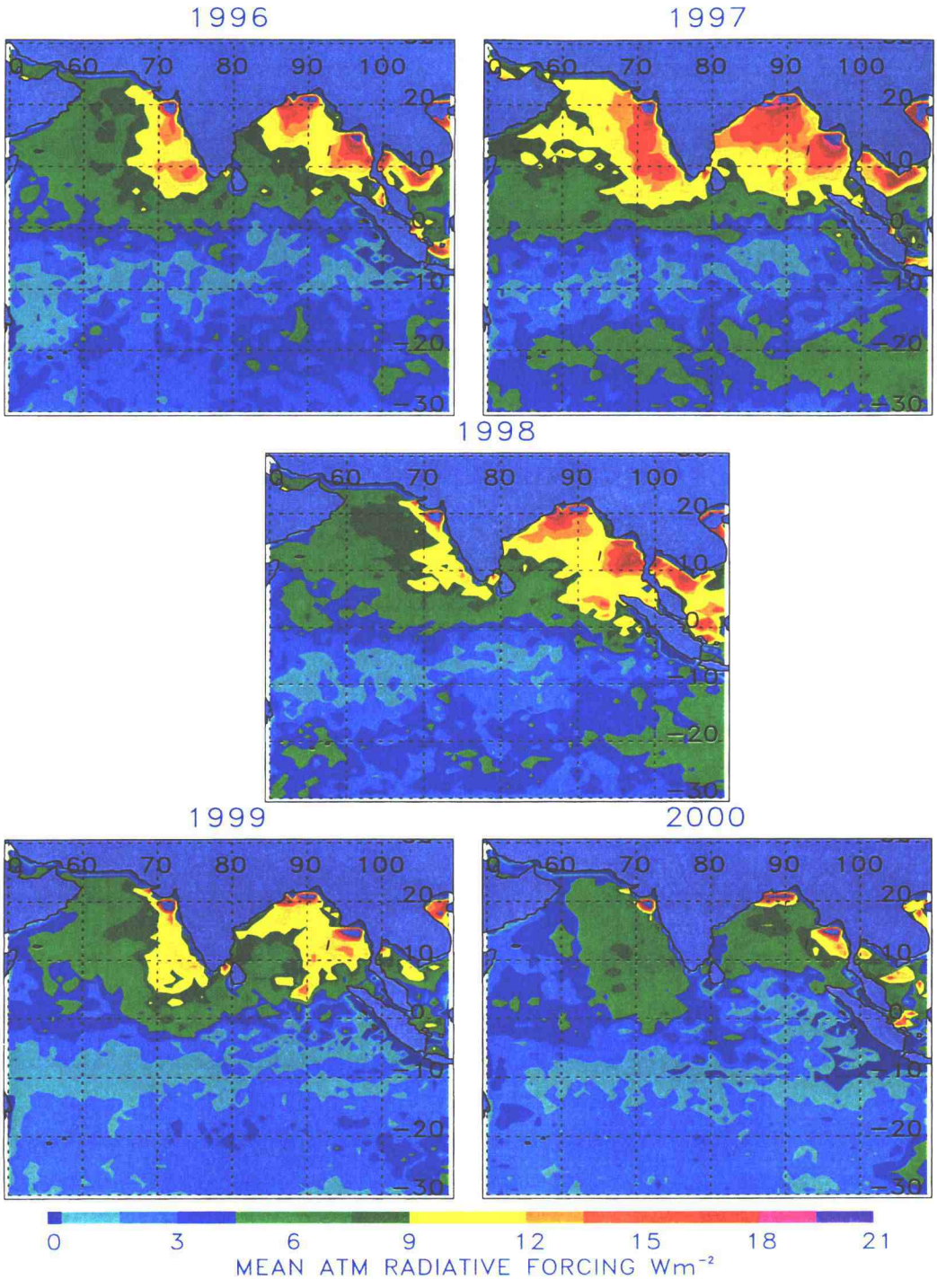

Figure 5.19. Seasonally averaged aerosol direct radiative forcing for 1996-2000 for the atmosphere and average cloud conditions.

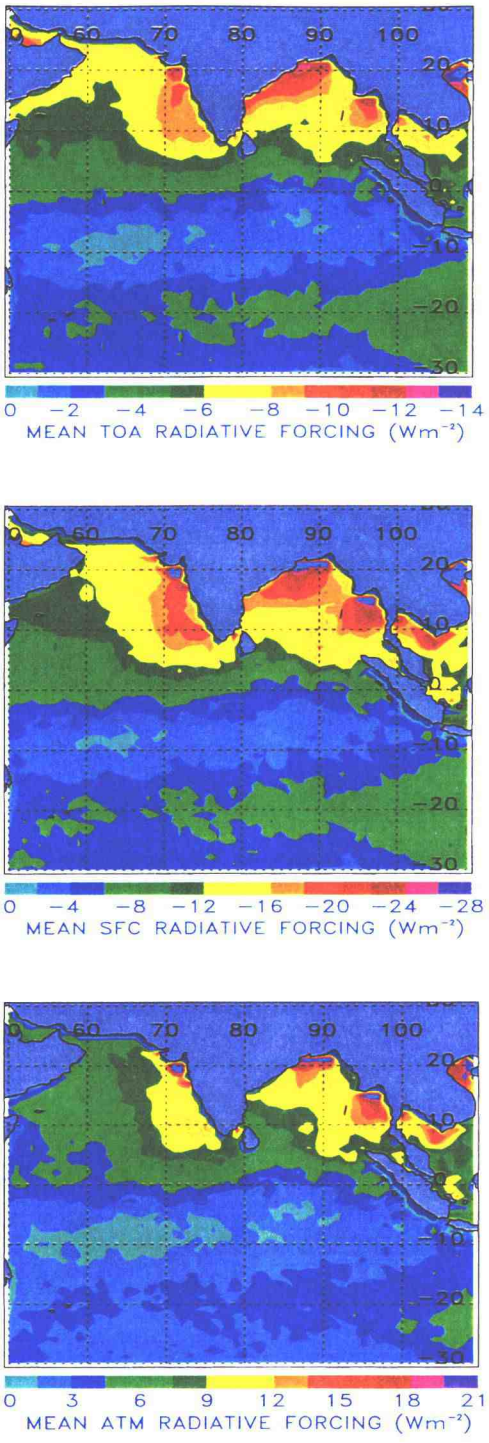

Figure 5.20. Same as Fig. 5.16 but for average cloud conditions.

Clearly, the aerosol direct radiative forcing is related to the optical depth. The sensitivity of the forcing to optical depth is presented for the 10° × 10° latitude-longitude subregions in Figure 5.21 for cloud-free conditions and in Figure 5.22 for average cloud conditions. Each point in Figs. 5.21 and 5.22 is contributed by one of the 1° × 1° latitude-longitude boxes for one of the five years included in the study. Linear, least-squares fits constrained to pass through the origin were used to determine the sensitivity of the fluxes to the optical depth. For cloud-free conditions, the departures of the points from a strict, linear relationship with optical depth is the result of using the 2-channel, 2-aerosol model retrieval scheme. The departures are particularly noticeable for the surface and atmospheric forcing. Use of a single aerosol model as done, for example, by Rajeev et al. (2000) would have led to strictly linear relationships for the range of optical depths observed.

Despite the use of the 2-channel, 2-model scheme, the sensitivity of the radiative forcing to optical depth is nearly identical for the four subregions. As indicated by the results in Table 1, the 0.64 and 0.84-μm reflectances did not place the absorbing average continental aerosol with its relatively small particles in the polluted regions and the nonabsorbing tropical marine aerosol with its relatively large particles in the pristine regions. Based on these retrievals, there is little difference between the aerosols and consequently little difference in the relationship between the top of the atmosphere direct radiative forcing for cloud-free conditions and the optical depths. For the four subregions under cloud-free conditions, the top of the atmosphere radiative forcing ranges from –30 to –33 Wm^{-2} per unit 0.55-μm optical depth; the surface forcing ranges from –64 to –71 Wm^{-2}, and the atmospheric forcing ranges from 32 to 38 Wm^{-2}. The sensitivity of the atmospheric forcing to optical depth in the Southern Hemisphere is expected to be close to zero. As was noted by Coakley et al. (2000), the retrieval scheme used here failed to produce such a result. Satheesh and Ramanathan (2000) obtained –25 Wm^{-2} per unit 0.5-μm optical depth for the sensitivity of the top of the atmosphere cloud-free aerosol direct radiative forcing to optical depth and –70

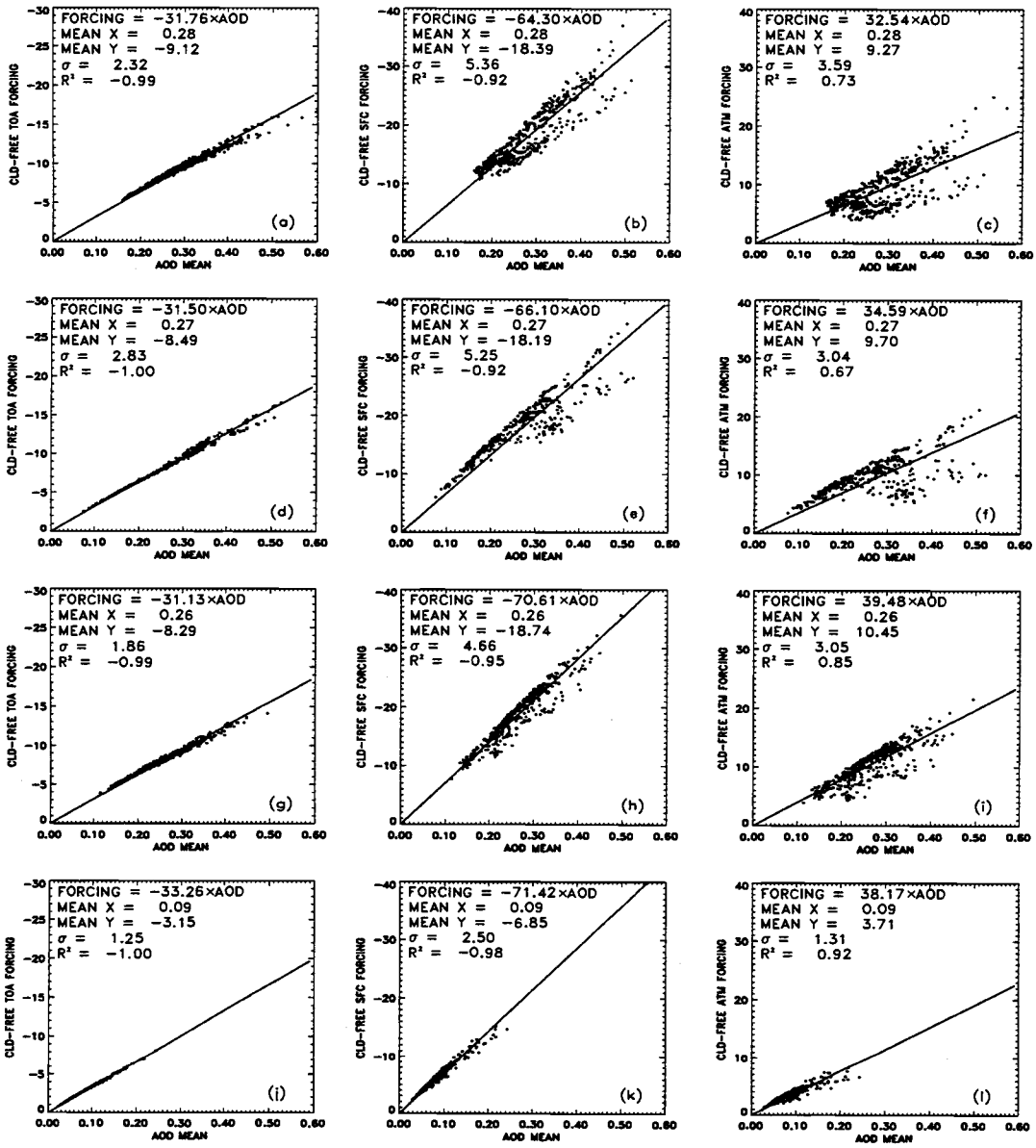

Figure 5.21. Aerosol direct radiative forcing and optical depth for cloud-free conditions and the following 10° × 10° latitude-longitude subregions: (a)-(c) No. Arabian Sea; (d)-(f) So. Arabian Sea; (g)-(i) Bay of Bengal; and (j)-(l) Southern Hemisphere. The line represents a linear least squares fit passing through the origin.

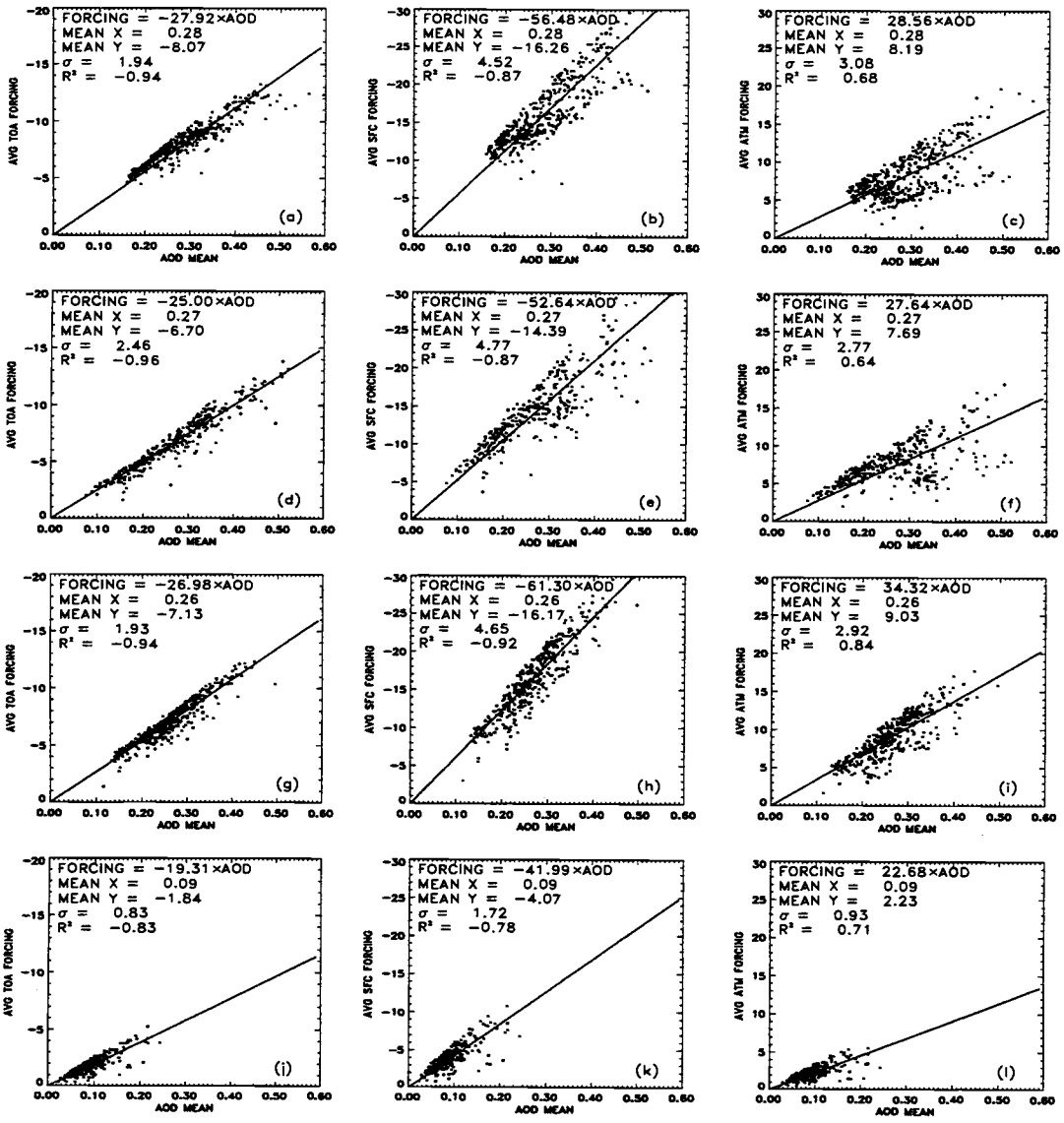

Figure 5.22. Same as Fig. 5.21 but for average cloud conditions.

Wm^{-2} per unit 0.5-μm optical depth for the surface forcing. They based their estimates on surface measurements of the optical depth and surface radiative fluxes at KCO and top of the atmosphere radiative fluxes obtained by the Cloud and Earth's Radiant Energy System on the Tropical Rain Measurement Mission satellite. The results obtained here give larger magnitudes (25%) for the top of the atmosphere forcing and generally smaller magnitudes (10%) for the surface forcing.

The magnitude of the aerosol direct radiative forcing under average cloud conditions is, of course, less than the magnitude for cloud-free conditions. The 10° × 10° latitude-longitude subregions of the Northern Hemisphere were remarkably devoid of cloud cover during the winter monsoon, and as a result, clouds reduced the sensitivity of the forcing by only about 15% in these subregions. Cloud cover was more extensive in the subregion of the Southern Hemisphere and the sensitivity of the top of the atmosphere forcing to optical depth was reduced by 40% there.

Because of the nearly linear relationship between radiative forcing and optical depth, day-to-day and year-to-year variability in the forcing is given by the product of the sensitivity of the forcing to optical depth and the variability of the optical depth. For example, the year-to-year variability of the seasonal mean 0.55-μm optical depth in the Bay of Bengal is 0.07 (Fig. 5.12), the year-to-year variability in the top of the atmosphere forcing is $0.07 \times -27\ Wm^{-2} = -2\ Wm^{-2}$, $-4\ Wm^{-2}$ at the surface, and $2\ Wm^{-2}$ in the atmosphere.

Chapter 6
Concluding Remarks: Summary and Future Work

6.1 Summary

6.1.1 Introduction

The Indian Ocean Experiment (INDOEX) was a focused field experiment designed to achieve a better understanding of the role of aerosols, clouds, and tropospheric chemistry and transport, in climate forcing and change (Ramanathan et. al., 1996). A specific objective of INDOEX was the determination of the aerosol radiative forcing for the Indian Ocean during the January-March winter monsoon. Estimates of aerosol burdens and the consequent radiative forcing derived from satellite imagery data were the primary means for achieving this objective, and the Advanced Very High Resolution Radiometer (AVHRR) on the NOAA-14 satellite was a major source of observations. This study used NOAA-14 observations from the INDOEX region to derive a five-year seasonal climatology of aerosol burden and assess the magnitude and distribution of radiative forcing and its impact on climate.

6.1.2 NOAA-14 AVHRR Calibration

Analyses of cloud-free NOAA-14 channel 1 and 2 reflectances for the permanent ice sheets of Antarctica and Greenland were conducted in order to evaluate the accuracy of published calibration coefficients. Based on data from January 1996-2000 for

Antarctica and May and June 1995-2000 for Greenland, it is apparent that the published formulae for calibrating reflectances from the NOAA-14 AVHRR visible and near-IR bands overcompensate for sensor degradation. Consequently, revised sets of calibration coefficients were developed. The Antarctic data were reprocessed, using the revised calibration formulae and exhibited stable reflectances for the 5-year period of this study. The derived calibration formulae were used to obtain reflectances for stable targets over Greenland and the formulae proved to adequately account for sensor degradation. The improved calibration coefficients were used to derive NOAA-14 AVHRR channel 1 and 2 reflectances in the INDOEX region for the period of this study.

6.1.3 Retrieval of Aerosol Optical Depth and Radiative Forcing: Theory

A new aerosol retrieval scheme was developed to take advantage of both the visible and near infrared reflectances measured by the AVHRR. In the scheme, reflected sunlight is taken to be a composite of the components contributed by two distinctly different aerosol types. The types chosen for this investigation were the average continental and tropical marine aerosol models described by Hess et al. (1998). The models were chosen in part because they represented the polluted continental haze and the marine aerosols that were expected to be found in the INDOEX region and in part because reflectances calculated for cloud-free ocean scenes with these aerosol types occupied the largest portion of the visible and near infrared reflectance domain spanned by any combination of realistic aerosol types (Fig. 4.1). The fraction of the aerosol component contributing to the observed reflectance was determined from the slope of the departures in the near infrared and visible reflectances from their cloud-free and aerosol-free values for ocean scenes. The optical depth of the mixed aerosol was then derived from the departure of the reflectances from their cloud-free and aerosol-free values. For comparison, optical depths were also retrieved using a variety of aerosol models: the INDOEX FFP model described by Rajeev et al. (2000), the NOAA Phase 1

and Phase 2 models described by Stowe et al. (1997), and the average continental and tropical marine aerosols taken separately in the commonly used single-channel, single-aerosol model retrieval (Stowe et al. 1997; Rajeev et al., 2000) as well as in a two-channel variant of the single-aerosol model retrieval.

Optical depths retrieved at visible and near infrared wavelengths were compared with collocated surface measurements. Except for the NOAA Phase 1 model, the comparisons indicated that there was little reason to choose one retrieval scheme or one aerosol model over the other. Biases in the 0.65-μm optical depths were typically less than 0.05 and RMS differences about the bias were typically less than 0.06. Such values are comparable to the bias expected for cloud contamination in the fields of view used to retrieve aerosol properties.

Estimates of the top of the atmosphere and surface aerosol direct radiative forcing were made using the retrieved optical depth and aerosol component mixing fraction in radiative transfer calculations of the shortwave fluxes. For the top of the atmosphere forcing under cloud-free conditions, the derived forcing was relatively insensitive to the choice of aerosol model and retrieval scheme used to derive the aerosol properties. For example, even though optical depths retrieved using the NOAA Phase 1 model differed by almost a factor of two from those obtained with the FFP model, the estimates of the top of the atmosphere radiative forcing differed by only 40%.

Satheesh and Ramanathan (2000) obtained empirical estimates for the sensitivity of the top of the atmosphere and surface solar radiative fluxes for cloud-free conditions at KCO. For the top of the atmosphere cloud-free forcing, the results in Fig. 4.9 and Table 4.3 suggest that the FFP model underestimates the sensitivity of the radiative forcing by less than 15% while the 2-model, 2-channel retrieval scheme overestimates the radiative forcing by 30% when compared with the value given by Satheesh and Ramanathan. The 2-model, 2-channel retrieval scheme underestimates the surface forcing by less than 20% while the FFP model overestimates the forcing by 30% compared with the empirical value.

Extreme estimates were offered for the aerosol direct radiative forcing under average cloud conditions. For the lower estimate, "Average Low," the forcing was set to zero in $1° \times 1°$ latitude-longitude regions that contained upper-level clouds. For the

upper estimate, "Average High," the forcing for regions that contained upper-level clouds was set to the average forcing obtained when no upper-level clouds were present. The upper and lower estimates differed by as much as 60% in the top of the atmosphere and by a factor of two in the surface aerosol direct radiative forcing. By setting the forcing to zero for all $1° \times 1°$ latitude-longitude regions that contained upper-level clouds and all portions of the regions overcast by low-level clouds, "Average-Zero, All Clouds," the resulting top of the atmosphere forcing was almost identical to that obtained by the "Average Low" estimate. Because all but very thick clouds fail to completely attenuate the effect of the aerosols on the solar radiative flux at the surface, the magnitude of the forcing estimated here is likely to be too low, especially for the "Average-Zero, All Clouds" estimate.

6.1.4 Retrieval of Aerosol Optical Depth and Radiative Forcing: Results

Aerosol optical depths and the relative concentrations of aerosol type, continental or marine, were retrieved for the INDOEX region using 5 years of NOAA-14 observations covering the winter monsoons, January–March, 1996-2000. The optical depths and relative concentrations coupled with the optical properties of the aerosol models used in the retrievals were employed to derive estimates of the diurnally averaged, cloud-free aerosol radiative forcing for $1° \times 1°$ latitude-longitude boxes. The effect of clouds on the aerosol direct radiative forcing was estimated by setting the forcing to zero for all regions that contained upper-level cloud and for all portions of regions overcast by low-level clouds. For the monthly mean aerosol direct radiative forcing under average cloud conditions, the estimates for forcing were expected to be within 60% of those obtained by alternate extreme estimates that result from different approximations for the effects of clouds (Coakley et al. 2000). Because only opaque clouds completely attenuate the effect of the aerosols on the surface solar radiative flux, the approximation used here

leads to magnitudes of the surface radiative forcing that are too small, but are probably within 50% of the actual forcing.

For the Arabian Sea, Bay of Bengal, and the Indian Ocean in the Southern Hemisphere, the optical depths were remarkably constant over the five year period (Fig. 5.6). For subregions, such as the southeastern portion of the Arabian Sea and the subregion of the Bay of Bengal, the optical depths retrieved for the IFP were substantially larger than those encountered during the 1998 INDOEX First Field Phase. Differences in optical depths between the polluted Northern Hemisphere and the relatively pristine Southern Hemisphere indicated that the 0.55-μm aerosol optical depth in the Northern Hemisphere was about 0.08 larger as a result of the pollution. In some regions, the seasonal mean aerosol optical depth climbed to 0.2–0.3, depending on the proximity of the pollution sources.

Despite the use of a mixture of aerosols, the continental model with relatively small absorbing particles, and a maritime model with relatively large, nonabsorbing particles, and the reflected sunlight at visible (AVHRR Channel 1) and near infrared (AVHRR Channel 2) wavelengths to deduce the relative concentrations of the aerosol components and associated optical depths, the derived radiative forcing was found to be almost linearly related to the retrieved optical depth. The relative concentrations of the two aerosols were approximately the same for all regions, and with the exception of the later years (1999 and 2000), were the same for all periods. In later years the relative concentrations shifted toward more maritime conditions. While this shift may have been caused by errors in calibration or errors in the retrievals that were amplified by the shift in the NOAA-14 orbit to later equator crossing times, no evidence for such errors could be found in comparisons of the retrieved optical depths with optical depths measured by surface instruments. Because of the constant mixing fraction, the link between optical depth and the direct radiative forcing also remained constant at levels that were within 20% of those deduced empirically by Satheesh and Ramanathan (2000). As a result of the aerosol direct radiative forcing, the Northern Hemisphere loses about 1.6 Wm^{-2} compared with the Sourthern Hemisphere, and the ocean surface in the Northern Hemisphere loses about 4 Wm^{-2} (Table 5.1).

Because they have short atmospheric residence times, aerosols have concentrations which vary in accordance with their long-term average concentration. Large monthly mean optical depths arise because of the proximity of sources. Large optical depths lead to, on average, large day-to-day variability in the optical depths. Likewise, regions with large seasonal mean optical depths exhibit, on average, correspondingly large year-to-year fluctuations in the seasonal means. The variability in optical depths was well represented by a gamma distribution function. For $1° \times 1°$ latitude-longitude regions the monthly mean aerosol optical depths exhibited year-to-year variability that was comparable to their day-to-day variability. Such large variability in monthly mean optical depths suggests that many years of *in situ* observations would be needed in order to determine trends in aerosol concentrations suitable for assessing the performance of models that calculate climatological concentrations.

6.2 Future Work

While the optical depths derived using the 2-channel, 2-aerosol model retrieval scheme were well correlated with measured optical depth from a variety of surface-based instruments, they were biased toward higher values (Fig. 4.3a). One possible explanation for the overestimation is that the average continental model leads to particles that are too small. An alternative approach to using the maritime tropical and average continental models from Hess et al. (1998) would be to construct a model that represents conditions observed during the IFP. Size distribution and aerosol composition measurements made from aircraft and at the surface during the IFP could be used to design an aerosol model and aerosol size distribution for the INDOEX region. Optical depths derived using the new aerosol model would be evaluated against measured values to determine if the statistics have improved.

The radiative transfer calculations were made using an isotropically reflecting bottom boundary (the ocean) with a constant surface albedo of 0.005. An alternative

approach is to include a bidirectional reflectivity function for the bottom boundary. This adds a degree of complexity to the radiative transfer calculations made using DISORT, but may lead to better agreement with observed.

As described in Section 4.3, optical depths and mixing fractions derived using the 2-channel, 2-model scheme were then used to calculate diurnally averaged broadband radiative fluxes. Top of the atmosphere and surface radiative flux is then used to calculate cloud-free aerosol direct radiative forcing. Consequently, errors in the radiative flux calculation will likely show up in the forcing estimates. Derived radiative fluxes were somewhat higher than satellite-observed fluxes (Fig. 4.7) for a limited sample. Reasons for the differences need to be explored.

Three different estimates for aerosol direct radiative forcing for 'average' cloud conditions were presented in Section 4.5. The range in values of the forcings calculated using the three methods is an indication of the degree of uncertainty in characterizing the effects of clouds on aerosol direct radiative forcing. The treatment of clouds needs to be explored. Satellite observations from CERES may be used to better characterize forcing, though the fact that most clouds in the INDOEX region during the winter monsoon were sub-pixel scale complicates the problem.

Bibliography

Adams, J.P., J.H. Seinfeld, and D.M. Koch, 1999: Global concentrations of tropospheric sulfate, nitrate, and ammonium aerosol simulated in a general circulation model. *J. Geophys. Res.*, **104**, 13,791-13,823.

Albrecht, B. A., 1989: Aerosols, cloud microphysics, and fractional cloudiness. *Science*, **245**, 1227-1230.

Andreae, M. O., 1995: Climatic effects of changing atmospheric aerosol levels Ch 10, in World *Survey of Climatology*, vol. 16, Future Climates of the World, edited by A. Henderson-Sellers, Elsevier, New York.

Brest, C. L., and Rossow, W. B., 1992: Radiometric calibration and monitoring of NOAA AVHRR data for ISCCP. *Int. J. Remote Sens,* **13,** 235-273.

Charlson, R. J., 1988: Have the concentrations of tropospheric aerosol particles changed? In *Physical, Chemical, and Earth Sciences Research Reports.* F. S. Rowland and I. S. A. Isaksen, eds., Wiley-Interscience, Chichester, UK, 79-90.

Charlson, R. J., and J. Heintzenberg (Eds.), 1995: *Dahlem Workshop Report on Aerosol Forcing of Climate*, 416 pp., John Wiley, New York.

Charlson, R. J., S. E. Schwartz, J. M. Hales, R. D. Cess, J. A. Coakley, Jr., J. E. Hansen, and D. J. Hoffman, 1992: Climate forcing by anthropogenic aerosol. *Science,* **255**, 423-430.

Chin, M.D., J. Jacobs, G.M. Gardner, M.S. Foreman-Fowler, and P.A. Spiro,1996: A global three-dimensional model of tropospheric sulfate. *J. Geophys. Res.*, **101**, 18,667-18,690.

Clarke, A., P. K. Quinn, and J. Ogren, 2000: The INDOEX aerosol: Comparison and summary of microphysical, chemical and optical properties observed from land, ship and aircraft. *J. Geophys. Res.* (submitted for publication).

Coakley, J. A., W. R. Tahnk, A. Jayaraman, P. K. Quinn, C. Devaux, and D. Tanré, 2000: Aerosol optical depths and direct radiative forcing for INDOEX derived from AVHRR: Theory. *J. Geophys. Res.* (submitted for publication).

Cox, C., and W. Munk, 1954: Measurements of the roughness of the sea surface from the sun's glitter. *J. Opt. Soc. Am.*, **44**, 838-850.

Davies, C.N., 1974: Size distribution of atmospheric particles, *J Aerosol Sci,* **5**, 293-300.

Deirmendjian, D., 1964: Scattering and polarization properties of water clouds and hazes in the visible and infrared. *Appl. Opt.*, **3**, 187-196.

Deirmendjian, D., 1969: *Electromagnetic Scattering on Spherical Polydispersions,* American Elsevier, New York, 290 pp.

Devaux, C., P. Goloub, D. Tanré, and B. Chatenet, 2000: Aerosol Characterization from Ground-Based measurements in Male during INDOEX. *J. Geophys. Res.* (submitted for publication).

Durkee, P., F. Pfeil, E. Frost, and E. Shima, 1991: Global analysis of aerosol particle characteristics. *Atmos. Environment, Part A*, **25**, 2457-2471.

Epstein, B., 1947: The mathematical description of certain breakage mechanisms leading to the logarithmic-normal distribution. *J Franklin Inst,* **244**, 471-477.

Gutman, G., Tarpley, D., Ignatov, A., and Olson, S., 1995: Global land products from AVHRR: The enhanced NOAA GVI data set. *Bull. Am. Met. Soc.*, **76**, 1141-1156.

Han, Q., Rossow, W. B., and Lacis, A. A., 1994: Near-global survey of effective droplet radii in liquid water clouds using ISCCP data. *J. Climate*, **7**, 465-497.

Han, Q., Rossow, W. B., Chou, J., and Welch, R.M., 1998: Global survey of the relationships of cloud albedo and liquid water path with droplet size using ISCCP. *J. Climate*, **11**, 1516-1528.

Hansen, J. E., 1971: Multiple scattering of polarized light in planetary atmospheres. Part II. Sunlight reflected by terrestrial water clouds. *J. Atmos. Sci.*, **28**, 1400-1426.

Hansen, J. E., and Travis, L. D., 1974: Light scattering in planetary atmospheres. *Space Science Reviews,* **16**, 527-610.

Harris, F. S., Jr. and McCormick, M. P., 1972: Mie scattering by three polydispersions. *J. Colloid Sci.*, **39**, 536-545.

Haywood, J.M., D.L. Roberts, A. Slingo, J.M. Edwards, and K.P. Shine, 1997: General circulation model calculations of the direct radiative forcing by anthropogenic sulfate and fossil-fuel soot aerosol. *J. Climate*, **10**, 1562-1577.

Hess, M., Koepke, P., and Schult, I., 1998: Optical properties of aerosols and clouds: The software packages OPAC. *Bull. Am. Met. Soc.*, **79**, 831-844.

Higurashi, A. and T. Nakajima, 1999: Development of a two channel aerosol retrieval algorithm on global scale using NOAA/AVHRR. *J. Atmos. Sci.*, **56**, 924-941.

Holben B.N., T. F. Eck, I. Slutsker, D. Tanre, J. P. Buis, A. Setzer, E. Vermote, J. A. Reagan, Y. Kaufman, T. Nakajima, F. Lavenu, I. Jankowiak, and A. Smirnov, 1998: AERONET--A federated instrument network and data archive for aerosol characterization. *Remote Sens. Environ.*, **66**, 1-16.

Houghton, J. T., 1989: *The Physics of Atmospheres*, Cambridge University Press, Cambridge, 271 pp.

Husar, R.B., Prospero, J. M., and Stowe, L. L., 1997: Characterization of tropospheric aerosols over the oceans with the NOAA Advanced Very High Resolution Radiometer optical thickness operational product. *J. Geophys. Res.*, **102**, 16 889-16 910.

Intergovernmental Panel on Climate Control, Radiative forcing of climate change, *Clim. Change*, 339 pp., 1994.

Intergovernmental Panel on Climate Control, The Science of climate change, *Clim. Change 1995*, 572 pp., 1996.

Jayaraman, A., S.K. Satheesh, and V. Ramanathan, 2000: Regional scale differences in aerosol radiative forcing observed over the Arabian Sea and the tropical Indian Ocean from the 1996 to 1999 INDOEX cruises. *J. Geophys. Res.* (submitted for publication).

Junge, C. E., 1963: *Air Chemistry and Radioactivity,* Academic Press, New York, 382 pp.

Kahn, R, P. Banerjee, and D. McDonald, 2000: The sensitivity of multi-angle imaging to natural mixtures of aerosols over ocean. *J. Geophys. Res.* (submitted for publication).

Kaufman, Y. J., and B. N. Holben, 1993: Calibration of the AVHRR visible and near-IR bands by atmospheric scattering, ocean glint, and desert reflection. *Int. J. Remote Sens.*, **14,** 21-52.

Kaufman, Y. J., D. Tanre, H. R. Gordon, T. Nakajima, J. Lenoble, R. Frouin, H. Grassl, B. M. Herman, M. D. King, and P. M. Teillet, 1997: Passive remote sensing of tropospheric aerosol and atmospheric correction for the aerosol effect. *J. Geophys. Res.*, **102**, 16 815-16 830.

Khrgian, A. K. A., and Mazin, I. P., 1952: The drop size distribution in clouds. *Trudy Tsent, Aerolog Observ,* 7, 56-61.

Kidwell, K. B., 1994: *NOAA Polar Orbiter Users Guide* (Washington, D.C.: U.S. Department of Commerce, National Oceanic and Atmospheric Administration, National Environmental Satellite, Data, and Information Service, National Climatic Data Center, Satellite Data Services Division).

King, M. D., Harshvardhan, and Arking, A., 1984: A model of the radiative properties of the El Chichon stratospheric aerosol layer. *J. Cli. App. Met.,* **23**, 1121-1137.

Kratz, D. P., 1995: The correlated *k*-distribution technique as applied to the AVHRR channels. *J. Quant. Spectrosc. Radiat. Transfer*, **53**, 501-517.

Kukla, G., and Robinson, P., 1980: Annual cycle of surface albedo. *Mon. Wea. Rev.*, **108**, 56-68.

Lacis A.A., and J.E. Hansen, 1974: A parameterization for the absorption of solar radiation in the Earth's atmosphere. *J. Atmos. Sci.*, **31**, 118-133.

Loeb, N. G., 1997: In-flight calibration of NOAA AVHRR visible and near-IR bands over Greenland and Antarctica. *Int. J. Remote Sens.,* **18,** 477-490.

May, D. A., Parmeter, M. M., Olszewski, D. S., and McKenzie, B. D., 1998: Operational processing of satellite sea surface temperature retrievals at the Naval Oceanographic Office. *Bull. Am. Met. Soc.*, **79**, 397-407.

McClain, E. P., W. G. Pichel, and C. C. Walton, 1985: Comparative performance of AVHRR-based multichannel sea surface temperatures. *J. Geophys. Res.*, **90**, 11 587-11 601.

McClatchey, R. A., Fenn, R. W., Selby, J. E., Volz, F. E., and Garing, J. S., 1972: *Optical Properties of the Atmosphere*, 3rd edn. AFCRL-72-0497, Environmental Research Papers No. 411.

Mischenko, M.I., I.V. Geogdzhayev, B. Cairns, W.B. Rossow, and A.A. Lacis, 1999: Aerosol retrievals over the ocean by use of channels 1 and 2 AVHRR data: sensitivity analysis and preliminary results. *Appl. Opt.*, **38**, 7325-7341.

Nakajima, T. and A. Higurashi, 1997: AVHRR remote sensing of aerosol optical properties in the Persian Gulf region, summer 1991. *J. Geophys. Res.*, **102**, 16,935-16,946.

Nakajima, T. and King, M. D., 1990: Determination of the optical thickness and effective particle radius of clouds from reflected solar radiation measurements. Part I: Theory. *J. Atmos. Sci.*, **47**, 1878-1893.

Patterson, E. M., and Gillette, D. A., 1977: Commonalities in measured size distributions for aerosols having a soil-derived component. *J. Geophys. Res.*, **82**, 2074-2082.

Pendorf, R., 1957: Tables of the refractive index for standard air and the Rayleigh scattering coefficient for the spectral region between 0.2 and 20.0 μm and their application to atmospheric optics. *J. Opt. Soc. Amer.*, **47**, 176-182.

Quinn, P.K., T.S. Bates, D.J. Coffman, T.L. Miller, J.E. Johnson, C. Neususess, E.J. Welton, P. Sheridan, 2000: Variability in Aerosol Optical Properties during INDOEX and Controlling Factors. *J. Geophys. Res.* (submitted for publication).

Rajeev, K., V. Ramanathan, and J. Meywerk, 2000: Regional aerosol distribution and its long-range transport over the Indian Ocean. *J. Geophys. Res.*, **105**, 2029-2043.

Ramanathan, V., P. J. Crutzen, J. A. Coakley, Jr., A. Clarke, W. D. Collins, R. Dickerson, D. Fahey, B. Gandrud, A. Heymsfield, J. T .Keihl, J. Kuettner, T. Krishnamurti, D. Lubin, H. Maring, J. Ogren, J. Prospero, P. J. Rasch, D. Savoie, G. Shaw, A. Tuck, F. P .J. Valero, E. L. Woodbridge, and G. Zhang, Indian Ocean Experiment (INDOEX): A multi-agency proposal for a field experiment in the Indian Ocean, *C4 Publ. 143*, Scripps Inst. Of Oceanogr., Univ. of Calif. San Diego, La Jolla, June 1996.

Ramanathan, V., I. Podgorny, S. Satheesh, J. Anderson, G. Cass, T. Clarke, P. J. Crutzen, W. D. Collins, J. Coakley, B. Gandrud, A. Heymsfield, J. Heintzenberg, A. Jayaraman, J. Kiehl, A. P. Mitra, J. Ogren, T. Novakov, K. Prather, G. Shaw, 2000: An Integrated assessment of the INDOEX AEROSOL Climate Forcing and Response. *J. Geophys. Res.* (submitted for publication).

Rao, C. R. N., and Chen, J., 1995: Inter-satellite calibration linkages for the visible and near-infrared channels of the Advanced Very High Resolution Radiometer on the NOAA-7, -9, and –11 spacecraft. *Int. J. Remote Sens.,* **16,** 1931-1942.

Rao, C. R. N., and Chen, J., 1996: Post-launch calibration of the visible and near-infrared channels of the Advanced Very High Resolution Radiometer on NOAA-14 spacecraft. *Int. J. of Remote Sens.,* **17,** 2743-2747.

Roelofs, G.-J., J. Lelieveld, and L. Ganzeveld, 1998: Simulation of global sulfate distribution and the influence on effective cloud drop radii with a coupled photochemistry-sulfur cycle model. *Tellus*, **50B**, 224-242.

Satheesh, S. K., Ramanathan, V., Li-Jones, X., Lobert, J. M., Podgorny, I. A., Prospero, J. M., Holben, B. N., and Loeb, N. G., 1999: A model for the natural and anthropogenic aerosols over the tropical Indian Ocean derived from INDOEX data. *J. Geophys. Res.*, **104**, 27,421-27,440.

Satheesh, S.K. and V. Ramanathan, 2000: Large differences in tropical aerosol forcing at the top of the atmosphere and Earth's surface. *Nature*, **405**, 60-63.

Sato, M., J. E. Hansen, M. P. McCormick, and J. B. Pollack, 1993: Stratospheric aerosol optical depths, 1850-1990. *J. Geophys. Res.*, **98**, 22 987-22 994.

Spiro, P. A., D. J. Jacob, and J. A. Logan, 1992: Global inventory of sulfur emissions with 1 degrees * 1 degrees resolution. *J. Geophys. Res.*, **97**, 6023-6036.

Stamnes, K., Tsay, S-C., Wiscombe, W., and Jayaweera, K., 1988: Numerically stable algorithm for discrete-ordinate-method radiative transfer in multiple scattering and emitting layered media. *Appl. Opt.*, **27**, 2502-2509.

Stone, R. S., Key, J. R., and Dutton, E. G., 1993: Properties and decay of stratospheric aerosols in the arctic following the 1991 eruptions of Mount Pinatubo. *Geo Res Lett,* **20**, 2359-2362.

Stowe, L.L., A.M. Ignatov, and R.R. Singh,. 1997: Development, validation, and potential enhancements to the second-generation operational aerosol product at the National Environmental Satellite, Data, and Information Service of the National Oceanic and Atmospheric Administration. *J. Geophys. Res.*, **102**, 16,923-16,934.

Stratton, J. A., 1941: *Electromagnetic Theory,* McGraw-Hill Book Co., New York, 615 pp.

Sverdrup, G. M., Whitby, K. T., and Clark, W. E., 1975: Characterization of California aerosols, 2, Aerosol size distribution in the Mojave Desert. *Atmos. Environ.*, **9**, 483-494.

Tahnk, W.R. and J.A. Coakley, Jr., 2000: Aerosol Optical Depths and Direct Radiative Forcing for INDOEX Derived from AVHRR: Observations, January - March, 1996 – 2000. *J. Geophys. Res.* (submitted for publication).

Tahnk, W.R. and J.A. Coakley, Jr., 2000a: Improved calibration coefficients for NOAA-14 AVHRR visible and near-IR channels. *Int. J. Remote Sens.* (in press).

Tahnk, W.R., and J.A. Coakley, Jr., 2000b: Further improvements to calibration coefficients for NOAA-14 AVHRR channels 1 and 2. *Int. J. Remote Sens.* (submitted for publication).

Twomey, S. A., 1977: The influence of pollution on the shortwave albedo of clouds. *J. Atmos. Sci.*, **34**, 1149-1152.

Twomey, S. A., M. Piepgrass, and T. L. Wolfe, 1984: An assessment of the impact of pollution on global cloud albedo. *Tellus,* **36B**, 356-366.

van de Hulst, H. C., 1957: *Light Scattering by Small Particles,* John Wiley and Sons, Inc., New York, 470 pp.

Wang, M. and H.R. Gordon, 1994: Estimating aerosol optical properties over the oceans with the multiangle imaging spectroradiometer: Some preliminary results. *Appl. Opt.*, **33**, 4042-4057.

Weller, G., 1980: Spatial and temporal variations in the South Polar surface energy balance. *Mon. Wea. Rev.*, **108**, 2006-2014.

Whitby, K. T., R. B. Husar, and B. Y. H. Liu, 1972: The aerosol size distribution of Los Angeles smog, in *Aerosols and Atmospheric Chemistry*, edited by G. M. Hidy, pp. 237-264, Academic, New York.

Whitby, K. T. and Cantrell, B., 1975: Atmospheric aerosols – Characteristics and measurements. *Int Conf. on Env. Sensing and Assessment*, **2**, Las Vegas, Nev., 14-19 September 1075.

Wielicki, B.A., and L. Parker, 1992: On the determination of cloud cover from satellite sensors: The effect of sensor spatial resolution. *J. Geophys. Res.*, **97**, 12,799-12,823.